Single GaAs nanowire spectroscopy: From 1D quantum confinement to optical waveguiding and lasing

DISSERTATION

zur Erlangung des
Doktorgrades der Naturwissenschaften (Dr. rer. nat.)
der Fakultät für Physik der Universität Regensburg

vorgelegt von

Viola Zeller

aus Saal a. d. Donau

2023

Das Promotionsgesuch wurde eingereicht am 23. November 2022

Die Arbeit wurde angeleitet von Prof. Dr. Dominique Bougeard.

Prüfungsausschuss:

Vorsitzender:	Prof. Dr. John Schliemann
Erstgutachter:	Prof. Dr. Dominique Bougeard
Zweitgutachter:	Prof. Dr. Christian Schüller
Weiterer Prüfer:	Prof. Dr. Sergey Ganichev

Contents

1 Introduction

Semiconductor nanowires, with their lateral dimensions in the range of a few hundreds of nanometers and lengths in the micrometer scale, have attracted significant attention in recent decades due to their unique electrical and optical properties. The term "wire" already implies the one-dimensional character of the object, representing a natural medium for directional transport in one dimension. However, when speaking of one-dimensionality in this regard, one should distinguish two different kinds of this directional motion - for electric charges on the one hand, and for light guided along the wire axis on the other hand.

The spatial confinement of charged particles into one dimension of free motion requires to reduce the semiconductor material along the other two directions down to the scale of the electron wavelength. In this type of confinement, the particle's wavefunction becomes localized in the confined dimension, and its behavior is governed by the principles of quantum mechanics - a *quantum wire* is then formed. They represent a subclass of semiconductor nanowires, reached for sufficiently small diameters. Quantum wires stand out among spatially confined solid-state systems. Their unique quantized properties build the basis of rich physics [1], leading to intriguing phenomena, such as fully ballistic transport [2], manifestation of strong correlation [3, 4] and the formation of new quasi-particle states [5, 6], for example.

The second manifestation of one-dimensionality we will address in the present thesis concerns electromagnetic waves, described in the framework of classical electromagnetism. The high refractive index contrast of a dielectric wire to its environment will guide light along the one-dimensional channel and thus supports *optical waveguiding*. Nowadays, optical waveguiding is indispensable in applied technologies, including fiber-optic communication, laser technology, and sensing.

Given their wire-like shape and dielectric nature, semiconductor nanowires with diameters of a few hundreds of nanometers, are able to guide visible and infrared light along their longitudinal axis, acting as optical waveguides on smallest spatial dimensions,

approaching the diffraction limit. Due to their unique photonic properties, semiconductor nanowires have established as fundamental building block in the realm of nanophotonics, including their implementation in light-emitting diodes or solar cells [7, 8]. Optical waveguiding in nanowires is furthermore of particular relevance in the research field of nanolasers and on-chip coherent light sources [9].

When investigating the optical characteristics of nanophotonic devices, the electronic and photonic properties can never be considered in isolation. Proved for the first time by E. M. Purcell [10], it is known, that the emission and absorption ability of an emitter is highly affected by it's electromagnetic environment. Be it the vacuum field or the altered field inside an optical cavity, the excited particle can only emit its energy into available electromagnetic, or photonic modes. That is, emission/absorption is inhibited when there are no photonic modes around the particle, and vice versa, the probability of photon emission/absorption increases the more photon states exist.

Due to their strong waveguiding nature, light-matter interaction is always inherently present in semiconductor nanowires. Mainly determined by the wire diameter, the emission probability can be increased, or reduced, dependent on whether optical waveguide modes exist inside the nanowire [11, 12]. Optical waveguiding in dielectric media, however, is governed by the diffraction limit of light. In GaAs nanowires, the ability to confine the emitted light therefore demands cross-sectional dimensions of above 200 nm.
By contrast, referring back to the electronic, one-dimensional quantum confinement requires thin diameters of only a few tens of nanometers, a range, in which no photonic waveguide modes exist. Consequently, the length scales between the one-dimensional confinement of light and the one for electrons, do not coincide. Building a bridge between these two length scales, however, could result in widespread technological advances, e.g., in the realization of single-mode quantum wire lasers, which are based on the confinement of both, charge carriers and light, into one-dimension.
GaAs/AlGaAs core/shell nanowires are highly attractive in that respect. The coinciding lattice constants, but still large difference in energy bandgap, make planar heterostructures of this material system already broadly used in technological applications. Concerning nanowires, another key feature of this material system is the low refractive index contrast between the GaAs core and the AlGaAs shell. Building a potential wall for electrons, the interface between core and shell does barely affect the characteristics of propagating light. By having control over the GaAs core diameter, as well as the AlGaAs shell thickness, one-dimensional confinement can thus simultaneously be reached for both, electrons and electromagnetic waves: in the GaAs core for electrons and holes, in the waveguiding GaAs/AlGaAs entity for light.

Only recently, the implementation of ultrathin GaAs-based nanowires has made strong one-dimensional quantum confinement accessible in optical experiments [13–17]. At the time of this thesis, studies of such one-dimensional quantum confinement in combination with optical waveguiding, however, has still been absent, such that the potential of self-assembled nanowires has not yet been evaluated to realize quantum wire lasers.

On the other hand, first pioneering works on lasing in single GaAs/AlGaAs core/shell nanowires, operating up to room-temperature, were published in 2013 [18, 19]. Until today, detailed studies on the lasing threshold, however, has been scarce. Especially in the realm of plasmonic and hybrid-plasmonic nanolasers, GaAs-based nanowires have hardly been investigated [20, 21].

This thesis is structured into two main objectives:
The first one seizes the topic of one-dimensional quantum confinement with a special focus on the electronic dispersion in wurtzite quantum wires. We also address and systematically investigate the role of the AlGaAs shell in connection with the photonic properties of the quantum wires.
The second purpose is to explicitly study the aforementioned waveguide nature in connection with the lasing behavior of single GaAs nanowires. Our analysis includes an exploratory study on the coupling between photonic modes and surface plasmons in the vicinity of a metal surface. A systematic evaluation of the lasing efficiency additionally provides the basis for future choices in GaAs-based nanolaser design.

All of our experiments are performed using single-wire micro-photoluminescence spectroscopy. For the optical excitation of single wires, we use laser sources with different energies operating under cw or pulsed mode. Spectral-, time- and polarization-resolved photoluminescence spectroscopy thereby provides an excellent tool to probe internal electronic properties as well as photonic effects. Moreover, by supplementing our experimental results with numerical electromagnetic simulations and $\mathbf{k}\cdot\mathbf{p}$ calculations, this work provides a comprehensive analysis of the studied effects.

Subsequent to this introduction, the present thesis is structured as follows:

Part I The first part introduces fundamental notions, relevant for the experiments and analyses reported in this thesis. We start with explaining the structural differences between the well-known zinc-blende crystal phase and the unusual wurtzite phase in GaAs, the formation of which is observed solely in nanowires. The subsequent chapter addresses the fabrication of wurtzite GaAs nanowires via catalyzed epitaxy, both in terms of principles and technical implementation. The first experimental study of this thesis is presented and concerns the development of an epitaxy recipe for the growth of ultrathin wurtzite GaAs nanowires for single wire optical experiments. The last chapter of part I is then concerned with the fundamentals of the optical processes involved in our experiments, focusing on spontaneous emission and photoluminescence in semiconductors, and finally introduces the technical aspects of our experimental photoluminescence setup.

Part II Having established the characteristics of the wurtzite phase and fabrication of ultrathin nanowires, the second part is dedicated to the optical spectroscopy

of wurtzite quantum wires. To begin with, the theoretical basics of one-dimensional spatial quantum confinement are introduced, followed by an experimental proof of strong size-quantization effects in our GaAs nanowires. By a thorough combined experimental and theoretical analysis, supported by numerical simulations, we disentangle the polarization anisotropies of wurtzite GaAs in the quantum regime from those of photonic effects. We carefully analyze the overlap between electronic and photonic polarization selection rules in the emitted light as a function of the AlGaAs shell thickness, which was found to be the major tuning parameter.

Part III In the last part of the thesis, we investigate the functionality of GaAs nanowires operating as nanolasers. At first, we introduce the fundamental concepts of semiconductor nanowire lasers, including the details of photoluminescence waveguiding, which were specifically developed for our GaAs wires using numerical simulations. Afterwards, the main objective of this part is to study the influences of different dielectric, metallic or hybrid substrates on the lasing behavior of our GaAs nanowires. For each structure, we elucidate the change in waveguiding nature resulting from plasmonic coupling and provide a detailed analysis on the lasing performance. We furthermore carve out their respective main advantages as well as the major challenges that come along. In Ch. 14, the essential findings and main statements of this part are summarized and conclusively analyzed.

To finalize this work, a last chapter is appended to summarize our experimental results and to conclude the reached objectives. It also includes an outlook on a possible direction of future studies related to the presented research area.

GaAs nanowire epitaxy and spectroscopy

2

Structural properties of GaAs nanowires

Along with silicon, gallium arsenide (GaAs) is one of the most frequently investigated semiconductors. The direct bandgap, with its energy in the the near-infrared part of the electromagnetic spectrum, makes this material particularly advantageous for optical and opto-electronic applications. Together with aluminum gallium arsenide (AlGaAs), GaAs-based heterostructures are very important in fundamental research and have already found numerous applications in the semiconductor industry. The electronic properties of GaAs in the zinc-blende (ZB) phase has therefore been well-documented over the last decades.
In nanowires, the reduction in dimensions induces a new degree of freedom in the control of the band structure. The precise epitaxial control of morphology and crystal structure have made it possible to synthesize GaAs, and other non-nitride semiconductor compounds (e.g. indium arsenide or indium phosphide) in the wurtzite (WZ) crystal phase, which is not stable in the bulk form of the respective materials. The electronic band structure of WZ GaAs has thus only recently gotten into the focus of research. Despite of considerable efforts, fundamental properties of the WZ phase are still under debate. In experimental studies, for instance, the reported values of the fundamental bandgap of WZ GaAs range from 1.50 eV [22, 23] to 1.54 eV [24].
Most important in this thesis are the altered optical selection rules that result from the WZ crystal phase as compared to the ZB counterpart. In this chapter, we present the main differences between the ZB and the WZ crystal structures and outline the peculiarities of the resulting WZ band structure.

2.1 The zinc-blende and wurtzite crystal phase

The zinc-blende structure is a face-centered cubic (fcc) lattice, containing two sublattices at the basis $(0,0,0)$ and $(\frac{1}{4},\frac{1}{4},\frac{1}{4})\,a_{\mathrm{ZB}}$, where $a_{\mathrm{ZB}} = 5.65\,\text{Å}$ is the lattice constant of zinc-blende GaAs. In GaAs, the two different lattice sites are occupied by gallium or

arsenic atoms, respectively.
The ball-and-stick model in Fig. 2.1 (a) shows the atom stacking along the [111]-direction, which is the preferential growth direction of NWs in the ZB crystal phase [25]. WZ, on the other hand, belongs to the hexagonal crystal family. Its corresponding stacking order with a bi-atomic basis is shown in Fig. 2.1 (b), along the hexagonal [0001]-direction. For hexagonal-closest packing, the ZB and the WZ phase differ only in their stacking sequence: In ZB, the stacking-sequence can be denoted as ABCABC..., where each letter represents one of the three possible positions of the group III or group V atom in the respective layer. In WZ, only two positions are possible, resulting in the stacking sequence notation ABABAB... [26, 27]. The altered stacking order in the WZ crystal compared to the ZB crystal comes along with a different lattice parameter nomenclature: The lattice constant c is along the [0001]-direction, which is the growth direction of wurtzite nanowires that corresponds to the [111] ZB crystal direction, also referred to c-axis in NWs. The second lattice constant is a_{WZ}, which parameterizes the dimension perpendicular to the c-axis. For an ideal WZ crystal, the lattice constants are linked and given by $a_{\mathrm{WZ}} = a_{\mathrm{ZB}}/\sqrt{2}$ and $c = \sqrt{8/3}\, a_{\mathrm{WZ}}$ [28].
The tetrahedral bonding of one atom with its four direct neighbors is identical in both cases, but the different stacking order results in a different distance of the atom with its third nearest neighbor. This is illustrated by the two neighboring bonding tetrahedra for the cubic case in Fig. 2.1 (a), and the hexagonal case in Fig. 2.1 (b). While in the cubic ZB lattice the ions of two different charges (here depicted in two separate colors) exhibit the largest possible distance to each other, the upper bilayer in the hexagonal WZ lattice is twisted by 60°. As a result, the two differently charged ions and their covalent bonds are directly stacked on top of each other. This significantly changes their balance and yields a net third-nearest-neighbor repulsive force [29]. With this picture, it becomes more clear, that the structural differences between the ZB and the WZ GaAs crystal phases also come along with a significant change in electronic energy dispersion. These differences will be discussed in the next section.

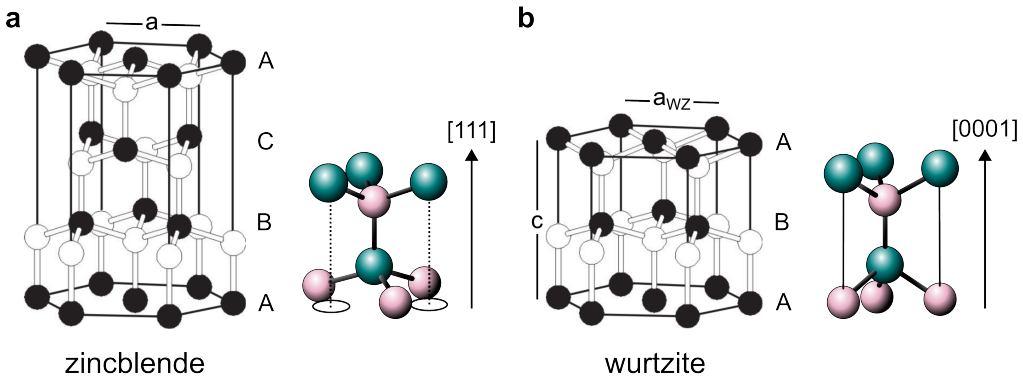

Figure 2.1: Crystal structure differences between the zinc-blende and the wurtzite phase. (a) Stacking order of a ZB crystal along the cubic [111] direction. The stacking sequence of the plane of III-V pairs can be assigned to ABCABC... Right-hand side: Two neighboring bonding tetrahedra of the ZB structure. Two ions with opposite signs (depicted in different colors) have the largest possible distance. (b) Same as in (a) for the hexagonal WZ crystal structure. The stacking sequence is changed to ABABAB... As a result, two oppositely charged ions of two neighboring tetrahedra are placed on top of each other, which results in a net repulsive force. Adapted from Refs. [26] and [27].

2.2 Band structure and optical selection rules in bulk wurtzite GaAs

As wurtzite GaAs appears exclusively in nanowires, the fundamental electronic properties of this crystal phase are much less well explored and understood as in its ZB counterpart. The symmetry of the wurtzite structure has a substantial impact on the resulting band structure. In general, the literature is consistent with the form of the splitting of the individual bands in WZ GaAs, although the exact energy values still differ from study to study. In the present section, we follow Refs. [28, 30–33] in terms of band symmetry notation and selection rules.

For a direct comparison between the ZB and the WZ band structure, Fig. 2.2 (a) schematically depicts the energy levels involved in the lowest energy optical transitions at the Γ-point of the Brillouin zone. The energy levels are designated according to the "BSW" (Bouckaert, Smoluchowski and Wigner)-notation [34], which labels the symmetry of the wavefunction in the given band. The indices "c" and "v" thereby stand for the conduction and the valence band, respectively. In the absence of spin-orbit coupling, the transition from ZB to WZ causes the p-like Γ_{15v} valence band to split into two bands with Γ_{6v} and Γ_{1v} symmetry. The energy difference of this crystal field splitting is denoted as Δ_{crystal}. In terms of p-orbitals, the Γ_{1v} band comprise p_z orbitals, and the Γ_{6v} band p_x and p_y orbitals [28]. Furthermore, the energetic alignment between the lowest conduction band and the highest valence band changes by $\Delta\Gamma_c^{WZ-ZB}$ and $\Delta\Gamma_v^{WZ-ZB}$, respectively.

Under the effect of spin-orbit coupling, the Γ_{6v} valence band in WZ further splits into a higher Γ_{9v} and a lower Γ_{7v} energy band. The symmetry of the conduction band, as well as of the third-highest valence band, transforms from Γ_1 to Γ_7. Note, that theoretical works have predicted both Γ_7 and Γ_8 symmetry to exist for the lowest conduction band [28, 29, 35]. Experimental works, however, have attributed the Γ_{7c} band to be the energetically more favorable state [36, 37]. In ZB on the other hand, spin-orbit coupling leads to a splitting of the Γ_{15v} valence band to an upper Γ_{8v} and a lower Γ_{7v} band, as well as in a change in lowest conduction band symmetry from Γ_{1c} to Γ_{6c}.
Another important difference of the WZ phase involves the optical selection rules between the different energy states. The symmetry of the crystalline structure manifests in a preferred polarization of the dipole transitions with respect to the c-axis. For the WZ band structure Taking the WZ band with spin-orbit interaction, the resulting preferred orientations are [33]:

$$\begin{aligned} E \perp c: &\quad \begin{cases} \Gamma_7 \leftrightarrow \Gamma_9 \\ \Gamma_7 \leftrightarrow \Gamma_7 \end{cases} \\ E \parallel c: &\quad \Gamma_7 \leftrightarrow \Gamma_7. \end{aligned} \tag{2.1}$$

Hence, an optical transition between the conduction band, Γ_{7c}, and the highest valence band, Γ_{9v}, is only allowed for perpendicular polarizations, while the transition $\Gamma_{7c} \leftrightarrow \Gamma_{7v}$ is allowed for perpendicular *and* parallel dipoles.
The energy dispersion $E(\mathbf{k})$, in the vicinity of the Γ-point, is illustrated in Fig. 2.2 (b). The three upper valence bands are denoted as heavy-hole (hh), light-hole (lh) and split-off (so) band. The most significant difference to the ZB structure is the energy splitting between the hh and the lh valence bands at $\mathbf{k} = 0$, which are degenerate in the ZB phase. The energetic distance between the Γ_{9v} and the Γ_{7v} is commonly found to be about 100 meV [30, 37, 38]. The optical transitions and selection rules, which are most relevant for this thesis, are annotated by the dashed arrows. According to Eq. 2.1, transitions between the conduction band (cb) and the hh band are only allowed for polarizations perpendicular to the c-axis, while cb $\leftrightarrow$ lh transition occur for any polarization. Hence, it is possible to distinguish interband transitions involving the hh band from those involving the lh band by analyzing the respective polarization.
Most studies investigating the WZ band structure of GaAs do not address quantum confinement effects, and consider NWs as small, cylindrical pieces of bulk material. It was not until 2016, that Vainorius *et al.* first reported optical access to one-dimensional subbands in self-assembled GaAs *quantum* wires. One-dimensional quantum confinement effects will become relevant in part II of this thesis, with a particular focus on the optical selection rules. At first, we show in the following chapter, how our nanowires are synthesized via molecular-beam epitaxy.

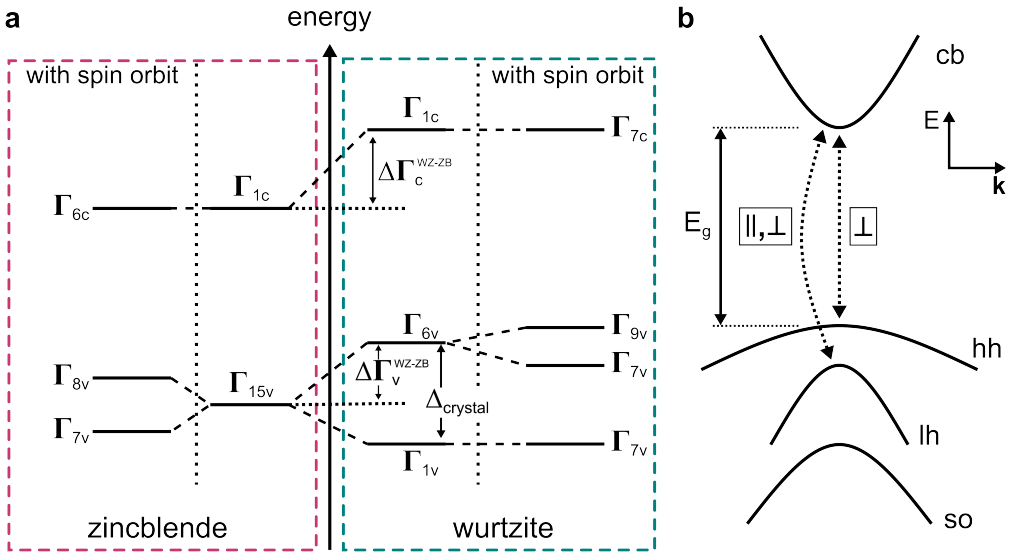

Figure 2.2: (a) Schematic of the band energies and wavefunction symmetries in ZB and WZ structures at the Γ-point, with and without spin-orbit interaction. (b) Simplified electronic energy dispersion of WZ GaAs around $\mathbf{k} = 0$. The most significant difference to the ZB dispersion is the energy splitting of the hh and the lh band at $\mathbf{k} = 0$. The symmetry of the bands, depicted in (a), results in different optical selection rules for the hh and the lh band. Subfigure (a) is adapted from Ref. [31]

3

Synthesis of GaAs nanowires

All NWs presented in this thesis are grown by molecular-beam epitaxy (MBE) in the in-house MBE system. In this chapter, we first give an overview over the general concept of MBE. Afterwards we concentrate on the principle of non-planar, vertical growth of nanowires, with a special focus on the selection rules established for growing the WZ or ZB structure. The third part then finally presents the experimental implementation of phase pure and ultrathin WZ nanowires, which allow us to realize the 1D quantum confinement discussed in part II of this work.

3.1 Molecular-beam epitaxy

In general, epitaxial growth is based on preserving the crystalline structure of a material when new layers are deposited onto the surface. MBE is a modern growth technique, dedicated to the growth of semiconductors with the highest achievable purity. A sketch of a MBE chamber is shown in Fig. 3.1. The growth chamber comprises various, shutter-controlled effusion cells containing the individual, high-purity materials. Under

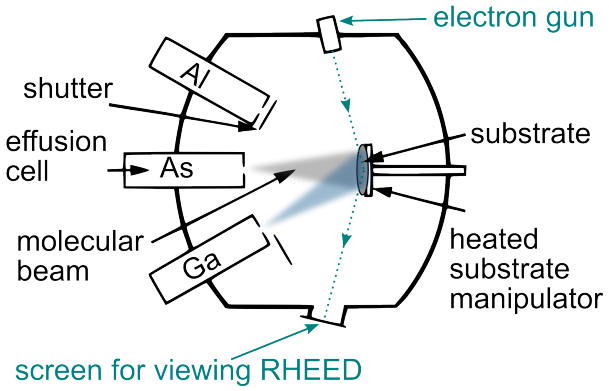

Figure 3.1: Schematic of a molecular-beam epitaxy system. The shutter-controlled effusion cells are directed towards the growth substrate, which is mounted onto a heated, rotatable substrate manipulator. The growth can be *in situ* monitored via RHEED. Adapted from Ref. [39].

heating, the source elements are sublimated from the effusion cells and evaporated as a molecular beam onto an appropriate substrate. The latter is mounted onto a heated substrate manipulator that facilitates rotation to ensure an uniform distribution of the atoms on the surface. In the chamber, ultra-high vacuum (UHV) conditions prevail, with a base pressure in the range of 1×10^{-11} mbar that ensures a high mean free path of the evaporated molecules and furthermore minimizes the incorporation of impurities into the growing crystal. The growth procedure can be monitored via a reflection high-energy electron diffraction (RHEED) system. For that purpose, an electron gun directs a beam of electrons onto the substrate, and the diffracted or reflected electrons are visualized on a fluorescent screen on the opposite side of the chamber. The method of monitoring growth via RHEED, in particular with respect to the growth of NWs, is discussed in more detail in Sec. 3.2.3.
The MBE system at the University of Regensburg comprises four different growth chambers, which are interconnected by a vacuum tube. This allows an *in situ* transfer of samples between the chambers, without them being exposed to air. A technical drawing of the entire MBE cluster in top view is shown in Fig. 3.2. The cluster involves a silicon/germanium (Si/Ge), a topological insulator (TI), a metal/oxide (M/O) and a III-V MBE chamber. Especially relevant for this thesis are the III-V and the M/O MBEs. The III-V chamber contains group III and group V elements, such as gallium (Ga), arsenic (As) and aluminum (Al), from which our GaAs/AlGaAs core/shell nanowires are synthesized. The M/O MBE is, on the one hand, relevant to prestructuring the growth substrates with a thin, 0.05 Å gold layer (cf. Sec. 3.2.1), and on the other hand to fabricate atomically flat gold substrates, which become relevant in part III of this thesis. The NW growth, which takes place in the III-V MBE, will be described and explained in more detail in the following sections.

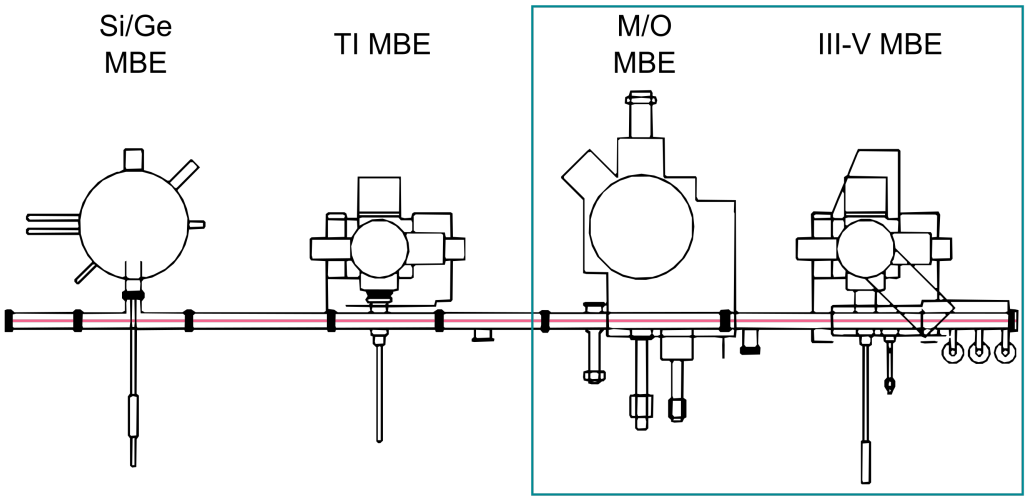

Figure 3.2: Technical drawing of the MBE cluster of the University of Regensburg. The cluster comprises four MBE chambers containing different source materials. A vacuum transfer channel interconnects all chambers and allows an *in situ* transfer between them. The chambers relevant for this thesis are the M/O and the III-V MBE. Adapted from Ref. [40].

3.2 Growth of GaAs nanowires

3.2.1 Principle of the Vapor-Liquid-Solid growth

The most common method of growing free-standing NWs is by the assistance of small seed particles of foreign material, typically a metal. Acting as catalyst, these particles enhance the growth rate in one direction without being incorporated into the crystal itself [41]. The one-dimensional growth of microstructures was observed over 60 years ago [42]. Often, these one-dimensional crystals exhibited a hemispherical metal particle at one end, which led to the idea of the crystal growth being promoted by this particle. The earliest model for this catalytic nanowire growth has been proposed by Wagner and Ellis [43] and was termed *Vapor-Liquid-Solid* (VLS) mechanism. They explained the growth of silicon wires (or "whiskers", as they are called in the original publication) from the gas phase in the presence of a liquid Au/Si alloy droplet. It is named VLS because of the three phases present, and necessary, during the nanowire growth: The vapor phase of the molecular beam or the precursor flux, the liquid alloy of the seed particle droplet and the solid, one-dimensional crystal that is formed.
With the help of Fig. 3.3, we will now qualitatively describe the individual steps involved in the Au-catalyzed VLS growth of our GaAs nanowires. For a detailed theoretical model on the microscopic processes, we recommend the publications from V.G. Dubrovskii and F. Glas (Refs. [44–50]), as well as the PhD theses of Joachim Hubmann [51] and Andreas Rudolph [52] from our group.

To grow vertical, upright-standing GaAs nanowires, we use GaAs$(111)_B$ substrates (the index B denotes that the (111) surface is As terminated), which are covered with a thin Au layer evaporated onto the GaAs substrates in the M/O MBE prior to growth. The term "layer" is here not entirely correct, as the typical deposited gold thickness on our substrates does not exceed 1 Å and is therefore thinner than one monolayer of Au. Instead of full coverage, the deposition produces isolated patches of Au on the substrate, as indicated in step 1 in Fig. 3.3. In step 2, the substrate is heated under constant background pressure of As. During this heating step, Ga atoms from the growth substrate dissolve and develop liquid Au/Ga droplets by forming an eutectic alloy. Afterwards, Ga atoms are evaporated onto the substrate by heating the Ga effusion cell. The liquid droplet acts as the preferred sink for the Ga atoms. They directly impinge, or diffuse towards the droplet and increase the Ga content of the alloy until supersaturation is reached. The nanowire then begins to grow layer by layer on the substrate beneath the droplet, initiating the vertical growth in the [111] crystal direction (step 3). As a result, the minimum NW diameter is limited by the size of the catalyst droplet. The evaporated Ga adatoms continue to diffuse towards the droplet, which promotes a steady vertical growth of the nanowire until the flow of Ga atoms is disrupted. Note, that the pure vertical growth is limited by the diffusion length of the Ga adatoms. Consequently, the NWs exhibit a maximum length above which the atoms start to nucleate on the side facets and increase the diameter. This is exploited during the intentional radial overgrowth of the NWs with a shell in step 5. During this step, the substrate is cooled and the As background pressure is increased, both of which reduce the adatom diffusion. As a result, the radial growth rate is enhanced and the atoms preferable nucleate at the side facets.
We want to emphasize that this last growth step provides the possibility to controllably increase the GaAs core diameter, as well as the thickness of the AlGaAs shell. For optical experiments, the passivation with AlGaAs is required to inhibit non-radiative charge carrier recombination at GaAs surface states. The AlGaAs shell, with its larger bandgap, acts as potential barrier for excited charge carriers, which are captured inside the GaAs core. Typically, the core/shell nanowires are additionally capped with a thin GaAs cap layer to prevent the oxidation of the AlGaAs. In Sec. 3.3, we present the experimental implementation of GaAs nanowire growth with varying AlGaAs shell thicknesses.

3.2.2 Crystal phase formation during growth

The description of the VLS mechanism above does not specify how nanowires can adopt a crystal phase, which is not stable in bulk. The hexagonal WZ phase has been observed for most III-V ZB materials when grown as nanowires [49], but the coexistence of ZB and WZ phases along a single NW often complicates basic studies on the WZ phase. Hence, phase purity control remains one of the major challenges of III-V nanowire fabrication. In our group, a strategy to developed GaAs nanowires with extremely high phase purity was already experimentally implemented by Florian Dirnberger [53] during his PhD thesis, whose results are also reported in Ref. [54]. Given that there are different growth parameter regimes for which either the ZB or the WZ phase formation is preferred, we

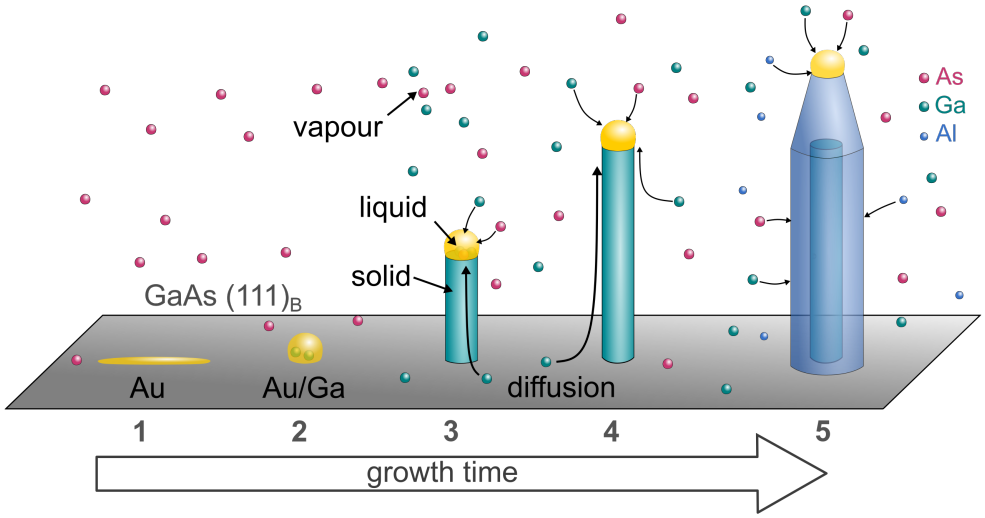

Figure 3.3: Principle of Au-catalyzed VLS growth of our GaAs nanowires. The process involves five steps: Prior to growth, a thin Au layer is deposited onto the GaAs$(111)_B$ substrate (1). During heating under constant As background pressure, liquid Au/Ga alloy droplet are formed (2). The supply with Ga atoms leads to a supersaturation of the droplet followed by nucleation and vertical crystal growth (3). The vertical growth steadily continues through direct impinging or diffusion towards the catalyst droplet, until the flow of Ga atoms is disrupted (4). By reducing the temperature and enhancing the As pressure, diffusion is damped and the wires can be radially overgrown with an (Al)GaAs shell (5).

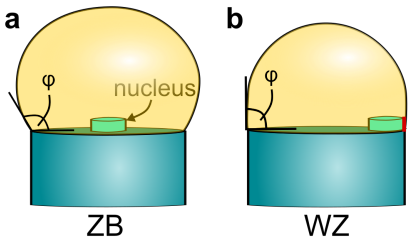

Figure 3.4: Graphical illustration of the two energetically different nucleation sites of a new monolayer. (a) The nucleation can take place at the center of the droplet/NW interface, or (b) at the triple phase line (TPL) (indicated by the red bar). At situation (a), only the ZB structure grows, while in situation (b) the metastable WZ phase is favored. The site of nucleation is furthermore dependent on the droplet size and the contact angle φ.

now elucidate the crystal phase formation during growth based on the model of Glas *et al.* [49].
They identified the nucleus inside the droplet, which initiates the layer growth, to be the key parameter that influences whether the layer is grown in the WZ or the ZB phase. They differentiate between two locations at which a new nucleus can settle: Either at the center of the interface between the droplet and the top facet (cf. Fig. 3.4 (a)), where its lateral surface is entirely surrounded by the liquid, or at the triple phase line (TPL) (marked in red in Fig. 3.4 (b)), where it is partially surrounded by the vapor. A distinct difference to the scenario in (a) is the small part of the liquid (droplet) interface with the vapor that is eliminated and replaced by a nucleus-vapor interface. With the monolayer nucleus having this anchor to the TPL, the total edge energy of a new nucleus can be lower in the WZ position than in the ZB position [55]. The site of nucleation, however, is dependent on various factors and in general more complex as described by Glas *et al.*. This was outlined by Jacobsson *et al.*, who explained the switching between ZB and WZ phase under different growth conditions, using a model that relates the catalyst volume, the contact angle at the trijunction (angle φ in Fig. 3.4) and the nucleation site of a new layer [56]. Growing the nanowires in an ultra-high vacuum chamber inside a transition electron microscope (TEM), they could *in situ* observe and record a variety of different growth modes. Among others, they have demonstrated that the droplet size, and thus the contact angle, play a major role in the phase formation and that the droplet size can be dynamically controlled by the V/III ratio.
Overall, the most relevant aspects for phase selective growth are [57]: The metastable WZ phase only grows when the nucleation of a new bilayer takes place at the TPL. If the nucleation takes place at the TPL, either WZ or ZB structure can be formed, which is dependent on the supersaturation of the catalyst droplet, as well as on the surface energies. As soon as the nucleation takes place away from the TPL, only the ZB structure is formed. The optimal contact angle φ for the WZ phase to occur is close to 90°. For significantly higher and lower contact angles, always the ZB phase was found to grow.

3.2.3 Monitoring the crystal phase via RHEED

Reflection high-energy electron diffraction (RHEED) is a standard tool in MBE to monitor the growth procedure and *in situ* characterize the crystal structure. Usually, the main purpose of RHEED is to gain immediate feedback during thin film growth. It is used to determine the rate of standard planar epitaxial growth, or to make statements about the surface consistency, e.g. occurring surface reconstructions. For non-planar structures, such as nanowires, the geometry changes from reflection to transmission mode, with the electrons being diffracted when they penetrate the nanowires [58, 59].
The principle is illustrated in Fig. 3.5 (a). The RHEED gun, implemented in the III-V chamber of our MBE system, directs a collimated electron beam with an energy of 15 kV onto the growth substrate. The electrons then transmit through the nanowires, which vertically stand on the growth substrate. A fluorescent screen on the opposite side then visualizes the transmitted and diffracted electrons. By fulfilling the Bragg condition, a characteristic diffraction pattern appears on the screen, similar to other diffraction methods such as X-ray diffraction or electron diffraction in TEM.
In our studies, especially in part II of this work, it is essential to have insights about the crystalline quality of our fabricated nanowires. For that purpose, RHEED monitoring can provide very good indication on whether the NW ensemble is primarily grown in the WZ phase. The diffraction pattern of the WZ phase can only be reliably distinguished from the ZB phase along the $[11\bar{2}0]$-direction, which corresponds to the $[1\bar{1}0]$-direction in the cubic ZB crystal. The corresponding direction with respect to the hexagonal NW cross section is sketched in Fig. 3.5. The diffraction pattern of a phase pure WZ structure along this direction, which was recorded during NW growth, is shown in Fig. 3.5 (b). The spots at the WZ positions are very bright and there are no signs of ZB spots. In Fig. 3.5 (c) on the other hand, both WZ and ZB phases are present. In this case, the two diffraction patterns overlap. In order to distinguish them, the spots belonging to the WZ and ZB phase are marked by green and red circles, respectively. Additionally, the pattern in (c) exhibits streaks, which is commonly ascribed to the presence twin defects [59]. Figure 3.5 (d) finally shows the diffraction spots that occur when only the ZB phase is present.
It should be noted, that the crystal purity of single nanowires can only be determined via high-resolution TEM. However, the presented RHEED monitoring during growth indicates the predominant phase of the grown NW ensemble. With an additional optical preselection by photoluminescence analysis, according to Refs. [30, 54], single wires with high WZ phase purity can be reliably identified and investigated.

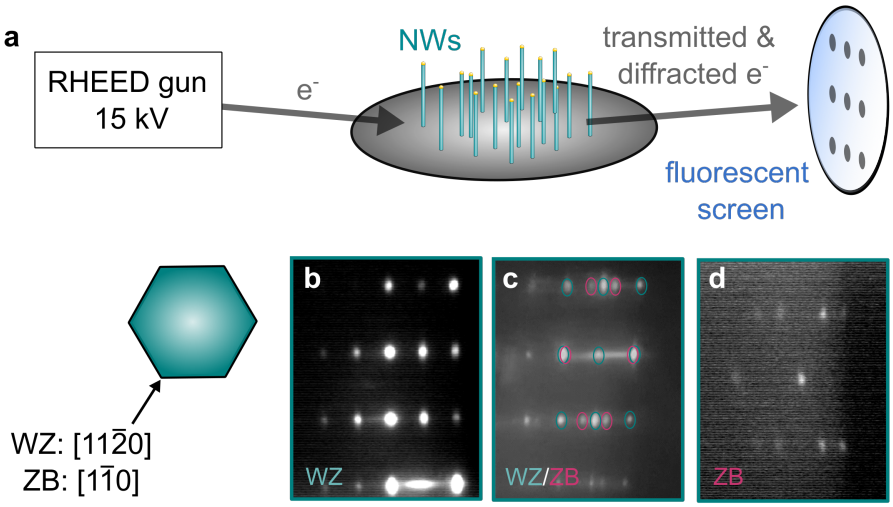

Figure 3.5: Principle of RHEED monitoring during NW growth. (a) A RHEED gun directs a collimated electron beam towards the growth substrate where the NW grow vertically to the substrate surface. The transmitted and diffracted electrons impinge on a fluorescent screen, on which the resulting pattern, according to Bragg's law, provides information about the crystal structure. During NW growth, it is essential to distinguish between the WZ and the ZB phases, which is possible along the $[11\bar{2}0]$-direction (WZ) or the $[1\bar{1}0]$-direction (ZB), respectively. The RHEED pattern in the case of pure WZ, WZ/ZB mix and pure ZB are shown in panels (b)-(d).

3.3 Synthesis of wurtzite wires with strong spatial quantum confinement

3.3.1 Growth of ultrathin GaAs cores

Despite their high-aspect ratio, most NW systems exhibit an electronic structure than is well described in terms of bulk properties. NW-based electronic and nanophotonic devices do not yet exploit the potential of 1D quantum confinement and the concomitant density of states. Although GaAs nanowires have been grown since quite some time, there are only a few reports addressing the 1D quantum confinement in ultrathin GaAs NWs [13, 14, 16, 17]. A major problem is the controlled synthesis of thin wires, since the diameters have to be below 50 nm to observe pronounced quantum confinement effects in GaAs [16, 17]. An unconventional approach to radially shrink GaAs nanowires to diameters of even below 10 nm was proposed by Loitsch *et al.* in 2015 [13]. This approach consists of the growth of regular, Ga-catalyzed nanowires, followed by a subsequent step of high-temperature annealing with absent Ga supply. In their work, this "reverse-reaction growth" step led to a gradual thermal decomposition of the GaAs material from the NW surface, shrinking the core to diameters down to 7 nm.
Concerning the Au-catalyzed nanowires with high WZ phase purity, earlier efforts in our group [53] have demonstrated that this approach is not applicable, as the high-temperature annealing step either destroyed the nanowire morphology or even led to a full sublimation. Instead, it was shown that it is possible to grow ultrathin GaAs nanowires using the regular parameters for the VLS growth of Au-catalyzed NWs. The growth of the ultrathin GaAs wires, which are investigated in this thesis, are based on the attempts in Ref. [53]. The key of growing ultrathin nanowires was found to be in controlling the size of the droplet catalyzer, or furthermore, to achieve the lowest possible average diameter with a narrow size distribution. This requirement is fulfilled when the growth substrate is covered by a thin Au layer of only 0.05 Å. As already outlined in Sec. 3.2.1, such a thin Au layer does not yield a full coverage of the growth substrate, but furthermore patches that are distributed over the surface. Under thermal heating, the large distance between the emerging Au/Ga droplets prevents them from melting with each other and form larger particles.
Hence, all wires presented in part II of this work, are grown on GaAs$(111)_B$-substrates with a Au coverage of 0.05 Å. Stable and reproducible results of ultrathin GaAs wires, featuring high WZ crystal phase purity, are achieved under the following steps: Prior to the NW growth, each substrate is heated to $T = 600\,°C$ for at least 10 min under As background pressure in order to create identical conditions for the nanodroplet formation in all growth runs. Afterwards, the substrate temperature is lowered to $T = 540\,°C$ and the NW growth initiated by opening the Ga effusion cell. In all growth runs, the Ga evaporation rate is kept constant at $R_{Ga} = 0.7$ Å/s. (Note, that this is the 2D equivalent growth rate of GaAs on a GaAs(001) substrate, determined via RHEED). During the core growth, the As beam equivalent pressure is approximately 1.5×10^{-6} Torr, yielding

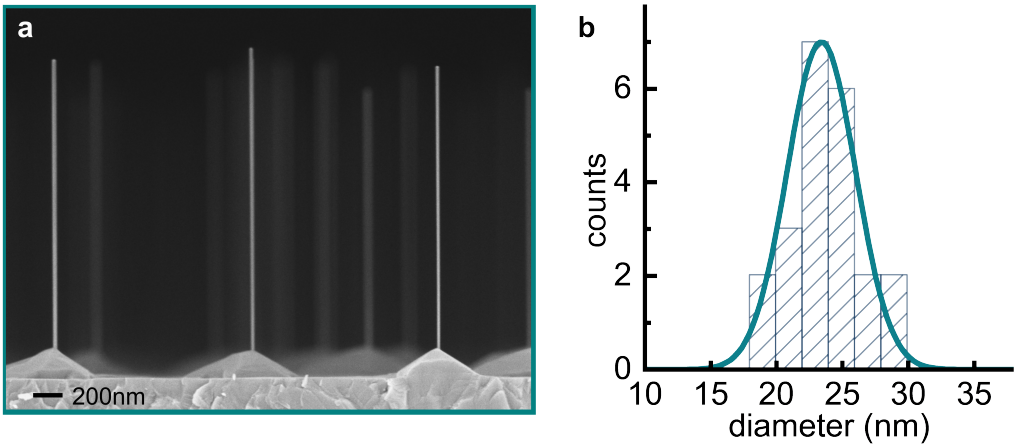

Figure 3.6: Growth of ultrathin GaAs nanowires. (a) SEM image of as-grown GaAs nanowire grown via Au-catalyzed VLS growth on a substrate covered with 0.05 Å Au. All wires have a almost uniform length of 2 µm and ultrathin diameters. (b) The SEM evaluated diameter statistics reveals a mean diameter of 24 nm with a very small standard deviation of only 2.6 nm

a V/III ratio of As/Ga $\approx$ 2. A Ga evaporation time of 95 min reproducibly results in approximately 2 µm long wires with ultrathin core diameters of 20 – 30 nm and a high WZ phase purity. Longer growth periods always result in nanowires with higher diameter and a tapered end facet. We therefore conclude, that 2 µm is the critical nanowire length (at 540 °C), above which the average adatom migration length on the NW side walls is exceeded. The atoms then start to nucleate at the NW side facets and the flow to the droplet is decreased [60, 61]. A SEM image of nanowires, grown under the described conditions, is shown in Fig. 3.6 (a). In all of the wires, we can identify the small Au/Ga droplet on top, which has the same diameter as the grown nanowires. The SEM evaluated diameter statistics in Fig. 3.6 (b) further demonstrates a narrow diameter distribution of only 2.6 nm and a very low mean diameter of 24 nm.

3.3.2 Varying the AlGaAs shell thickness

Due to their high surface-to-volume ratio, semiconductor nanowires are particularly sensitive to surface effects. Surface electronic states can act as surface charged traps or as recombination centers for charge carriers [62, 63]. Both effects significantly impede the optical performance of semiconductor NWs as the majority of charge carriers gets lost non-radiatively. This problem can be overcome by passivating the emitter material with a material of higher bandgap that acts as a potential barrier for charge carriers. GaAs is commonly passivated with AlGaAs, as their almost matching lattice constants allow an epitaxial growth of AlGaAs/GaAs heterostructures.
In order to confine excited charge carriers in the ultrathin GaAs wires, all our optically

investigated nanowires are *in situ* passivated with an $Al_xGa_{1-x}As$ shell. By adjusting the radial overgrowth and the As pressure, the thickness of the shell can be varied while still maintaining the ultrahin GaAs core. For all wires presented in part II, the core is fabricated according to the conditions described in Sec. 3.3.1. After the GaAs core is grown, the the Ga supply is interrupted and the temperature lowered to $T \approx 460\,°C$. Additionally, we enhance the V/III ratio to As/Ga = 4 to further damp the Ga adatom diffusion and thus enhance the radial growth rate [47]. By simultaneously opening the Ga and Al shutter, the ultrathin GaAs cores are then radially overgrown by an $Al_xGa_{1-x}As$ shell, with $x_{Al} \approx 0.38$ (the respective Al evaporation rate is $R_{Al} = 0.44$ Å/s). Exemplary results of ultrathin GaAs wires with various AlGaAs shell thicknesses are shown in Fig. 3.7. For comparison, panel (a) shows the pure GaAs core without shell, and panels (b), (c), and (d) nanowires with various shell radii, resulting in total diameters of 70 nm (b), 160 nm (c) and 220 nm (d) and lengths ranging from 2 µm to 3 µm. The wires stem from different growth runs where the duration of shell growth was altered from 8 min (b) to 63 min (c,d). The AlGaAs shell overgrowth time of the nanowires shown in panel (c) and (d) is the same, but in the growth run (d), the V/III ratio was increased from As/Ga = 4 to As/Ga = 8, which led to an increase in both, radial and axial growth rate (note the pronounced tip in (d)). After the shell growth, all nanowires are capped with nominally 5 nm of GaAs to prevent the AlGaAs from oxidation. In total, we produced nanowires with total core/shell diameters ranging from 50 nm to 230 nm as determined by SEM. In order to emphasize the difference to the ultrathin GaAs core diameters, we will refer to the total core/shell diameter as *dielectric* diameter in the further course of this work, as the GaAs core and the $Al_{0.38}Ga_{0.62}As$ shell have similar dielectric constants. We therefore make a clear distinction between the core diameter, relevant for electrons confined to the GaAs, and the diameter relevant for photonic effects, which is the *dielectric* diameter.
Typical photonic effects are for example optical waveguiding or lasing. As we will see in part III, a long conical tip of nanowires with large dielectric diameter can severely deteriorate the properties of such nanophotonic structures. In the next section, we will present first attempts for the MBE growth control of high-diameter nanowires without conical tip formation.

3.3.3 Effect of temperature on the shell growth

In order to inhibit the formation of a conical tip during shell growth, the axial growth must be minimized. One way to obtain untapered nanowires is to synthesize them on a Si(111) substrate using the Ga-assisted growth technique. Here, the a pure Ga droplet acts as catalyst and no Au is needed. During shell growth, the liquid Ga droplet crystallizes to GaAs and allows a pure radial overgrowth, as the VLS mechanism is stopped. However, so far, it has not been possible to synthesize such ultrathin and phase pure WZ GaAs wires, as described in Sec. 3.3.1, with the Ga technique. In this section, we therefore present first attempts to diminish the axial nanowire growth, while the shell growth is in progress, on the basis of the Au-catalyzed NW growth. The major goal is to fabricate high quality optical cavities while maintaining the ultrathin GaAs core. We will use the

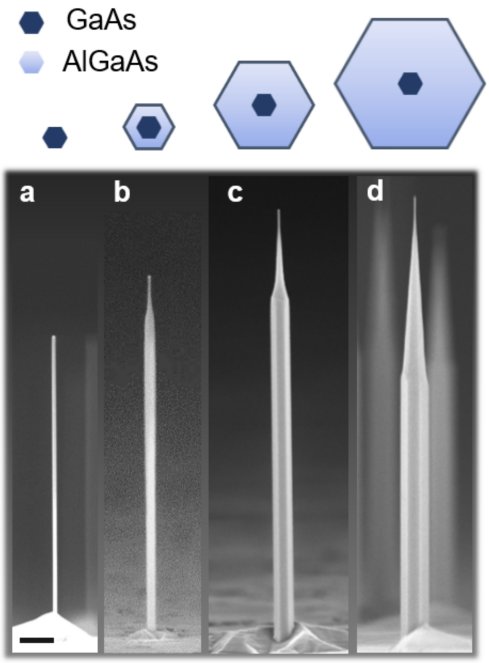

Figure 3.7: Representative SEM image of ultrathin GaAs nanowires from four different growth runs. (a) Pure GaAs core without AlGaAs shell. (b-d) GaAs core overgrown with different AlGaAs shell thicknesses. The total core/shell diameter of the wires amounts to 30 nm (a), 70 nm (b), 160 nm (b), and 220 nm and the lengths range from 2 µm to 3 µm. The conical tip formation at the end facet increases with increasing total core/shell diameter. Scale bar is 250 nm.

temperature during shell growth as major tuning parameter and investigate its effect on the nanowire morphology.
With the usual shell growth temperature of 460 °C, the first approach is to lower the temperature to the point where the Au/Ga droplet becomes solid. Prior to the shell growth, ultrathin GaAs cores are grown under the conditions given in Sec. 3.3.1 (see Fig. 3.8 (a)). Afterwards, a thin $Al_{0.38}Ga_{0.62}As$ shell is grown for 13 min at $T = 460\,°C$ and As/Ga = 4, to ensure a smooth interface between the GaAs core and the AlGaAs shell. The temperature is then further cooled down to $T < 200\,°C$ and the AlGaAs growth continued for 52 min. In this systematic growth series, we found that temperatures above $T \approx 200\,°C$ always lead to the formation of a conical tip. A SEM image of the resulting nanowires is shown in Fig. 3.8 (b). The nanowires exhibit total diameters of 230 – 240 nm and indeed do not exhibit a conical tip, but instead have a irregular shaped lump on top as a result of amorphous crystal growth around the droplet. Additionally, the crystal quality of the shell is relatively poor as the wires do not exhibit smooth side facets and some wires also show irregular parts in the center, as can be exemplarily seen on the righthand side of Fig. 3.8 (b). Representative micro-photoluminescence spectra of a wire from this growth run are shown in Fig. 3.8 (b). This wire exhibits a typical quantum wire luminescence (cf. Ch. 6), with the ground state transition at $\lambda = 814$ nm, and two further, higher energy peaks at $\lambda = 799$ nm and $\lambda = 776$ nm under high excitation. This indicates transitions from higher subbands. Hence, the interface between the GaAs core and the AlGaAs shell is good enough for charge carrier confinement inside the core. However, we can not observe signatures of cavity resonances, which implies that these wires do not form an optical resonator with a quality sufficient to support lasing.

The second approach is to significantly enhance the temperature during shell growth. Harmand *et al.* [60] found, that the VLS mechanism and hence the NW growth is suppressed when the temperature is too high. Very high temperatures can lead to a change in the chemical potentials, such that the particles rather leave the liquid droplet to migrate on the GaAs surface, instead of being absorbed. We aim exploit this during shell growth and enhance the temperature to $T = 580\,^{\circ}\mathrm{C}$ after the core growth is finished. Then, $Al_{0.38}Ga_{0.62}As$ was grown for 130 min. In order to prevent an excessive desorption of the As atoms from the hot substrate surface, the As background pressure was increased to 1.1×10^{-5} Torr, yielding As/Ga ≈ 15. The resulting nanowires have diameters between 290 nm and 350 nm and a hexagonal shape with smooth side facets, as can be seen from the SEM image in Fig. 3.8 (d). The axial growth was not fully suppressed, but in some of the nanowires, the conical tip was much less pronounced as compared to Fig. 3.7 (d). In Fig. 3.8 (e) we plot the high-excitation and low-excitation photoluminescence spectra of one representative wire. Under high excitation (blue spectrum), the equidistant, sharp peaks point towards the formation of resonances from an optical cavity (cf. Ch. 10). Under low excitation, however, these nanowire feature only a small peak at the GaAs bulk bandgap at $\lambda = 820$ nm, but a more intense peak at $\lambda = 765$ nm. This was the case for all investigated nanowires, while the wavelength of the main peak varied from $\lambda = 750$ nm to $\lambda = 770$ nm. We exclude these peaks to arise from higher subband transitions, as none of these wires exhibited typical quantum wire luminescence. We instead suppose that the luminescence arises from the AlGaAs shell itself, with the Al concentration being modified by the high temperature (an AlGaAs bandgap transition at $\lambda = 765$ nm would imply $x_{\mathrm{Al}} = 0.16$), or from defects in the AlGaAs shell, which energetically lie within the bandgap. Nevertheless, the high-temperature approach entails the potential to inhibit the continuation of axial growth. Future studies could for example comprise a thin AlGaAs shell, grown at 460 °C, before raising the temperature, in order to protect the thin GaAs core from degradation at high temperatures.

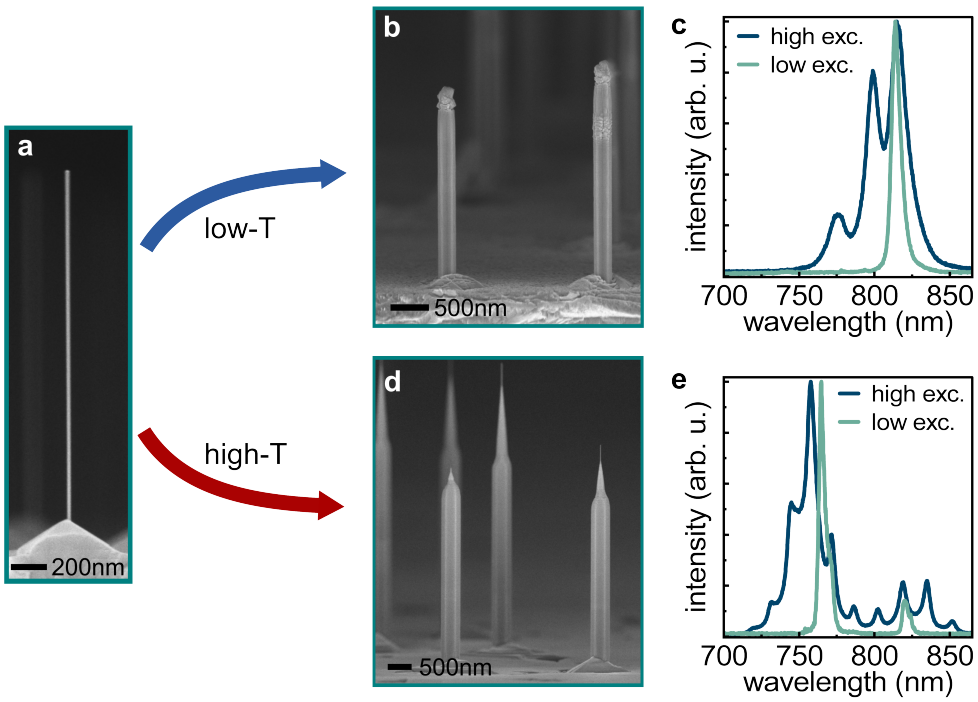

Figure 3.8: Effect of growth temperature on the AlGaAs shell. (a) Ultrathin GaAs core grown under the conditions described in Sec. 3.3.1. (b) SEM image of the nanowires with an AlGaAs shell grown at very low temperature. Instead of a conical tip, the wires exhibit an irregular shaped lump on top. (c) Representative photoluminescence spectra under low and high excitation, showing a typical quantum wire luminescence. (d) Nanowires overgrown with an AlGaAs shell at high temperature. (e) The corresponding photoluminescence spectra indicate resonances from an optical cavity, but no quantum wire luminescence from the GaAs core is observed.

4

Photoluminescence spectroscopy

Luminescence spectroscopy is a powerful tool for material characterization. Throughout the history of semiconductor research, it has been used to investigate the macroscopic optical properties of semiconducting materials as well as microscopic electronic processes [64]. Luminescence differs from other types of radiation, e.g. reflection of light or various types of scattered light. The latter arise from very fast light-matter interactions with virtually no exchange of energy between the radiation and the electronic system of the matter. The luminescence process, on the other hand, is based on the absorption of excitation energy, whereupon an electron is excited and lifted from its equilibrium to a higher energy state. After cessation of the excitation, the excited electron relaxes into the lower energy, equilibrium state and the excess energy is radiatively emitted in form of a photon. This relaxation is known as *spontaneous emission* and the duration of this process is determined by the spontaneous emission lifetime of the excited state The retarded time-scale of the luminescence process strongly distinguishes it from the afore-mentioned, quasi-instantaneous radiation types. Among the various kinds of luminescence (electroluminescence, bioluminescence, cathodoluminescence, ...), which are named after the type of excitation, the relevant one for this thesis is the process of *photoluminescence*, where the excitation energy is provided by the absorption of a photon. In this chapter, we therefore describe the fundamentals behind the photoluminescence process in semiconductors and the underlying mechanism of spontaneous emission. Furthermore, the experimental implementation of single-wire photoluminescence (PL) spectroscopy as well as the technique of time-resolved measurements are presented.

4.1 Principle of photoluminescence in semiconductors

In a photoluminescence (PL) experiment, the excitation of an electron takes place by absorbing a photon from an external source. This source is usually monochromatic light from a laser with larger energy than the bandgap of the material. The PL process in a direct-bandgap semiconductor is sketched in Fig. 4.1 (a). When the material is illuminated with light of energy $E_{\mathrm{exc}} > E_{\mathrm{g}}$, whereby E_{g} is the bandgap energy of the semiconductor, an electron is lifted from the valence band (VB) to the conduction band (CB), leaving behind a positively charged vacancy, or *hole*, in the VB. The energy of the created electron-hole (e-h) pair equals the energy of the excitation photon $E_{\mathrm{exc}} = \hbar\omega'$. Afterwards, both particles are directed towards the respective band extrema (CB minimum for the electron, VB maximum for the hole) by relaxation processes. Once they have reached the energy minimum at $\mathbf{k} = 0$, electron and hole recombine under emission of a luminescence photon with an energy $E_{\mathrm{g}} = \hbar\omega$. Note, that the wavevector $\mathbf{k}$ of a photon is negligible compared to the typical momenta of electrons. Thus, in the single-particle representation in Fig. 4.1 (a), the photon absorption or emission process, respectively, is illustrated as vertical transition in $\mathbf{k}$-space.
During the e-h recombination, the electron thus *spontaneously* undergoes a transition from the excited state to the ground state. The term "spontaneous" thereby reflects the probabilistic nature of the transition with the exact moment of the event being impossible to predict. Let us now focus more deeply on the process of spontaneous emission. A measure of the probability of this spontaneous process was given in 1916 by Einstein's A coefficient [65], which gives the rate at which an electron in a higher energy state will spontaneously decay into a lower energy state. The inverse of this rate therefore describes the lifetime of the excited state. The first person to describe this coefficient from first principle was Paul Dirac in 1927 within his newly formulated quantum theory of radiation in 1927 [66, 67], a cornerstone for the field of quantum electrodynamics (QED). Before that, spontaneous emission was long thought to be an inherent and unchangeable property of the respective emitter. However, it is now understood that spontaneous emission arises due to an interaction of the emitter with the electromagnetic environment, which has the zero-point energy of the quantized radiation field [68]. According to Fermi's golden rule, the rate of an emission process is governed by the density of final states available for a photon to emit into. In the case of emission into free space, the photon is emitted into a continuum of states, as schematically illustrated in Fig. 4.1 (b) (assuming a two-level electronic system), with the density of photon states in free space being proportional to ω^2 [69]. A first expression of the exact rate of spontaneous emission into free space was calculated by Weisskopf and Wigner [68, 70]:

$$\Gamma_0 = \frac{\omega^3 \mu_{12}^2}{3\pi\epsilon_0\hbar c^3}, \tag{4.1}$$

where $\hbar\omega$ is the energy difference between the initial and the final electronic state, ϵ_0 the

vacuum permittivity, c the speed of light and μ_{12} the dipole matrix element between the two states.
The photon density of the vacuum field, however, does not necessarily have to be continuous. Instead, it can be modified, as it is the case, for example, in nanophotonic structures like photonic crystals. When an emitter is placed into an altered electromagnetic environment, the rate of emission is modified to

$$\Gamma_{\mathrm{g}} = \frac{2\pi\mu_{12}^2 E_0^2}{\hbar^2}\rho(\omega). \tag{4.2}$$

Here, E_0 is the electric field, generated by a single photon at the location of the emitter and $\rho(\omega)$ the electromagnetic local density of states (LDOS) at frequency ω. Consequently, the rate of the transition is determined by the number of available photon states and the electric field strength of the emitter [71]. The first proposal of modified spontaneous emission came by Edward Purcell in 1946. He suggested that the emission rate of an emitter can be altered, or even controlled, by placing it into a resonant optical cavity [10]. The change in emission rate of an emitter in the cavity compared with the free space rate is commonly known as *Purcell factor* and given by [72]

$$F_{\mathrm{p}} = \frac{\Gamma_{\mathrm{g}}}{\Gamma_0} = \frac{3Q\lambda^3}{4\pi^2 V_0}, \tag{4.3}$$

where λ is the wavelength, Q the cavity quality factor and V_0 its volume. According to this formula, the emission rate is increased when the light is confined into small dimensions and stored there for a long time [68]. Although Purcell did not explicitly state this, the cavity's role is to modify the LDOS [73].
Not only can the emission rate be enhanced by a cavity, it can also be significantly suppressed. In his seminal work [74], Yablonovitch proposed, that the periodic modulation of the electromagnetic environment opens up an electromagnetic, or *photonic* bandgap, which rigorously inhibits the spontaneous emission of an emitter that is placed inside. Together with the work of John [75], this opened up the extensive research field of photonic crystals. Via the coupling of a single emitter to a photonic crystal, both enhancement and suppression of spontaneous emission rate were demonstrated (c.f for example Refs. [76, 77]). Our NWs in particular have demonstrated a drastic increase in spontaneous emission lifetime in dielectrically thin nanowires by almost two orders of magnitude, as a result of reduced LDOS [12].
Another popular example of modified spontaneous emission is to place an emitter in the vicinity of a mirror, or a metal surface [73, 78, 79]. Regarding the emitter as a electric dipole and the metal as perfect conductor, the emitted radiation is reflected at the interface and reversely interferes with the dipole. Depending on whether the reflected field is in phase or out of phase with the oscillating dipole, the emitter is driven or damped. This can also be seen as varying LDOS as a function of distance to the metal interface.
Summarizing all the methods of modified spontaneous emission by engineering the LDOS, it may be more appropriate to regard spontaneous emission as a form of stimulated

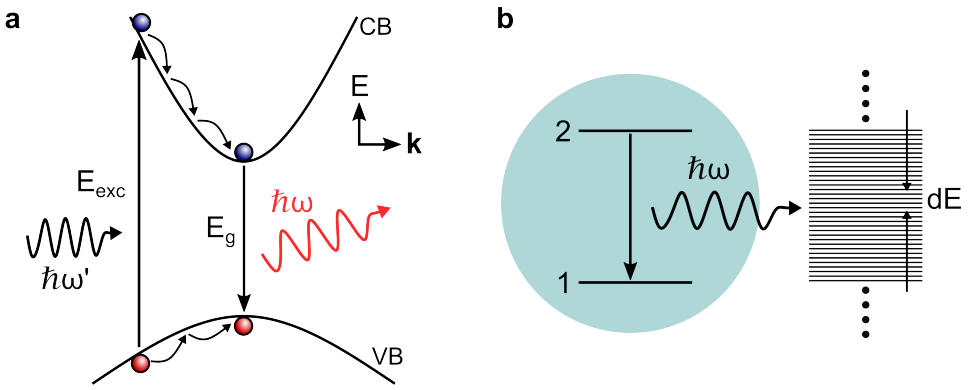

Figure 4.1: Principle of photoluminescence. (a) Schematic of the PL process in a direct-bandgap semiconductor. The absorption of an incident photon with energy $E_{\mathrm{exc}} > E_{\mathrm{g}}$ lifts an electron from the valence band to the conduction band. The created e-h- pair undergoes relaxations processes that directs the two particles towards the respective band extrema. The excited state *spontaneously* decays under emission of a photon with energy $\hbar\omega = E_{\mathrm{g}}$. (b) When the emitter is in free space, this photon is emitted into a continuum of states, determined by the density of photon states. This density can be altered by changing the electromagnetic environment of the emitter, which consequently influences the probability of the electronic transition. Subfigure (b) is adapted from Ref. [69].

emission, with the stimulus being the (modified) vacuum. In general, there is a strong motivation to control spontaneous emission of a system, meaning to either entirely suppress it when it is not desired or, alternatively, engineer it to a useful form [71]. In lasers, for example, spontaneous emission, which does not couple to the lasing mode, raises the threshold and therefore limits their performance. In this regard, there is an extensive field of research on the optimal design of nanolasers, tailored to control spontaneous emission [80]. This aspect will have a greater relevance in part III of this thesis.

4.2 Spectroscopy methods

4.2.1 Single wire μ-PL spectroscopy

All PL spectra presented in this thesis were recorded in the confocal μ-PL setup, shown in Fig. 4.2. The excitation was provided by dual mode lasers operating in continuous-wave (cw) or pulsed mode. In this thesis, we use different lasers with excitation energies of 1.8 eV (690 nm) or 3.1 eV (405 nm), a pulse width of FWHM $\approx$ 50 ps and variable repetition frequencies. The intensity of the laser light can be damped by either inserting neutral density (ND) filter into the excitation path (blue trace in Fig. 4.2), or by regulating

the current supply on the laser controller for a finer adjustment. Additionally, a half-wave ($\lambda/2$) plate in the beam path allows us to rotate the linear polarization of the excitation laser. The laser is then directed via a 90:10 (R:T) beam splitter towards an optical microscope objective, which focuses the laser onto the sample. Depending on the experiments, two different objectives, with either 20× (NA = 0.45) or 100× (NA = 0.8) magnification, are used, resulting in spot diameters of around 5 µm and 1 µm, respectively. To study the optical properties of our NWs at low-temperatures, all samples are mounted into a continuous-flow cryostat, cooled with liquid He_4 to obtain a nominal temperature of 4.2 K. The cryostat is attached to a x-y-z piezoelectric translation stage to precisely the sample with respect to the laser excitation area and to enable a spatial fine mapping of the emitted PL.
The PL signal is collected by the same objective and directed towards the detection part of our setup, while the excitation laser is spectrally filtered from the emission by a optical longpass filter. A CMOS camera captures the real-space image of the microscope and serves to orientate on the investigated samples. For that purpose, an infrared LED optionally provides a spatially broad illumination of the samples. To record the time-integrated PL spectra, the emitted signal is focused onto the entrance slit of a spectrometer, which is equipped with a liquid nitrogen-cooled CCD array on the exit slit to record the spectrally resolved signal. Polarization-resolved measurements are obtained by inserting a linear polarizer into the detection path, as shown in Fig. 4.2. Furthermore, an additional mirror is used to direct the PL signal to an avalanche photodiode (APD), where a temporal resolution is provided by the method of time-correlated single photon counting (TCSPC), which is explained in more detail in the next section.

4.2.2 Time-resolved measurements

Time-resolved PL spectroscopy is a powerful analysis tool to gain insights about charge carrier dynamics. Detecting the dynamics of a PL process requires to record the intensity of the emitted PL upon excitation at different times. TCSPC is thereby a well-established technique for time-resolved luminescence measurements. The principle is sketched in Fig. 4.3. The method is based on a repetitive and precisely timed registration of single photons, with the excitation pulse serving as reference (cf. Fig. 4.3 (a)). According to the principle of a stopwatch, the time difference between the laser pulse and the incoming photon is measured by fast electronics and converted into a digital signal. In our setup, the reference (sync) signal is available from the laser controller when the laser operates under pulsed mode and the single photon detection takes place via an avalanche photodiode (APD). After both photon events (excitation and emission) are converted into an electrical signal, the time information is stored in form of time bins. These time bins are sorted in a histogram with the width of the bins being the minimum time resolution of the stopwatch, which is 25 ps in our instrument. It should be noted that, according to the principles of quantum physics, the occurrence of a photon is entirely random, as it is for the individual stopwatch readings [81]. The TCSPC method can therefore be seen as an account for photon statistics solely based on probabilities. After many cycles, the histogram reveals a

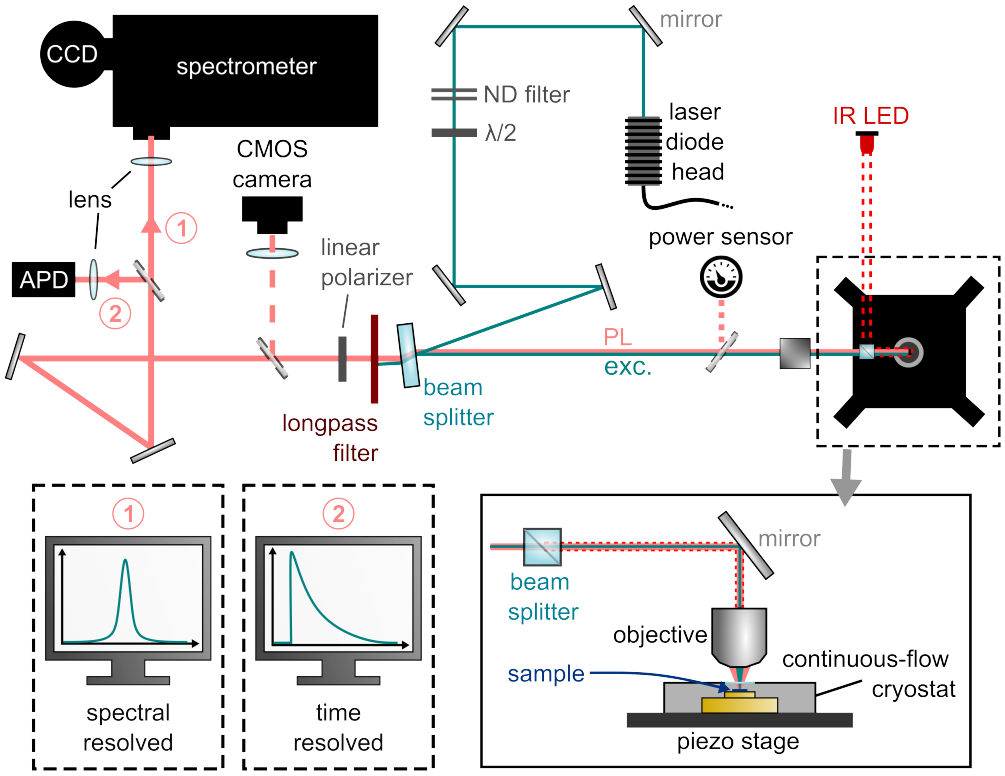

Figure 4.2: Schematic of the confocal µ-PL setup used in this work. The excitation is provided by different laser diodes, able to operate in cw or pulsed mode. The laser light is focused through an optical microscope objective onto the NW samples. The latter are mounted into a continuous flow cryostat. The PL signal is then either directed to a CMOS camera, capturing the microscope image, a spectrometer, which provides the spectral resolution, or to an APD to detect the time-resolved signal.

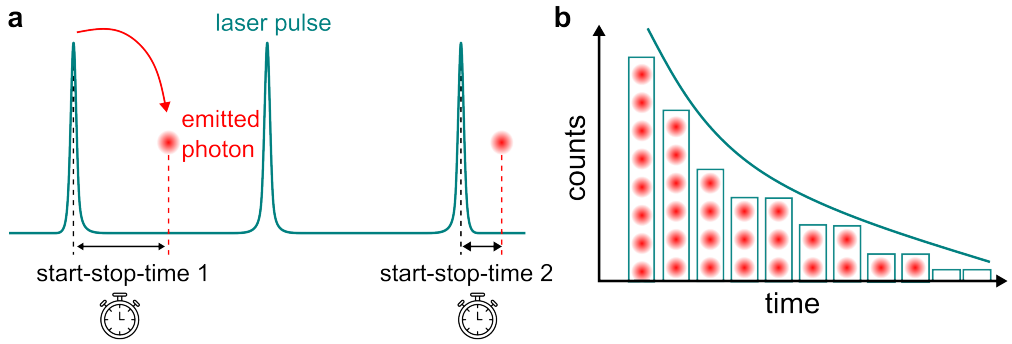

Figure 4.3: Principle of TCSPC, used for time-resolved measurements. (a) The method is based on a stopwatch principle which measures the time between the laser pulse (excitation) and an emitted, single photon. (b) All the recorded timing events are then statistically piled up in a histogram, which registers the probability of a photon being emitted after a certain time. The resulting histogram after multiple cycles then portrays the, typically exponential, decay curve of the investigated system. Adapted from Ref. [81].

decrease in the number of counts at later times, resulting in a typical exponential decay curve for the registered photon events, as sketched in Fig. 4.3 (b). As the method is based upon the detection of single photons, the requirement of single photon probability is obtained by attenuating the emitted PL signal to the necessary extent by ND filters, which are inserted into the detection path.

II Optical spectroscopy on quantum wires

5

The 1D quantum regime

5.1 One-dimensional subband formation

5.1.1 Quantum mechanical description

Speaking of one-dimension means to trap electrons or holes inside a potential well such that only one dimension is left for free movement. The confinement along the other two dimensions then causes a quantization of the particle's kinetic energy, which is particularly dependent on the dimensions and geometrical shape of the potential well. We now want introduce the essential, quantum mechanical features and properties of an electronic 1D system. A more precise treatment incorporating the hexagonal cross section and in particular the crystalline structure of wurtzite is presented at a later stage of this thesis. We will give a course approximation by treating our nanowires as infinitely long cylinders with radius a, having infinitely high potential barriers, so that

$$V(r,\theta) = V(r) = \begin{cases} 0 & \text{for} \quad r < a \\ \infty & \text{for} \quad r \geq a \end{cases}. \tag{5.1}$$

We denote z as the cylinder's long axis and hence the direction of free motion, as sketched in Fig. 5.1(a). Using polar coordinates, the two-dimensional, time-independent Schrödinger equation can then be written in the form [39, 82, 83]

$$-\frac{\hbar^2}{2m_\perp}\left(\frac{\partial^2}{\partial r^2} + \frac{1}{r}\frac{\partial^2}{\partial r} + \frac{1}{r^2}\frac{\partial^2}{\partial \theta^2}\right)\psi(r,\theta) = E\psi(r,\theta), \tag{5.2}$$

where $m_\perp$ is the particle mass perpendicular to the long axis. The wavefunction can be separated into a radial and an angular part and thus be written as $\psi(r,\theta) = R(r)\Theta(\theta)$.

The normalized angular part then has solutions in the form

$$\Theta_l(\theta) = \frac{1}{\sqrt{2\pi}} \exp(il\theta). \tag{5.3}$$

The requirement that the wavefunction has to be single-valued premises the angular part to return to the same value when adding 2π, such that $\Theta_l(\theta) = \Theta_l(\theta + 2\pi)$, which restricts the angular momentum quantum number to integer values: $l = 0, \pm 1, \pm 2, \ldots$. Equation 5.2 is then reduced to

$$\left[-\frac{\hbar^2}{2m_\perp} \left(\frac{d^2}{dr^2} + \frac{1}{r}\frac{d}{dr} \right) + \frac{\hbar^2 l^2}{2m_\perp r^2} \right] R(r) = ER(r). \tag{5.4}$$

When we replace E by $k = \sqrt{2mE}/\hbar$, we can rewrite Eq. 5.4 to

$$r^2 \frac{d^2u}{dr^2} + r\frac{du}{dr} + \left[(kr)^2 - l^2 \right] R = 0. \tag{5.5}$$

This is known as Bessel's equation with solutions $J_l(kr)$ and $Y_l(kr)$, which are the Bessel functions of order l of the first and second kind, respectively. Given that the Bessel function of second kind $Y_l(kr)$ diverges at the origin, only first kind Bessel functions $J_l(kr)$ are considered as solutions. In addition, due to the infinitely high potential walls, the wavefunction must vanish at $r = a$, thus requiring $J_l(ka) = 0$, which is fulfilled for every n-th zero $j_{l,n}$ of the Bessel function with $n = 1, 2, \ldots$. Hence, the allowed wave vectors amount to $k = j_{l,n}/a$, resulting in wavefunctions and eigenenergies of

$$\Phi_{l,n}(\mathbf{r}) \propto J_l \left(\frac{j_{l,n} r}{a} \right) \exp(il\theta) \qquad \text{and} \qquad \varepsilon_{l,n} = \frac{\hbar^2 j_{l,n}^2}{2m_\perp^2 a^2}, \tag{5.6}$$

with $\varepsilon_{l,n}$ being the bottom of each subband. This leaves us with the total energy of charge carriers in a 1D system of

$$E = \varepsilon_{l,n} + \frac{\hbar^2 k_z^2}{2m_\parallel}. \tag{5.7}$$

The second term thereby describes the free motion of charge carriers along the z-direction with their parallel mass $m_\parallel$. The lowest four subband energies $\varepsilon_{l,n}$ with the radial part of their corresponding wavefunctions are sketched in Fig. 5.1 (a).
With Eq. 5.6 we can now calculate the subband energies in dependence of the nanowire diameter $d = 2a$ in this approximation. The results for the five lowest energy states for electrons $e_{l,n}$ and holes $h_{l,n}$ are plotted in Fig. 5.1 (b), where we used the effective masses $m_{\perp,e} = 0.075\, m_0$ and $m_{\perp,h} = -0.12\, m_0$, taken from Ref. [84]. In PL spectroscopy however, we are rather interested in the interband transition energy between the electron and the hole states, i.e. $e_{l,n} - h_{l,n}$, which is plotted in (c) for the most probable transitions with coinciding quantum numbers l as a function of wire diameter. Below a diameter of ~ 40 nm, the curves increase very steeply with decreasing diameter. This highlights that, in the range below 40 nm, a small variation in diameter causes a strong change in

confinement energy. In the later course of this work, it will be useful not to determine a particular diameter dependence, but rather the energy splitting of the subbands with respect to *each other*. It is obvious from Eq. 5.6 that all subbands follow the same diameter dependence $\varepsilon_{l,n} \propto 1/a^2$ and only differ in a certain prefactor depending on $j_{l,n}$. We graphically depict this in Fig. 5.1 (d) where we plot the interband transition energies of higher states, as shown in (c), as a function of the lowest possible subband transition $e_{0,1} - h_{0,1}$. All transition energies from higher states increase linearly with the lowest energy, or ground state transition, respectively and only differ in their slope. This observation is helpful in determining whether peaks in optical spectra result from subband transitions, without the need for knowing the exact diameter.

5.1.2 Density of states in low-dimensional systems

The spatial quantum confinement described above also leads to significant variations in the density of states (DOS) of a 1D system compared with bulk or two-dimensional semiconductors. By contrast with the square-root shape and the step-like behavior of a 3D or 2D system, respectively, the DOS in a 1D quantum object scales with $\sqrt{1/E}$. The explicit form of the one-dimensional DOS (per unit length) for an infinitely high potential well is given by

$$n_{1\mathrm{D}}(E) = \sum_{l,n} \frac{1}{\pi\hbar}\sqrt{\frac{2m}{E - E_{\mathrm{gap}} - \varepsilon_{l,n}}}\Theta(E - E_{\mathrm{gap}} - \varepsilon_{l,n}), \tag{5.8}$$

thus having singularities at each subband minimum $\varepsilon_{l,n}$. At these points, the 1D DOS clearly exceeds those of a 3D or 2D structure, as it is sketched in Fig. 5.2, which is advantageous in many applications, e.g. lowering the threshold of lasers. The parameter that guarantees the energy conservation when describing interband transitions with Fermi's golden rule is then given by the *joint density of states* (jDOS), which determines the number of electronic states in the conduction and valence band that are separated by a certain energy and is therefore strongly related to optical absorption spectra [64]. In other words, the jDOS tells us the number of states available for photons to interact with. As the DOS in Eq. 5.8 is valid for quantum confined subbands in both, the conduction and the valence band, the $1/\sqrt{E}$ energy-dependence, shown in Fig. 5.2, is also present in the jDOS.

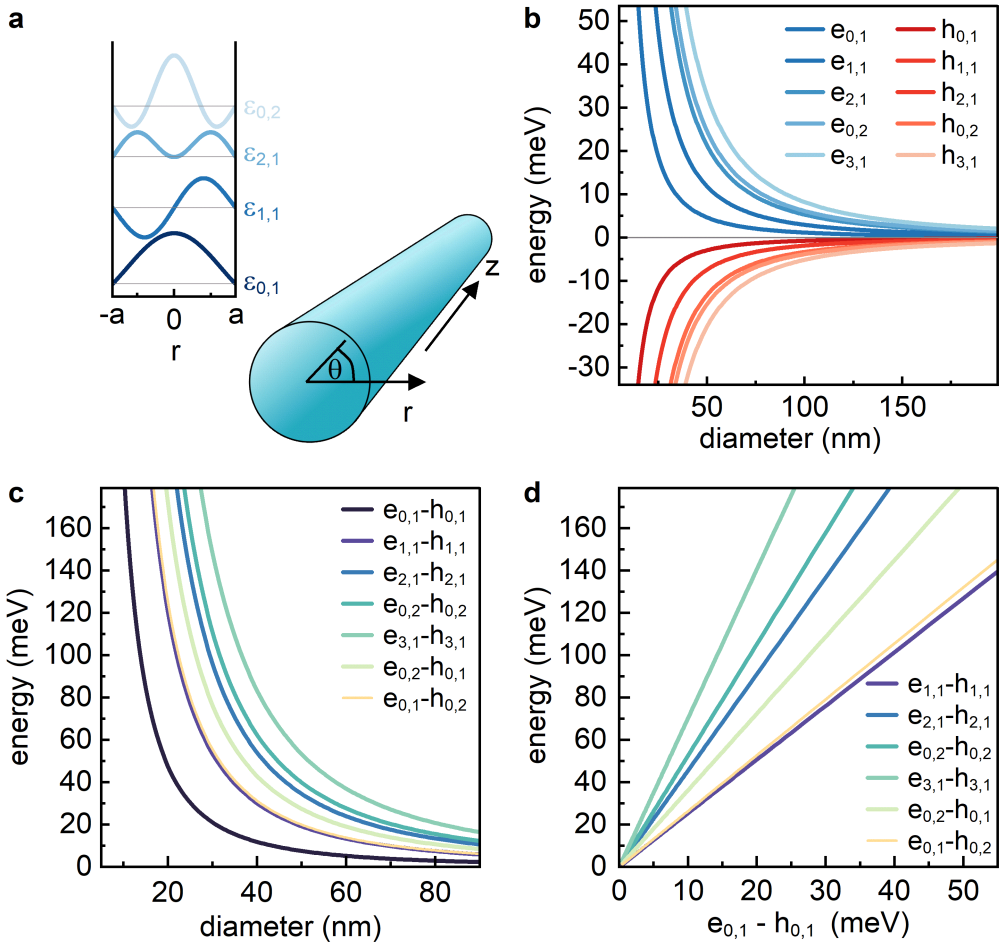

Figure 5.1: Subband formation in 1D quantum systems. (a) Schematic illustration and coordinate system of a quantum wire with circular cross section (right) and the corresponding first four wavefunctions with eigenenergies $\varepsilon_{l,n}$ (left) inside a quantum wire with radius a. (b) Diameter-dependent eigenenergies of the first five electron and hole states $e_{l,n}$ and $h_{l,n}$, respectively. (c) Possible transition energies between electron and hole states with the same quantum numbers l as a function of wire diameter. (d) Same transition energies as in (c), but as a function of the lowest transition $e_{0,1} - h_{0,1}$ in order to highlight the linear dependence between the energy states.

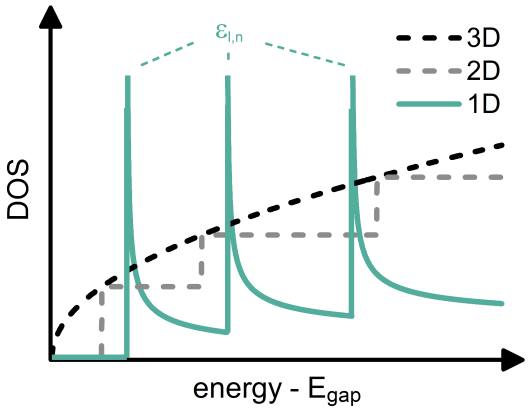

Figure 5.2: One-dimensional density of states (turquoise) in comparison with those of a 3D and 2D electronic structure (black and gray dashed lines, respectively). The 1D DOS has maxima at the subband eigenenergies $\varepsilon_{l,n}$.

5.2 Optical transitions in wurtzite GaAs quantum wires

As discussed in Sec. 2.2, in wurtzite GaAs the degeneracy of the heavy-hole (hh) and the light-hole (lh) valence bands is lifted. The energy of the light-hole to conduction band (el) transition is about 100 meV larger than the transition from the bottom of heavy-hole valence band [28, 30, 53, 85]. The symmetry of the valence bands then furthermore leads to polarization anisotropies of optical transitions. We now discuss the polarization selection rules in wurtzite GaAs including size quantization effects in the electronic 1D regime. Figure 5.3 (a) sketches the electronic dispersion $E(k_z)$ of a quantum wire when the bands are split into subbands and the z-direction is the direction of free motion. The sketch is based upon the band structure calculations in Ref. [17] and illustrates optical transitions between the valence and conduction subbands in vicinity of the Γ-point. While optical transitions from valence subbands with dominant hh character (red) are primarily polarized perpendicular to the wire axis, transitions from subbands with lh character (blue) can occur in both directions of polarization. Hence, the character of the involved subbands can be expected to strongly affect the polarization behavior of experimental emission or absorption spectra, respectively. Accordingly, in Fig. 5.3 (b) we show a calculated, polarization-resolved absorption spectrum of a wurtzite GaAs wire with 26 nm core diameter. The calculations are performed by Dr. Paulo E. Faria Junior within the scope of our collaboration, which is also presented in Ref. [86]. The band structure is calculated via the $\mathbf{k}\cdot\mathbf{p}$ framework under consideration of the hexagonal quantum confinement. In order to properly model the intrinsic polarization anisotropies of optical transitions, the valence band Hamiltonian includes band-mixing effects of heavy, light and crystal field split-off holes and the conduction band is treated with a parabolic dispersion. The absorption spectra are then calculated by

$$\alpha^a(\hbar\omega) = C_0 \sum_{c,v,k_z} \left| p^a_{cvk_z} \right|^2 F_{cvk_z}\, \delta\left(\hbar\omega_{cvk_z} - \hbar\omega\right), \tag{5.9}$$

in which the superindex a refers to the light polarization in perpendicular x- or parallel

z-direction, respectively, the indices c and v label the conduction and valence subbands and k_z is the wave vector along the wire axis. $p^a_{cvk_z} = \langle c, k_z | \mathbf{p} \cdot \hat{a} | v, k_z \rangle$ is the dipole matrix element for the polarization of the light $\hat{a}$, incorporating the valence band mixing and anisotropic Kane parameters [87, 88], $F_{c,v,k_z} = \left(f_{v,k_z} - f_{c,k_z}\right)$, where f_{v,k_z} and f_{c,k_z} are the Fermi-Dirac distribution for the electron occupancy in the valence and conduction subbands, $\hbar$ the Planck's constant, ω_{cvk_z} is the interband transition frequency and δ the Dirac delta function. The constant C_0 is given by $C_0 = 4\pi^2 e^2/(c n_r \epsilon_0 m_0^2 \omega \Omega)$ with the electron charge e, the speed of light c, the refractive index of the material n_r, the vacuum permittivity ϵ_0, the free electron mass m_0 and the nanowire volume Ω. In the calculation, undoped systems at nearly zero temperature are assumed, so that $(f_{v\mathbf{k}} - f_{c\mathbf{k}}) = 1$. The broadening due to finite carrier lifetimes was taken into account by replacing the Dirac delta function by a Lorentzian function with a full width at half-maximum of 5 meV. More specific details on the calculations can be found in Ref. [86] and the references therein.

The calculated spectra of the 26 nm wire in Fig. 5.3 (b) are structured by the typical Van-Hove singularities of a one-dimensional jDOS, here weighted by allowed optical interband transitions constituted by the dipole matrix element for light polarizations in perpendicular x- (red) or parallel z-direction (black). The singularities are resonances of the optical transitions highlighted by the arrows in Fig. 5.3 (a). The energy is scaled with respect to the bulk bandgap of wurtzite GaAs, set to $E_{\text{gap}} = 0$. The polarization anisotropies due to the band symmetries are directly seen in this calculated spectrum. In the energy range below ~120 meV, perpendicular polarized transition outweigh in the spectrum, which directly underlines the dominant hh-character of the involved subbands. The absorption of parallel light intensifies when the energy of the first resonance of a light-hole type subband is reached, which is at ~125 meV above the bulk bandgap in the 26 nm wire presented here. Comparing the overall intensity of the two spectra over the entire presented energy range, up to 200 meV above the wurtzite bulk bandgap here, Fig. 5.3 (b) predicts the absorption and emission to be dominated by perpendicular transition dipoles.

Understanding the optical properties and anisotropies of the wurtzite band structure is crucial when wurtzite nanowires are analyzed in optical spectroscopy. The calculations therefore form a marvelous testbed for verifying experimental observations. The large energetic distance between the individual subbands in this 26 nm wurtzite quantum wire, a diameter which is experimentally feasible by our growth technique [16, 53], motivates us to study such wires in high-excitation photoluminescence (PL) spectroscopy.

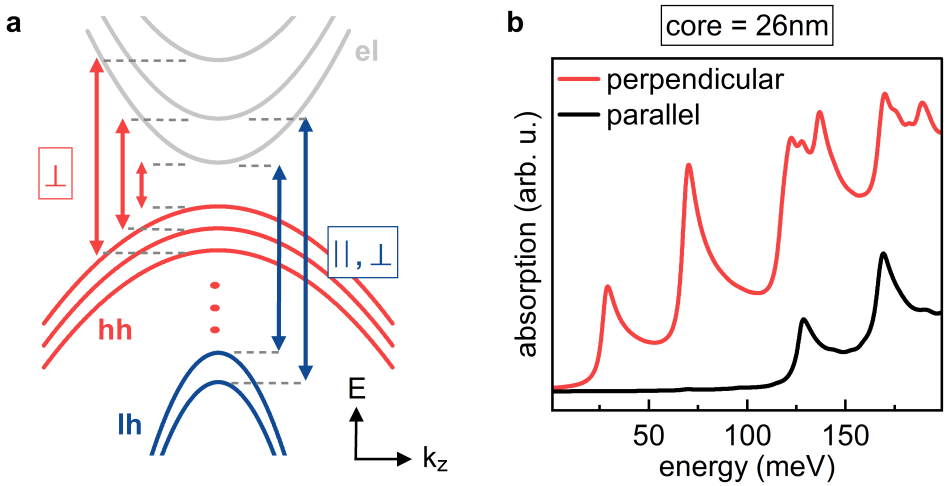

Figure 5.3: Polarization selection rules in 1D confined wurtzite GaAs. (a) Sketch of the subband dispersion resulting from size quantization. The electronic conduction band (gray) and the non-degenerate heavy hole (red) and light hole (blue) valence bands are split into subbands. The arrows indicate the allowed dipole transitions with their respective allowed directions of polarization. (b) Calculated, polarization-resolved absorption spectra of a wurtzite GaAs nanowire with 26nm core diameter, showing typical Van-Hove singularities of a 1D quantum object.

6

Signatures of subband transitions in photoluminescence

6.1 High power photoluminescence spectroscopy of quantum wires

In the previous chapter, we described the effects of 1D quantum confinement on the electronic band structure and the density of states. In absorption, transitions between quantized states manifest as Van-Hove singularities at certain energies above the bulk bandgap which we show in the calculated absorption in Fig. 5.3 (b). As the experimental realization of absorption measurements is difficult in single quantum wire spectroscopy, we investigate our wires by μ-PL spectroscopy via increasing excitation power density, which has been successfully implemented in other systems before in order to observe quantized states [89–94]. Figure 6.1 (a) shows characteristic spectra of a single quantum wire under various excitation intensities, irradiated with a pulsed, 3.1 eV laser diode with 80 MHz repetition frequency. At low excitation, the emission displays a single, narrow PL peak at 1.522 eV. This peak is representative for the ground state emission, here labelled as "1", when all excited carriers relax to the lowest conduction and valence subband, respectively. With increasing excitation power, additional peaks emerge on the high energy side of the spectrum. In this example, up to four peaks arise at the highest excitation level at 1.550 eV, 1.585 eV and 1.629 eV which are marked with numbers "2-4" in the plot. Note that the energetic position of the peaks slightly, but not significantly shift to lower energies, which can be attributed to the renormalization of the bandgap due to many-body effects in the electron-hole system [91]. This effect is more pronounced under continuous-wave excitation which is shown and briefly discussed in the Appendix A.1. We now further analyze these peaks in Fig. 6.1 (b) by plotting the absolute luminescence peak intensities of the transitions marked in (a) as a function of the excitation power. Peak 1 is already saturated at an excitation power of 0.45 W/cm^2 and even slightly degrades at higher powers which may indicate an increase in carrier temperature [90, 91]. Only after

saturation of peak 1, the second peak (peak 2) starts to emerge and amplifies until the third peak appears. The same behavior can be observed between peak 3 and peak 4. Note that the total peak intensities are influenced by the tails of neighboring peaks, which add up as background, especially when the peaks are spectrally broad under high excitation. This background was not subtracted for the individual peaks and causes a further, slight increase in the peak intensity after saturation. The excitation power dependency shown in Figs. 6.1 (a) and (b) for this single wire strongly suggests that the high energy peaks $2-4$ arise from transitions between higher excited subbands. Due to the $E^{-1/2}$ dependence of the density of states of the quantum wire subbands, the transitions in emission remain quite sharp and are visible as discernible peaks [93]. In addition, the finite recombination rate of the charge carriers [12, 53] combined with Pauli exclusion principle [64] leads to band filling and facilitates the occupation of higher subbands for sufficient pumping. In this stage, charge carriers from higher levels can not relax into the lowest energy, or ground state anymore and recombine from higher states. These emitted, high-energy photons can also not be reabsorbed by the saturated, lower-energy states, which promotes their visibility in photoluminescence. The presented behavior is characteristic for all of our studied quantum wires that are grown as described in Sec. 3.3.2 and exhibited an adequate wurtzite structure.

In total, we investigated 37 wires with different total, dielectric diameters on various substrates, all of which exhibited multiple peaks with increasing excitation. The wires were either excited with a 3.1 eV or a 1.8 eV laser diode at 10 - 80 MHz repetition frequency, which did not lead to any differences in the emission behavior. Figure 6.1 (c) summarizes the peak energies observed in the 37 single wires and displays the energies of the peaks 2-4 as a function of the energy of their corresponding ground state emission, peak 1. As mentioned in Sec. 3.3.1, the quantum wire core diameters are statistically distributed between 20-40 nm. In this diameter range, a diameter variation of only a few nanometers leads to a significant change in PL energy as a consequence of enhanced size quantization effects, which is highlighted in Fig. 5.1 and experimentally presented in Ref. [16]. The ground state PL energy of peak 1 therefore continuously increases from 1.515 eV to 1.548 eV with decreasing core diameter. Along with the ground state energy, the energies of the peaks 2-4 also increase steadily, following a linear dependence with the ground state energy as it was discussed in Sec. 5.1.1. The linear dependence is indicated as a guide to the eye for each peak in Fig. 6.1 (b). It is therefore most likely that the peaks are caused by transitions from higher excited subbands. While strong optical pumping of nanowires could also induce the formation of resonances from longitudinal cavity modes, we indeed exclude the emerging peaks to feature cavity resonances. Though each wire in principle geometrically represents a Fabry-Pérot cavity, it would be highly unlikely to observe such similar cavity resonances in 37 wires with different diameters, tip shapes and wire lengths.

For the first time, we spectrally resolve multiple subband transitions in the photoluminescence of single, wurtzite quantum wires, demonstrating significant confinement energies to be realized in our core-shell NWs. This provides an ideal model system for optically pumped studies of excitons and carriers in the 1D quantum limit. Next, we further

investigate of the subband structure regarding the polarization selection rules discussed in Sec. 5.2 for these quantum wires.

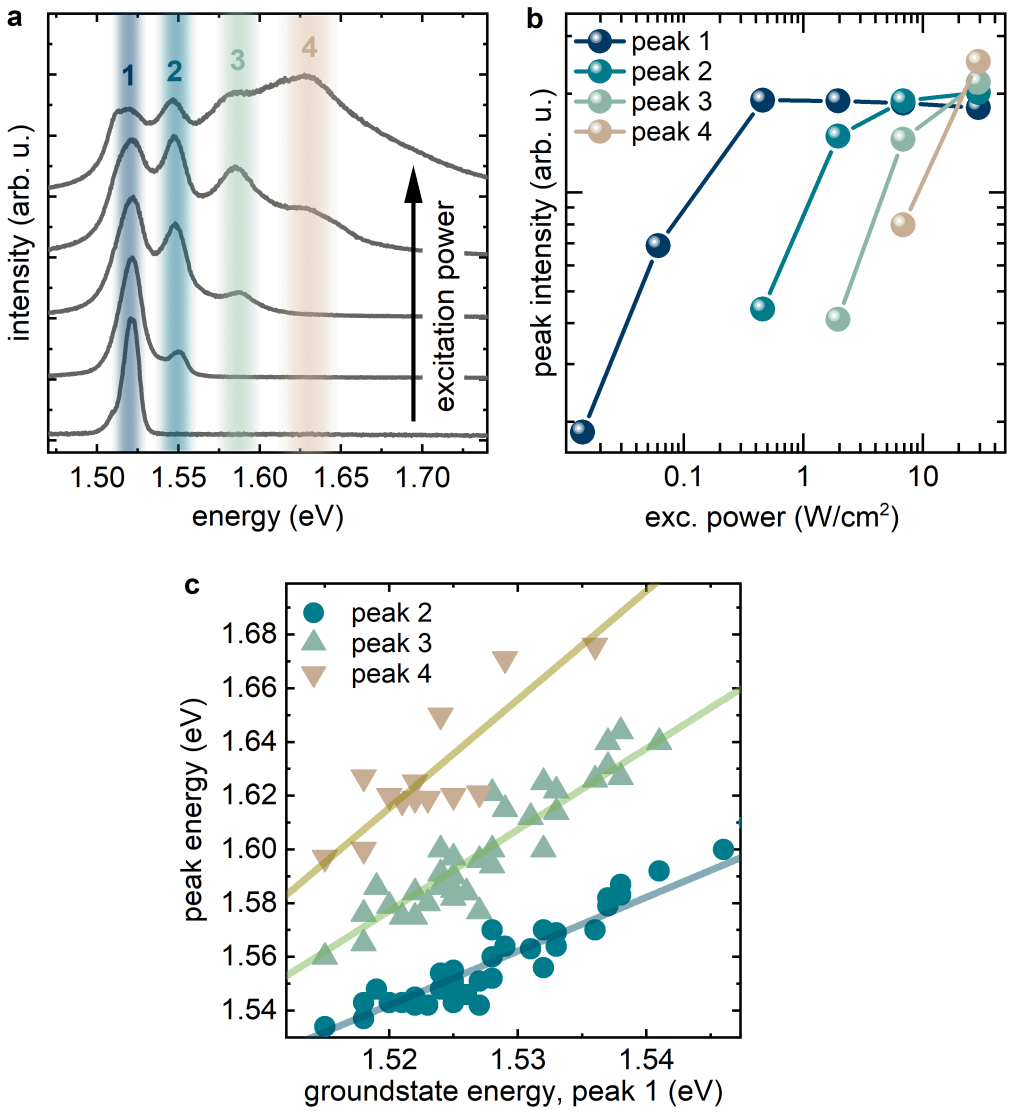

Figure 6.1: Indication of subband filling in quantum wires. (a) Exemplary PL emission spectra (normalized) of a single wire under increasing excitation power. While at low excitation only one narrow peak exists, up to four, well-separated peaks arise at the high-energy side of the spectrum with increasing excitation intensity. The peaks are labeled with numbers 1-4. (b) Intensities of peaks 1-4 as a function of excitation power on a double-logarithmic scale. Higher-energy transitions emerge when the lower states are saturated. (c) Summary of subband energies of the investigated nanowires at high excitation power as a function of the ground state emission energy (peak 1). The linear dependence between the energies are indicative of subband transitions. The lines are guides for the eye.

6.2 Polarization analysis of dielectrically thin quantum wires

In Ch. 5, we discussed the characteristics of the density of states in 1D quantum confined structures and specified the 1D band structure for wurtzite quantum wires, in particular by elaborating on polarization anisotropies for different optical dipole transitions. Experimentally, we demonstrated the observation of up to four subband transitions in the PL emission of our self-assembled wires. We now want to further connect theory and experiment by analyzing these subband transitions by polarization-resolved PL spectroscopy. It should be emphasized that this is a unique possibility to address multiple subband transitions at once, as experimental access to such strong quantum confinement in wurtzite GaAs is rather scarce.
To record polarization-resolved PL spectra, a rotatable linear polarizer was inserted into the detection path of our μ-PL setup, allowing to filter the emission from wires lying on a substrate by perpendicular x-, or parallel z-polarization. A schematic of the setup is shown in Fig. 6.2 (a). We start by analyzing two different wires with both having a comparatively thin AlGaAs shell and total, dielectric diameters of around 60 nm. The wires were excited with an energy of 3.1 eV at 80 MHz repetition frequency under the highest possible excitation power to achieve a high occupancy of quantum wire subbands. Note that we non-resonantly excite our wires with a lot of excess energy and solely concentrate on the polarization of the PL emission. The linear polarization of the exciting laser beam is therefore not relevant for our experiments. Figures 6.2 (b) and (c) show the results of the measured photoluminescence spectra analyzed perpendicular (red) and parallel (black) to the wire axis for quantum wires with a core diameter of 26 nm and 31 nm respectively. Focusing on the perpendicular spectra, both wires reveal three well-separated peaks at energies of E_1 =1.536 eV, E_2 =1.580 eV, E_3 =1.638 eV for the 26 nm wire and E_1 =1.527 eV, E_2 =1.562 eV, E_3 =1.610 eV for the 31 nm wire. The larger energy values of $(E_3 - E_1)$ for the 26 nm wire are in accordance with a larger energy splitting in thinner quantum wires as a result of stronger quantum confinement, as outlined in Secs. 5.1.1 and 6.1. The exact quantum wire core diameters given in the remainder of this chapter are determined by comparing the energetic distance between the PL peaks with those between the Van-Hove singularities in calculated absorption spectra for various diameters, like the one shown in Fig. 5.3 (b). Coming back to the theoretical model on the polarization behavior in wurtzite quantum wires in Fig. 5.3 (b), the calculated absorption spectra predict perpendicular transitions to dominate the spectrum in the presented energy range. Comparing this with the emission spectra of the two wires in Figs. 6.2 (b) and (c), this holds true for the first transition E_1, i.e. the ground state peak in both spectra. Intriguingly, transitions at higher energies, that is from higher excited states, clearly favor the emission of parallelly polarized light. At first sight, this experimental observations deviate from the calculated polarization-resolved analysis in Fig. 5.3 (b), which is solely based on interband transitions from the electronic 1D subband structure. This discrepancy may imply that, besides purely electronic polarization selection rules weighted by the

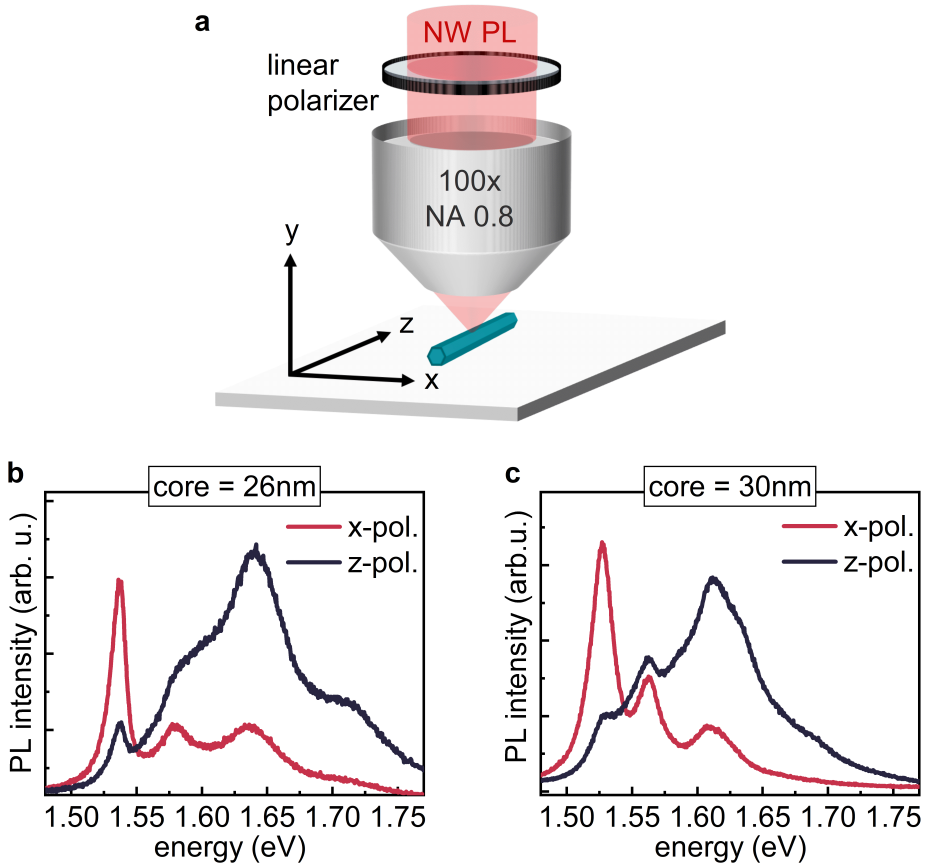

Figure 6.2: Polarization-resolved analysis of dielectrically thin quantum wires. (a) Simplified schematic of the setup for polarization-resolved PL measurements. (b) Experimental PL emission spectra of a 26 nm core quantum wire analyzed perpendicular (x-pol., red) and parallel (z-pol., black) to the wire axis. (c) Respective emission spectra for a quantum wire with 31 nm core diameter.

optical matrix element, also *extrinsic*, or photonic anisotropies in the light polarization must be considered. This will be examined in detail in the next chapter.

7

Photonic polarization anisotropies in nanowires

7.1 The dielectric mismatch effect

The discrepancies in the polarization behavior between thin nanowires in Sec. 6.2 and the calculations in Sec. 5.2 give rise to the assumption that not only *intrinsic* electronic, but also *extrinsic*, photonic anisotropies have to be considered when the polarization behavior of nanowires is studied. Early studies on optical polarization anisotropies in nanowires or quantum wires have focused on lithographically or epitaxially defined wires embedded in a semiconductor medium [95–98]. Self-assembled nanowires, however, either free-standing or lying on a substrate, are subjected to a large refractice index contrast with their environment. In combination with their high aspect ratio, this induces a strong polarization anisotropy of the absorbed and emitted light, which may add to, or possibly even outweigh, the electronic selection rules predicted by the band structure. This *dielectric mismatch effect* can be deduced from classical electrodynamics by treating the nanowire as an infinite dielectric cylinder in a uniform electric field $\mathbf{E^{out}}$ [99]. Inside the cylinder, the magnitude of the field component perpendicular to the long axis is then solely dependent on the relative dielectric constants of the cylinder medium ϵ^{in} and it's surrounding medium ϵ^{out}:

$$E_{\perp}^{in} = \frac{2\epsilon^{out}}{\epsilon^{in} + \epsilon^{out}} E_{\perp}^{out}, \tag{7.1}$$

where $E_{\perp}^{in}$ and $E_{\perp}^{out}$ are the perpendicular electric field components inside and outside the cylinder, respectively [31, 84, 100–102]. At the same time, the parallel field component is continuous at the interface:

$$E_{\parallel}^{in} = E_{\parallel}^{out}. \tag{7.2}$$

In the case of self-assembled semiconductor nanowires, the dielectric constant of the wire

is typically larger than that of the environment, thus inducing a strong reduction of the perpendicular field component inside the wire, while the parallel field remains constant. In the case of $E_{\perp}^{out} = E_{\parallel}^{out}$, Eq. 7.1 yields the attenuation ratio δ:

$$\delta = \frac{I_{\perp}}{I_{\parallel}} = \frac{\left|E_{\perp}^{in}\right|^2}{\left|E_{\parallel}^{in}\right|^2} = \left|\frac{2\epsilon^{out}}{\epsilon^{in} + \epsilon^{out}}\right|^2, \tag{7.3}$$

indicating the suppression of the perpendicular field intensity $I_{\perp} = \left|E_{\perp}^{in}\right|^2$ with respect to the parallel one $I_{\parallel} = \left|E_{\parallel}^{in}\right|^2$. For instance, in a GaAs nanowire with $\epsilon^{in} = 12.4$ [103] surrounded by vacuum ($\epsilon^{out} = 1$), the perpendicular electric field is suppressed by a factor of $\delta = 0.022$ compared with the parallel field. Though Eq. 7.1 was initially derived for static electric fields, it is also applicable for high frequency fields as long as the wavelength of the field is much larger than the nanowire diameter $\lambda \gg d_{NW}$. In practice, in nanowire experiments, the diameter is often comparable to the emission wavelength inside the wire λ/n. We therefore establish a diameter-dependent attenuation value $\delta(d)$ by a more custom-tailored approach using finite-element-method (FEM) simulations, which is presented in the following.

7.2 Estimating the diameter-dependent dielectric mismatch by numerical simulations

Before we further analyze the polarization in our wires with different dielectric diameters, we specify the light attenuation by diameter-dependent, finite-element-method (FEM) based simulations using the modeling software implemented in COMSOL Multiphysics v4.2a. The geometry consists of a $6 \times 6\,\mu m^2$ rectangle divided into two parts: The upper domain is defined as air or vacuum, respectively, with a refractive index of $n_{\mathrm{Air}} = 1$ and the lower domain as SiO_2 with $n_{SiO_2} = 1.45$ [104, 105], simulating the substrate. The nanowire cross section is formed by two concentric hexagons placed in the center of the simulation area, where the inner hexagon represents the GaAs core with a fixed diameter of $d_{\mathrm{core}} = 30\,\mathrm{nm}$ and a refractive index of $n_{\mathrm{GaAs}} = 3.67$, and the outer one the AlGaAs shell with $n_{\mathrm{AlGaAs}} = 3.40$ [106]. The system was excited by launching a plane wave with Gaussian shape from the upper boundary of the simulation area, which was either polarized perpendicular (E_x) or parallel (E_z) with respect to the nanowire axis. To the remaining boundaries, perfectly matched layers (PML) were attached in order to absorb all outgoing radiation and to minimize backscattering from the outer borders. As we want to assess the light suppression of the nanowire *emission*, the wavelength of the source field was set to $\lambda = 800\,\mathrm{nm}$, close to the measured PL wavelength. The geometry of an exemplary result is presented in Fig. 7.1 (a), where the total, dielectric nanowire diameter was set to $d = 60\,\mathrm{nm}$ and the source field is polarized in perpendicular x-direction. The incident light beam is partially reflected and partially transmitted at the air/SiO_2 interface

due to the slight refractive index difference. Figures (b) and (c) highlight the electric field distribution in vicinity of the wire in the case of perpendicular (b) and parallel (c) excitation, respectively. It is clear to see, that the perpendicular electric field in (b) is significantly suppressed inside this 60 nm wire and that the intensity is distributed along the outer side facets, which is reminiscent of a leaky waveguide mode when the wire diameter is thin compared to the wavelength [12, 107]. In contrast, under the same configuration, but now with a parallelly polarized source field in (c), the electric field inside the wire is apparently slightly enhanced. These two results display very well the strong polarization anisotropy in dielectrically thin wires due to the dielectric mismatch effect. In order to quantify this and to get the diameter dependence, we varied the size of the AlGaAs shell while keeping the GaAs core fixed at a diameter of 30 nm. Equivalent to the scenarios in Figs. 7.1 (a-c), we then performed a diameter sweep in the range of $d = 40 - 400$ nm for both directions of polarization. As the detected photoluminescence only occurs inside the GaAs core, we integrated the resulting electric field over the core domain (normalized to the core area) for each dielectric diameter and polarization. The results are plotted in Fig. 7.1 (d) as dashed lines. In particular for diameters below ~ 150 nm, the differences between the integrated perpendicular (dark blue) and parallel (light blue) electric fields are striking. While the perpendicular electric field inside the core is minimal, the parallel field even exceeds unity with a maximum at $d = 70$ nm. Above $d = 150$ nm, the curves deliver similar values and start to oscillate around unity at larger dielectric diameters. These oscillations can be explained by total internal reflection at the nanowire side facets, resulting in resonances at specific diameters with field maxima in the core region (see also Appendix A.2). According to Eq. 7.3, we can then calculate the diameter-dependent attenuation value

$$\delta(d) = \frac{I_\perp(d)}{I_\parallel(d)} = \frac{\left|E_\perp^{\text{core}}(d)\right|^2}{\left|E_\parallel^{\text{core}}(d)\right|^2}, \tag{7.4}$$

defining the light suppression inside the NW core (green curve in (c)). With a minimum at $\delta(70\text{nm}) = 0.015$, the attenuation value even falls below the classically determined δ-value calculated in the previous section for a thin GaAs wire in the limit $d \ll \lambda$. At larger diameters, however, $\delta(d)$ approaches unity at around 260 nm, so that the emission and absorption becomes almost unpolarized. Note that the oscillations with different phases of $|E_\perp|$ and $\left|E_\parallel\right|$ also leads to an oscillating $\delta(d)$.

Though our FEM model technically speaking simulates an absorption event, our results are bearing strong analogies with the theoretically approached *emission* case established by Ruda et al. [108] (see also Fig. A.2 (a)). We therefore conclude that the obtained δ-values are valid for both absorption and emission events, especially in the given configuration, as the excitation and detection paths are alike and geometrically coincide with the presented simulation. Hence, we are able to distinguish between absorption and emission polarization anisotropies by solely replacing the wavelength at which the simulation is solved.

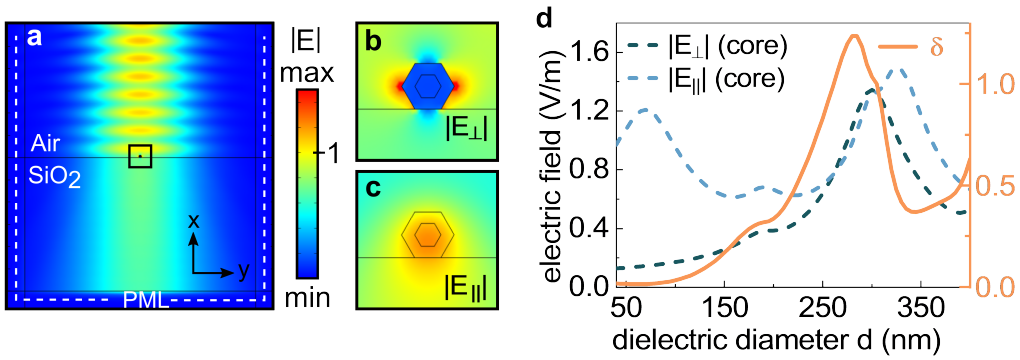

Figure 7.1: Numerical FEM simulation to estimate the diameter-dependent dielectric mismatch effect. (a) Normalized electric field distribution of the system when excited by a perpendicular, x-polarized wave of Gaussian shape, launched from the upper boundary of the simulation area. (b) Electric field distribution in the vicinity of the nanowire with a dielectric diameter of $d = 60\,\text{nm}$ when the system is excited by a perpendicular, x-polarized wave. (c) Respective solution when the system was excited by a parallel, z-polarized wave. (d) Magnitude of the electric field inside the nanowire core as a function of dielectric diameter (dashed lines) and the corresponding attenuation factor δ.

Note, that Ruda *et al.* have modeled the polarization ratio of the PL emission by considering an effective emitting dipole at the center of the nanowire, while in fact luminescence occurs throughout the entire NW volume. As we integrate the electric field only over the very thin GaAs core in the NW center, our numerical results are similar to the analytically modeled data in Ref. [108]. In nanowires with thicker cores, however, the importance of taking the whole volume into account rises. It is necessary to evaluate the electric field by integrating over the entire core region, which can only be performed numerically [108]. The differences between analytical and numerical approaches become clear by the direct comparison of the electric field evaluation in the NW center on the one hand, and over the entire NW cross-section on the other hand, which is further elucidated in Appendix A.2.

8

Diameter-dependent polarization anisotropies

8.1 The dielectric mismatch effect in thin and thick quantum wires

Having the possibility to evaluate the dielectric mismatch for any desired diameter, we now come back to the analysis of the polarization behavior of the 26 nm core quantum wire with a thin dielectric diameter of $d = 45$ nm, plotted in Fig. 8.1 (a). For this wire, we determine a attenuation δ-value of 0.016 from our simulations. This means that the perpendicular light field inside the core is suppressed by almost two orders of magnitude compared with the parallel field. We take this suppression into account in our calculation of the absorption spectrum by multiplying the calculated, perpendicular spectrum with the δ-value determined in our FEM simulation. The results are plotted in Fig. 8.1 (b). The calculated spectra are rigidly shifted in energy so that the first singularity coincides with the ground state PL peak in Fig. 8.1 (a). As can be seen, there is a non-zero parallel contribution even below the energy of the first light-hole to conduction band transition at around 1.625 eV. We attribute this non-zero contribution to valence band mixing effects that were implemented in the band structure calculations, described in Sec. 5.2, and become relevant in the regime of strong quantum confinement. Apparently, although transitions with lh character seem to be negligible in this energy range when only electronic selection rules are considered (see Fig. 5.3 (b)), they become significant when perpendicular transitions, that is with hh-character, are suppressed by two orders of magnitude as a result of dielectric mismatch. As a consequence, the calculated spectrum is now governed by parallel transitions above 1.55 eV, while perpendicular polarization dominates below this energy, which is in excellent agreement with the characteristic features of our experimental PL spectrum: On the one hand, the energetic positions of the PL peaks perfectly match with the subband excitations in the calculation, on the other hand, the switching of preferred perpendicular to preferred parallel emission/absorption

at around 1.55 eV is predicted correctly.
Vice versa, the results of our simulations imply that the dielectric mismatch gradually weakens with increasing dielectric diameter. Thus, we now discuss the polarization behavior of a much thicker wire featuring a dielectric diameter of 220 nm while still maintaining the same thin GaAs core of 26 nm. The polarization-resolved PL spectra are shown in Fig. 8.1 (c) and likewise reveal three perfectly distinguishable peaks in the spectrum, but now with striking differences with respect to the polarization behavior of the 45 nm wire. The PL emission is now clearly polarized perpendicular to the wire axis over the entire experimentally covered energy range. In Fig. 8.1 (d) we show the corresponding, calculated absorption spectra corrected by a δ-value of $\delta = 0.47$, as found for the 220 nm diameter from our FEM simulations. Though the perpendicular field is still slightly suppressed, there is a high consistency with the experiments as all observed transitions are predicted to be perpendicularly polarized. Nevertheless, the parallelly polarized signal is significant in the experiment (black curve in Fig. 8.1 (c)), where especially the first two peaks at $E = 1.526$ eV and $E = 1.568$ eV can not be explained by the calculated absorption spectrum in (d), as the parallelly polarized contribution should be low below $E = 1.625$ eV. One explanation could be that polarization-resolved analyses become more complex in emission spectroscopy when waveguiding effects come into play. In sufficiently thick nanowires, charge carriers no longer emit only into free space, but also into electromagnetic waveguide modes. As a result, the light is guided along the wire before being isotropically scattered at the end facet or wire discontinuities and emitted into free space. This scattered light, decoupled from the nanowire waveguide mode, then no longer possesses its initial polarization. As we will discuss in more details in Sec. 8.4, we have strong reasons to believe that the parallelly polarized signal from our thick quantum wires, displayed in Fig. 8.1 (c), stems from initially perpendicularly, mainly y-polarized emitted light, which is scattered into z-polarization at the nanowire end facet. Note that the detection of true, y-polarized light is excluded in our measurement geometry (see Fig. 6.2 (a)). Given that perpendicular x- and y-polarized dipoles underlie the same selection rules, this scattering causes a spurious z-polarized (parallel) signal below $E = 1.625$ eV, having less intensity since it can only be collected from the end facets. As waveguiding effects only become relevant in sufficiently thick nanowires, the detection of a spurious z-polarization is more pronounced in the 220 nm wire than in the 45 nm wire.

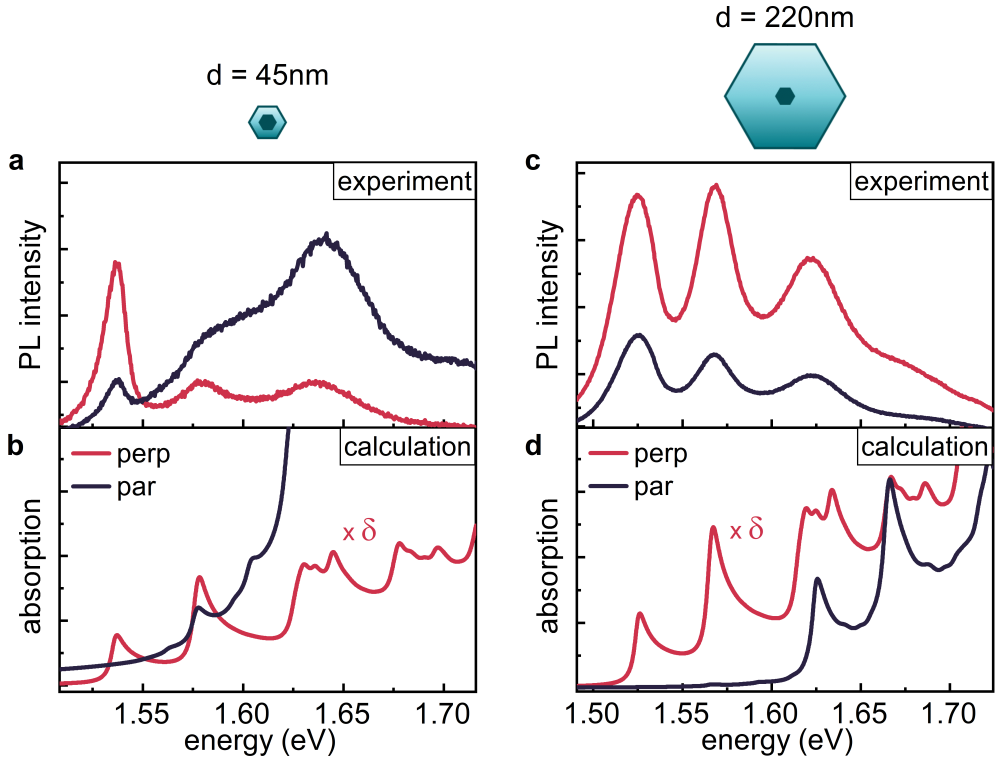

Figure 8.1: Polarization analysis of dielectrically thin and thick wires with a 26 nm core diameter. (a) Experimental PL spectra of a quantum wire with $d = 45$ nm in excellent agreement with the calculated absorption spectrum in (b) when the perpendicular spectrum is multiplied with the attenuation value δ. (c) Polarization-resolved PL of a thick, 220 nm wire showing preferred perpendicular emission over the entire energy range, also matching the behavior predicted by the calculations in (d), where the dielectric mismatch is less prominent. All y-axes are displayed in arbitrary units.

8.2 Diameter-dependent degree of linear polarization

In order to further demonstrate that the intrinsic, electronic polarization selection rules are strongly dominated by the diameter-dependent dielectric mismatch and that the light attenuation gradually decreases with dielectric diameter, we finally compare the 45 nm and the 220 nm wire with an intermediate dielectric diameter thickness of 110 nm. Therefore, we plot the energy-dependent degree of linear polarization (DLP), defined as

$$\mathrm{DLP} = \frac{(I_x - I_z)}{(I_x + I_z)}, \tag{8.1}$$

where I_x and I_z are the perpendicular and parallel spectra, respectively. Accordingly, a pure x-polarization (perpendicular) of the absorbed or emitted light yields DLP = +1 and pure z-polarization (parallel) DLP = −1. Figure 8.2 (a) shows the experimentally determined DLP traces of the PL emission for the three different diameters in the first 100 meV, starting from the energetic position of the ground state peak.
The predominant perpendicular polarized signal from the comparatively thick, 220 nm wire ($\delta = 0.047$), which we analyzed in Figs. 8.1 (c) and (d), results in a purely positive DLP with no significant variation over the experimentally covered energy range, as can be deduced from the purple curves in Figs. 8.2 (a) and (b). The deviation in absolute DLP value (0.45 in the experiment and close to 1 in the calculation) derives from the spurious, z-polarized signal, discussed in the context of Fig. 8.1 and in Sec. 8.4, whose contribution reduces the absolute value of the experimentally detected DLP. The DLP trace of the thinnest 45 nm wire ($\delta = 0.016$), on the other hand, illustrates very well the previously discussed switching from dominantly perpendicular to dominantly parallel polarization. Starting from DLP = 0.5 at 0 eV, it switches from positive to negative at around 15 meV above ground state and stays negative in the remaining energy range. Hence, the energy-dependent polarization behavior, predicted by the model in Fig. (b) for an attenuation value $\delta = 0.016$, is clearly resolved in the experimental DLP variations in (a), as well as the presence of the first two subband transitions at 0 and 42 meV. It furthermore highlights the key consequence resulting from a strong dielectric mismatch effect and considerable suppression of perpendicular light: The possibility to experimentally resolve contributions from z-polarized transitions, even if their contribution and thus their transition probability is very small. In our wurtzite GaAs wires in particular, we thus prove and directly detect the slight light-hole character in heavy-hole dominated valence subbands resulting from band mixing. The control over the visibility of such contributions, which we gain by tuning the dielectric dielectric diameter, is emphasized by the intermediate, 110 nm wire in Fig. 8.2 (a). The switching from dominant perpendicular to dominant parallel linear polarization now occurs at a higher energy compared to the 45 nm wire due to the less suppression of perpendicular light, which is in very good agreement with the simulated curve, modulated with $\delta = 0.044$ in (b). Note that the differences in absolute DLP values between experiment and calculation at 0 meV are much less in the 45 nm and the 110 nm

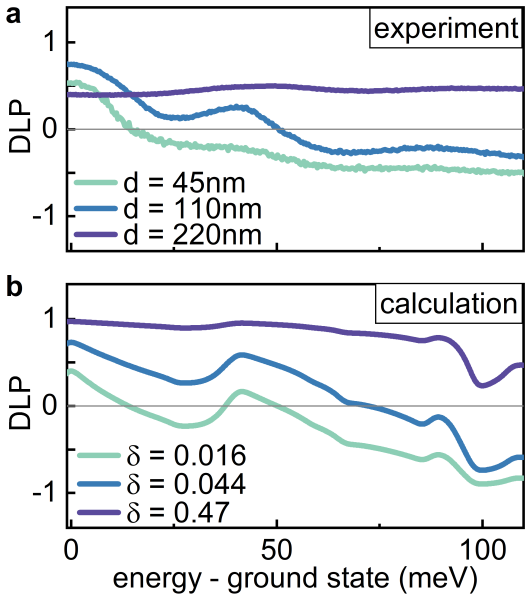

Figure 8.2: Diameter and energy dependent degree of linear polarization. (a) Experimental determined energy dependent DLP of wires with a 26 nm core and three different dielectric diameters of $d = 45$ nm, $d = 110$ nm and $d = 220$ nm. (b) Energy dependent DLP curves of the calculated absorption spectra, modulated with the δ-values found from the FEM simulations for the corresponding diameters in (a).

wire than in the 220 nm wire. This strengthens our suggestion that spurious signals due to light scattering at end facets are a result of waveguiding and thus more pronounced in sufficiently thick nanowires.
The excellent consistency in energy dependent DLP between our experimentally determined and the calculated spectra, modulated with δ, nicely highlights the subtle superposition of the electronic selection rules, resulting from the band structure symmetry, and the dielectric diameter-dependent photonic anisotropies that are strongly influenced by the dielectric mismatch effect and waveguiding properties.

8.3 Influence on carrier dynamics

As the dielectric mismatch effect causes a giant polarization anisotropy in dielectrically thin wires, it also lowers the amount of perpendicularly polarized photons that can exist inside the nanowire. As delineated in Sec. 4.1, the number of available photon modes in the emitter environment determines the rate of recombination into these modes. Hence, the emission probability is affected by the local electromagnetic density of states (LDOS). Apart from simple two-level system, energy conservation requires the consideration of the electronic jDOS when determining transition probabilities. The radiative efficiency is thus proportional to the product of the electronic jDOS and the photonic LDOS [109, 110]. For dielectrically thin quantum wires, the reduction in LDOS for perpendicularly polarized photons therefore lowers the decay rate of dipole transitions that include charge carriers with dominant hh-character. This is proven by the polarization-resolved TRPL measurements in Fig. 8.3 (a), showing the normalized decay curves of a single wire with a dielectric diameter of 55 nm (determined by SEM) and a core diameter of approximately 30 nm (determined from the subband transitions). At times after 7 ns, the decay curves

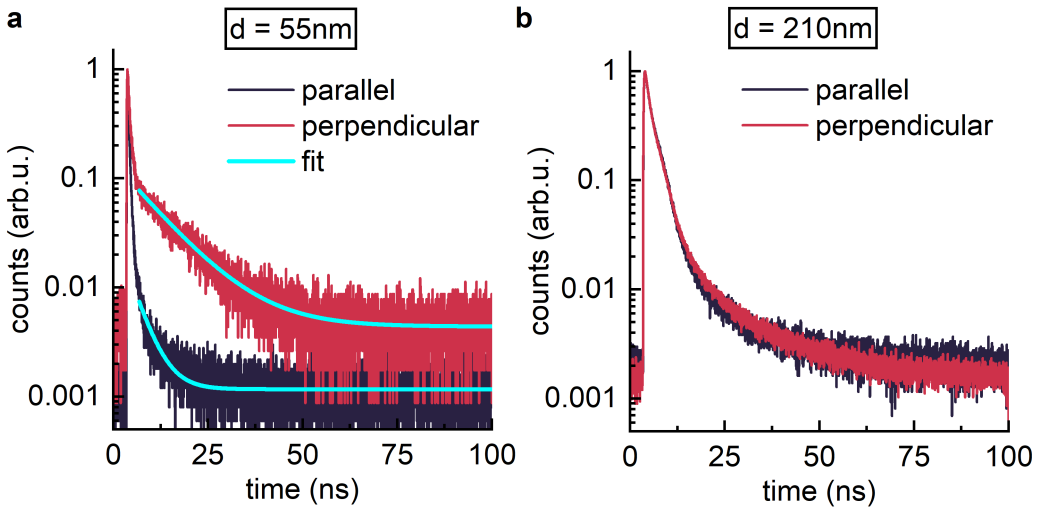

Figure 8.3: Polarization- and time-resolved measurements. (a) Decay curves of a quantum wire with a 30 nm core and a dielectric diameter of 55 nm. The longer decay time of perpendicular polarized dipole transitions directly reflects the lowered LDOS as a result of dielectric mismatch. By contrast, the polarization resolved decay curves of a quantum wire (core = 30 nm) with 210 nm dielectric diameter (b), are identical.

significantly differ from each other depending on whether the light is analyzed parallel or perpendicular to the wire axis. The slower rate of the perpendicular dipole transitions is a direct result of the lowered photonic mode density due to the dielectric mismatch effect. When we fit the curves at later times ($t > 7$ ns), where both curves exhibit a mono-exponential decay, we extract spontaneous emission lifetimes of $\tau_{\perp} = 10.8$ ns and $\tau_{\parallel} = 3.9$ ns for the perpendicularly and parallely polarized decay, respectively (cf. light blue traces in Fig. 8.3 (a)).

By contrast, the decay curves of a dielectrically thick wire show no difference between the perpendicularly and parallely polarized emission. Fig. 8.3 (b) exemplarily shows the TRPL measurements of a quantum wire with 210 nm dielectric diameter and the same core diameter of 30 nm as the wire presented in panel (a). The reason for the identical decay might be, that the detected photons stem from the same waveguide mode. As already stated in Sec. 8.1, an isotropic scattering of the emitted light at the nanowire end facets leads to a spurious, parallel z-polarization in the detection. As the detected z-polarized light originates from the same perpendicular dipole transitions, the decay curves are identical.

Our polarization- and time-resolved measurements thus clearly reflect the suppression of photonic modes inside dielectrically thin wires as a direct result of the dielectric mismatch effect. They furthermore support the results from the previous sections.

8.4 Geometrical limitations

In the previous sections, we discussed the polarization selection rules of wurtzite subbands in connection with light attenuation resulting from optical confinement. Owing to the geometry of our experimental setup, we can solely distinguish between perpendicularly x- and parallelly z-polarized emitted light in our polarization-resolved analysis (cf. Fig. 6.2 (a)). Nevertheless, there are some geometrical considerations limiting the accuracy of the detected light polarization in our confocal setup:

1. The large collection angle of the high numerical aperture (NA) microscope objective, through which the quantum wire signal is detected, influences the polarization in the image plane in an intricate way. The resulting error, however, is equal for both thin and thick dielectric wires and for all directions of polarization.

2. The polarization in thick nanowires becomes even more complex when waveguiding effects come into play, as a result of which the emitted light is guided until the end of the wire and is scattered into free space at its end facets. The scattered light from the end facets then no longer possesses its initial polarization, as it is sketched in the upper part of Fig. 8.4.

We now discuss the second mechanism in the context of the polarization analysis of the 220 nm wire, analyzed in the context of Figs. 8.1 (c) and 8.2 (a). There, we state that we detect parts of initially y-polarized PL as z-polarized light in our spectra due to light scattering at the nanowire end facets, which causes a discrepancy between the measured and calculated polarization-resolved spectra (Figs. 8.1 (c,d)) and of the value of the positive DLP (Figs. 8.2 (a,b)). As shown in Fig. 8.4 (a) in a real space micrograph of the emission profile of a 220 nm wire, the observed z-polarized emission is significant only at the end facets of the wire and at the point of geometrical tapering. Such an emission profile is typical for light coupled to guided wire modes. However, z-polarized emitted light actually cannot efficiently couple to optical waveguide modes of the nanowire, which are the fundamental $HE11_{x,y}$ modes in this diameter range [12, 18, 111, 112]. Hence, for purely z-polarized emission, a free space emission would be expected in each point of the nanowire: this would lead to an emission profile which is homogeneous over the whole nanowire, in discrepancy with Fig. 8.4 (a). At the same time, x- or y-polarized light which couples to the waveguide modes is emitted from the nanowire via scattering at the end facets of the wire or at geometrical discontinuities (such as the beginning of a tapered wire segment). This exactly matches our observation in Fig. 8.4 (a). We thus conclude that the dominant part of the z-polarized light, which we observe in the spectra for the 220 nm wire (Fig. 8.1 (c)), is in fact mainly y-polarized light from guided wire modes which has been scattered. At the contrary, x-polarized light (which we resolve in our measurement geometry) either emits into a waveguide mode (k-vector in z-direction), or radiates directly into free space towards the microscope objective (k-vector in y-direction). This leads to a more homogeneous emission profile shown in Fig. 8.4 (b).

We further illustrate our interpretation that most of the z-polarized emission in the comparatively thick wires actually results from scattered y- or x-polarized guided modes by 2D FEM simulations in a nanowire side view, shown in Figs. 8.4 (c) and (d). The GaAs nanowires are represented by the elongated rectangles with n = 3.66, a length of 2 µm and two different diameters of d = 220 nm and d = 60 nm. The refractive index of the surrounding was set to n = 1. For the excitation, we introduced a y-polarized plane wave from the left side of the nanowires, propagating in z-direction and the wavelength was set to λ = 800 nm. The color scale indicates the resulting z-component of the scattered electric field for the respective nanowire diameters. Fig. 8.4 (c) clearly shows how the wave is guided, and only emitted into free space, at the end facet of the 220 nm wire. Furthermore, the z-component of the scattered wave propagates into the direction of the microscope objective, which is deduced by the wave front intensities and indicated by the red arrow. The grey shaded areas sketch the large opening angle of the microscope objective with NA = 0.8. This is in consistency with the observed emission profile shown in Fig. 8.4 (a) and solidifies our assumption that the parallelly detected signal in Fig. 8.1 (b) arises from initially perpendicularly, y-polarized emitted light, which then uniformly lowers the absolute values of the DLP (Fig. 8.2 (a)). These scattering effect is less prominent in wires with thin dielectric diameter, as no waveguiding modes exist. All emitted light is then directly radiated into free space modes, which is illustrated in Fig. 8.4 (d) for a 60 nm wire.

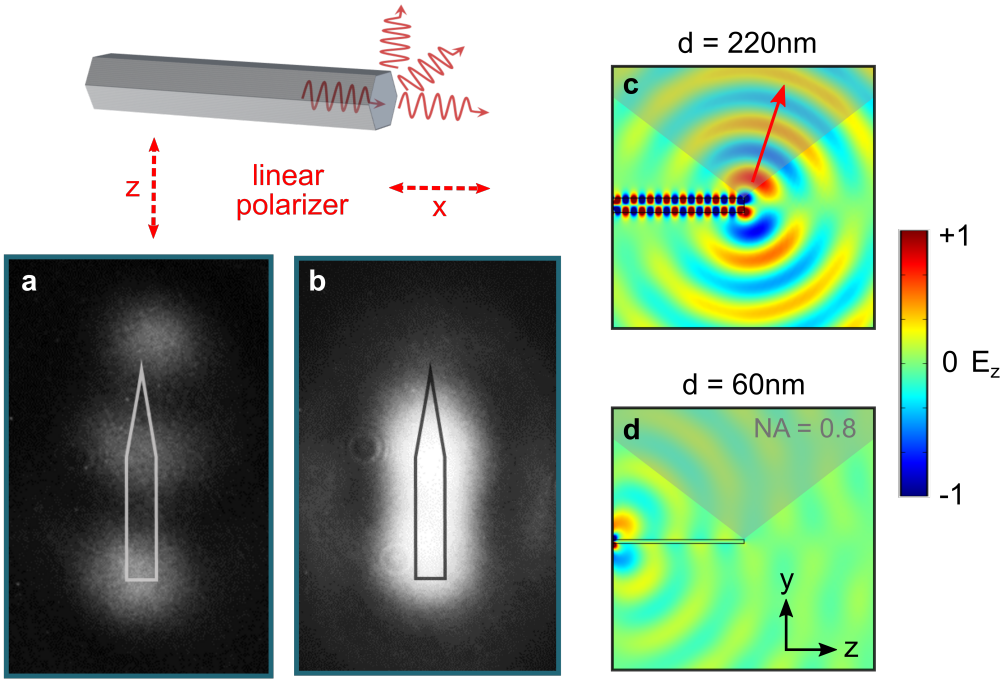

Figure 8.4: Waveguiding and light scattering in nanowires with thick dielectric diameter. (a,b) Real space micrographs of the PL emission profile when analyzed along parallel z- (a) and perpendicular x-direction (b). While the z-polarized light in (a) is only emitted at the nanowire ends or discontinuities, the x-polarized PL emission is homogeneous over the wire length. (c,d) Numerical FEM simulations illustrating the side view of the nanowire with a dielectric diameter of 220 nm (c) and 60 nm (d). The color scale indicates the scattered electric field component E_z of a y-polarized plane wave that was launched from the left side of the nanowire. The grey shaded areas sketch the large opening angle of the microscope objective with NA = 0.8.

9

Conclusion and outlook

In conclusion, our research has shown that our MBE-grown core/shell nanowires provide ultrathin GaAs cores, which ease experiments in the 1D quantum limit. Given their large confinement energies of several tens of meV, we are able to experimentally resolve up to four, well-separated subband transitions in the PL emission spectra of single quantum wires. We found an excellent agreement of the experimentally observed subband energies with **k**·**p**-based calculations. By polarization resolved PL-spectroscopy, the resolution of the subband structure further allows us to experimentally reveal the optical selection rules of WZ GaAs in the 1D quantum limit. At the same time, we demonstrate a significant role of the AlGaAs shell in polarization-resolved spectroscopy of our quantum wires: The polarization behavior is highly influenced by the dielectric mismatch effect, which induces a considerable suppression of perpendicular polarized light inside the wires with comparatively small dielectric diameter. This extrinsic, photonic polarization anisotropies significantly overlie the intrinsic, electronic 1D wurtzite selection rules. In practice, these dielectrically thin wires actively suppress perpendicularly polarized hh subband transitions and, hence, provide the opportunity to selectively excite 1D lh excitons. On the other hand, comparatively large dielectric diameters, above 200 nm, are required to observe the polarization behavior predicted the purely 1D electronic selection rules. By integrating our numerical simulations into the **k**·**p**-based calculations, we found and excellent match between the calculations and the polarization resolved emission spectra. These results will have to be integrated into spectroscopic studies and optically driven applications of such 1D wires. Furthermore, dielectrically thick quantum wires can serve as optical cavities. Together with their large confinement energies, they are promising candidates for the realization of thresholdless quantum wire lasers. Our results provide useful insights for the design of such lasers, including the optimization of the overlap between the targeted electronic subband transition and the cavity mode.

GaAs nanowire lasers

10

Fundamentals of semiconductor lasers

Lasers (*Light Amplification by Stimulated Emission of Radiation*) have meanwhile become an essential part in diverse applications of daily life, e.g. in industry, medicine, science, and more. There exist many different kinds of lasers, but all share the main components: a material which is capable of amplifying radiation (gain medium), a resonator that provides positive optical feedback and a pump source that induces population inversion.
Through their unique elongated shape and high refractive index, semiconductor nanowires naturally possess two of the three main components: the semiconductor material acts as a gain medium and the shape of the nanowire forms a stand-alone Fabry-Pérot (FP) cavity where the nanowire end facets function as reflecting mirrors (cf. Fig. 10.1). Through adding external pumping, which is done either electrically or optically, the three components to build a laser are complete.
In the following sections, we itemize important features and figures of merit that are essential for the design and characterization of nanowire lasers. Starting with the description of how optical gain is achieved in a direct-bandgap semiconductor, we continue with the basic principle of a laser resonator, followed by the waveguiding properties of nanowires. Afterwards, the lasing threshold and its connection with the mode confinement factor is defined. In the final section, a basic theoretical description of laser dynamics and how it is influenced by the spontaneous emission factor is given in the frame of static, coupled rate equations.

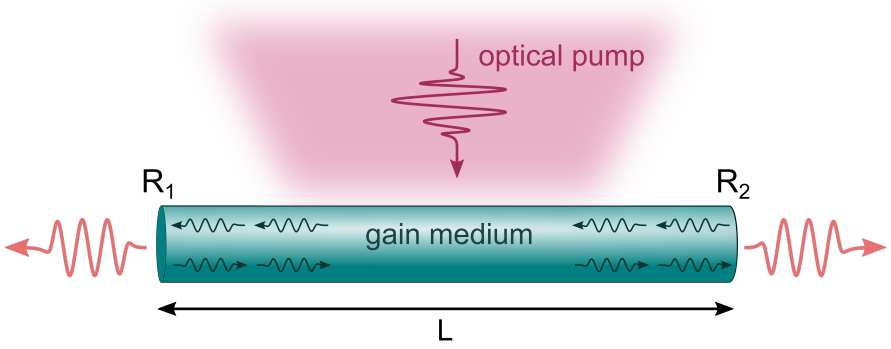

Figure 10.1: Schematic of an optically pumped nanowire laser. Three main components are needed to build a laser: a gain medium that is able to amplify radiation, an optical cavity to provide optical feedback and an external pump source to achieve population inversion. Semiconductor nanowires inherently exhibit two of those components: The semiconductor material acts as gain medium, and the elongated shape plus high refractive index build a stand-alone optical cavity of length L with the wave being reflected at the end facets of the nanowire. Modified according to Ref. [113].

10.1 Optical gain in semiconductors

In order to achieve stimulated emission, a suitable optical gain medium is needed. Direct-bandgap semiconductors, such as GaAs, are very attractive in this regard as they are smaller, cheaper, and less power consuming than other kinds of lasers [114]. In optically excited semiconductors, gain, and hence amplification, is achieved by pumping a sufficient amount of electrons from the valence to the conduction band. The high amount of carrier injection then leads to the development of quasi-Fermi levels for electrons and holes, denoted as $E_{F,e}$ and $E_{F,h}$ in Fig. 10.2 (a), respectively, whose energy separation must be larger than the bandgap of the semiconductor gain material and thus $\mu = E_{F,e} - E_{F,h} > \hbar\omega > E_g$. This is known as the Bernard-Duraffourg condition, which is satisfied above a certain carrier density and is necessary for the generation of stimulated emission [114, 115]. The process sketched in Fig. 10.2 (a) resembles the laser model of a four-level system. The carriers are injected to higher energy states, which are the quasi-Fermi levels $E_{F,e}$ and $E_{F,h}$, followed by a quick, mostly non-radiative relaxation into the ground state, meaning the band edges in Fig. 10.2 (a), where photon emission occurs with an energy $\hbar\omega$. Furthermore, the lifetime of the carriers in the ground state must be longer than the time needed for the relaxation process, which is typically the case in semiconductors like GaAs (fast phonon relaxation on the order of ps [116–120] versus radiative lifetime on the order of ns [12, 54]).
The energy-dependent optical gain in a semiconductor is usually derived perturbatively

with Fermi's Golden Rule and expressed in the form [121]

$$g(E) = \frac{\pi\hbar e^2}{\epsilon_0 m_0 n_r^2 v_g E} |M|^2 \rho_j(E) \left[f_c(E, E_{F,e}) - f_v(E, E_{F,h}) \right], \tag{10.1}$$

where e, ϵ_0, m_0, n_R and v_g are the electron charge, the vacuum permittivity, the electron mass, the material refractive index and the electronic group velocity, respectively. $|M|^2$ is the interband matrix element that governs the strength of optical transitions between the valence and conduction band and depends on various factors including the overlap between electron and hole wave function as well as the polarization of the optical field. $\rho_j(E)$ is the joint density of states (jDOS) and $f_c(E, E_{F,e})$ and $f_v(E, E_{F,h})$ are the Fermi distribution functions, giving the occupation probability for electrons and holes in the conduction and valence band, respectively. Eq. 10.1 is strongly related to optical absorption. In fact, optical gain is also expressed as negative absorption $g(E) = -\alpha(E)$. The term in the brackets $[f_c(E, E_{F,e}) - f_v(E, E_{F,h})]$ is therefore a measure of population inversion and must be positive to achieve gain. As the quasi-Fermi levels shift with increasing carrier injection, the dependency of the gain spectrum on the carrier density becomes clear by regarding Fig. 10.2 (b), where the functional shape of the gain spectrum is sketched for the case of a 3D jDOS. When the carrier density increases, positive gain is obtained for energies between μ and E_g and the peak gain simultaneously shifts to higher energies. When no population inversion exists, i.e. $[f_c(E, E_{F,e}) - f_v(E, E_{F,h})] < 0$, the material is absorbing. In this case, a negative gain curve (equals absorption) implies that photons get lost inside the material, whereas they are amplified through stimulated emission when the gain curve is positive. Photons with an energy E, for which $g(E) = 0$, are neither absorbed nor amplified, meaning that the material is transparent.

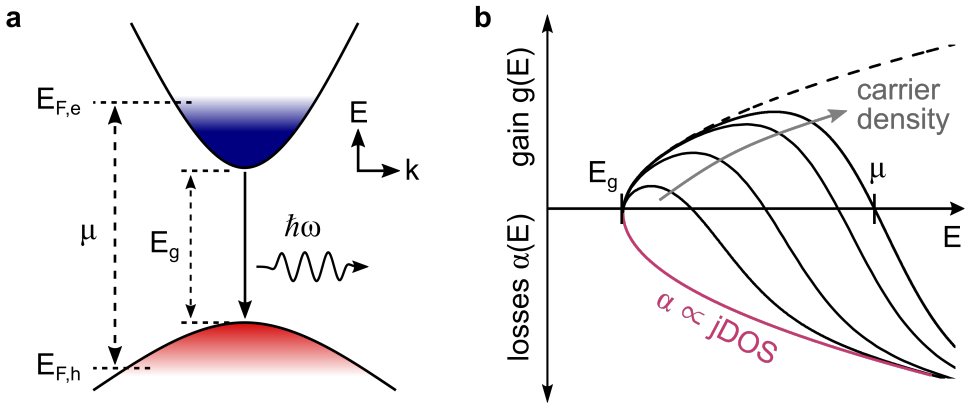

Figure 10.2: Optical gain in semiconductors. (a) Simplified schematic of the population inversion in a direct gap semiconductor. After sufficient pumping, the conduction and valence bands are filled with electrons and holes up to the quasi-Fermi levels $E_{F,e}$ and $E_{F,h}$, respectively, which are separated by the energy μ. The carrier recombination takes place near the bandgap under emission of a photon with energy $\hbar\omega$, fulfilling the Bernard-Duraffourg condition $\mu = E_{F,e} - E_{F,h} > \hbar\omega > E_g$. (b) Sketch of the gain spectrum as a function of energy. The optical gain is strongly dependent on the charge carrier density and hence on the energy μ. Without charge carriers, all incoming photons with an energy $E > E_g$ are lost by absorption (magenta curve). When the bands are filled, photons with energies between E_g and μ are amplified by stimulated emission and absorbed from the gain material for all energies above. Below E_g and at $E = \mu$, incoming photons are neither absorbed nor amplified and the material is transparent. Adapted from Ref. [113].

10.2 Laser resonator and optical gain

Conventionally, optical feedback in laser systems is provided by placing the gain medium inside an optical resonator where the wave is reflected back and forth. The light confinement between the two mirrors then leads to the formation of a standing wave when the resonator length L is a multiple of half the light wavelength λ, leading to the resonance condition $\lambda = 2L/q$, with q being an integer number [113]. Nanowires inherently represent a stand-alone Fabry-Pérot type cavity with the end facets acting as reflecting mirrors (cf. Fig. 10.1). Let us hence assume a nanowire waveguide with a fixed length L corresponding to the resonator length. The mode spacing in terms of the vacuum wavelength is then given by

$$\Delta\lambda = \frac{\lambda^2}{2Ln_g}. \tag{10.2}$$

The mode spacing for a fixed wavelength λ is therefore proportional to the inverse of the resonator length $1/L$. A laser resonator with a fixed length L therefore sustains a number of longitudinal modes, hence supporting all wavelengths λ_q with $\Delta\lambda = \lambda_q - \lambda_{q-1}$ through constructive interference. These modes are solely supported when the gain material provides positive gain, meaning that the gain is larger than all losses (cf. Sec. 10.4). The principle is outlined in Fig. 10.3 in terms of the emission wavelength. Those longitudinal Fabry-Pérot modes that overlap with the gain spectrum $g(\lambda)$ experience positive feedback and are amplified through stimulated emission. Hence, the laser spectrum is on the one hand governed by the longitudinal resonator modes, and on the other by the shape of the gain spectrum. If there is positive gain for more than one mode, the laser will contain a number of wavelengths λ_q that appear as sharp peaks in the emission spectrum, as schematically shown in Fig. 10.3.
As the light in a nanowire does not propagate as a planar wave but as a guided mode, the mode spacing has to be calculated employing the group index n_g instead of the refractive index of the bulk gain material. The group index is defined as [122–126]

$$n_g = n_{\text{eff}} - \lambda \left(\frac{\mathrm{d}n_{\text{eff}}}{\mathrm{d}\lambda} \right) \tag{10.3}$$

with n_{eff} being the effective mode index and $dn_{\text{eff}}/d\lambda$ the dispersion relation of the considered waveguide mode [127]. A more detailed explanation on the effective mode index regarding nanowire waveguides is given in the next section.

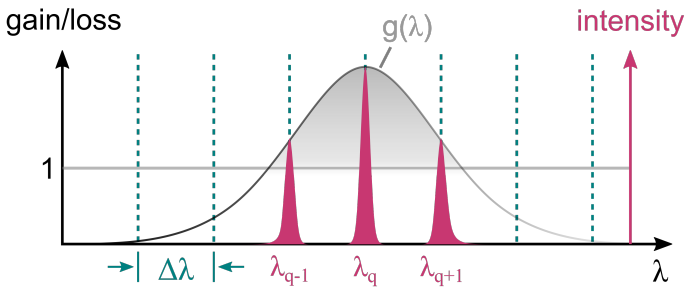

Figure 10.3: Illustration of the development of lasing modes. An optical resonator (or Fabry-Pérot cavity) supports a number of wavelengths λ_q which are separated by $\Delta\lambda$ (blue dashed lines). The modes which overlap with the positive gain spectrum (gray shaded area in $g(\lambda)$), experience positive feedback and are amplified through stimulated emission. The lasing spectrum, sketched in pink, is then governed by the resonator modes as well as the shape of the gain spectrum $g(\lambda)$. Modified according to Ref. [128].

10.3 Transversal optical waveguide modes in a nanowire on SiO_2

Similar to an optical fiber, the light in a dielectric nanowire waveguide is transversely confined inside the nanowire, based on total internal reflection on the nanowire sidewalls due to the large refractive index contrast of the wire and its surrounding. This confinement forces the electromagnetic field into a certain shape, or *eigenmode*, in which it propagates along the longitudinal, z-direction. The time-harmonic electric field is generally expressed as [129]

$$\mathbf{E}(x, y, z, t) = \tilde{\mathbf{E}}_t(x, y)e^{i(\tilde{\beta}z-\omega t)}, \tag{10.4}$$

where $\tilde{\mathbf{E}}_t(x, y)$ is the transversal field amplitude in x- and y-direction including the mode profile, $\tilde{\beta}$ the propagation constant and ω the light frequency. Note that in lossy media, the propagation constant $\tilde{\beta}$ is complex-valued and given by $\tilde{\beta} = k_0\tilde{n}_{\text{eff}}$, where $k_0 = 2\pi/\lambda_0$ is the k-vector in free space and $\tilde{n}_{\text{eff}}$ the complex-valued effective refractive index [130]. The real part of $\tilde{n}_{\text{eff}}$ is the effective mode index $n_{\text{eff}} = k_z/k_0$, with k_z being the mode propagation constant (real part of $\tilde{\beta}$) in axial direction [131]. n_{eff} therefore gives a measure on how much of the light is guided inside the waveguide.
Whether light with a given frequency can travel through a waveguide is strongly dependent on the waveguide diameter. To get an impression on how a wave propagates inside a nanowire, we analytically calculate the eigenmodes using the mode analysis solver implemented in COMSOL multiphysics v.4.2a. Using the finite-element method (FEM), the electromagnetic wave equation is solved as an eigenvalue problem for the given structure and a known propagation direction in out-of-plane (z-)direction, leading to a solution in the form of Eq. 10.4. The total, two-dimensional simulation area consists

of a $4 \times 4\,\mu m^2$ square with two concentric hexagons in the center The inner hexagon represents the GaAs core with a variable diameter, and the outer one the AlGaAs shell with a fixed shell thickness of 15 nm. The nanowire is lying with one side-facet on a SiO_2 substrate and is otherwise surrounded by vacuum. The material parameters are defined by their refractive indices at the simulation wavelength $\tilde{n}(\lambda) = n - i\kappa$, whereby $\lambda = 820\,nm$ was set to be close to the emission wavelength of GaAs. For the non-absorbing materials, we took $\tilde{n}_{vac} = 1$, $\tilde{n}_{SiO_2} = 1.45$ [104, 105] and $\tilde{n}_{Al_{0.32}Ga_{0.68}As} = 3.4$ [106], and for the absorbing GaAs $\tilde{n}_{GaAs} = 3.67 - 0.059i$ [106].

The solutions of the resulting effective mode indices as a function of nanowire diameter are plotted in Fig. 10.4 (a). The guided modes take values of n_{eff} between the index of the substrate and the nanowire and are identified by the shape of their mode profile and the polarization of the electric and magnetic field. We use the naming convention for guided modes in a cylindrical dielectric waveguide [131]. The first two letters refer to the mode type: hybrid (HE or EH), transversal electric (TE), or transversal magnetic (TM). The number suffixes such as "11" are to describe the radial order and angular symmetry, respectively, and the subscripts "x" and "y" indicate the different polarization states of two nearly degenerate modes. Near the mode cut-off diameter, where n_{eff} is close to n_{SiO_2}, the modes are weakly confined within the nanowire and the degeneracy between the $HE11_y$ and the $HE11_x$ as well as between the $HE21_y$ and the $HE21_x$ mode is lifted as the SiO_2 substrate acts differently on electric fields with polarization parallel or perpendicular to the substrate surface. An increasing diameter on the other hand leads to a better confinement of the guided mode within the nanowire when n_{eff} approaches n_{GaAs}, which reduces the influence of the substrate and degenerates the different polarization states. A larger diameter also supports a higher number of eigenmodes, while no guided modes at all exist in wires with $d < 160\,nm$. The mode with the highest value of n_{eff} at a given diameter is commonly defined as the *fundamental* mode. Note that all effective index values below the mode cut-off (where $n_{eff} \leq n_{SiO_2}$) are not relevant as the simulation delivers unphysical results there.

The spatial intensity distribution of the various modes is shown separately in Fig. 10.4 (b). In a nanowire with $d = 200\,nm$ (left panel) only the fundamental $HE11_{x,y}$ modes exist whose intensity is partially pushed out of the nanowire due to a weak confinement. The right panel shows the first six waveguide modes that are supported in a nanowire with comparatively thick diameter of $d = 400\,nm$. Here, compared to the 200 nm wire, the modes with largest mode indices, such as the two fundamental $HE11_{x,y}$ modes and the TE01 mode, are very well confined within the nanowire as they are far away from their cut-off diameter. The modes with lower effective indices, like the $HE21_{x,y}$ and TM01 modes, however, still feature evanescent fields outside of the nanowire.

Understanding the mechanisms of a propagating wave in a nanowire waveguide is crucial for the design of nanolasers and will be an essential part of the interpretation of our experimental results in the subsequent chapters.

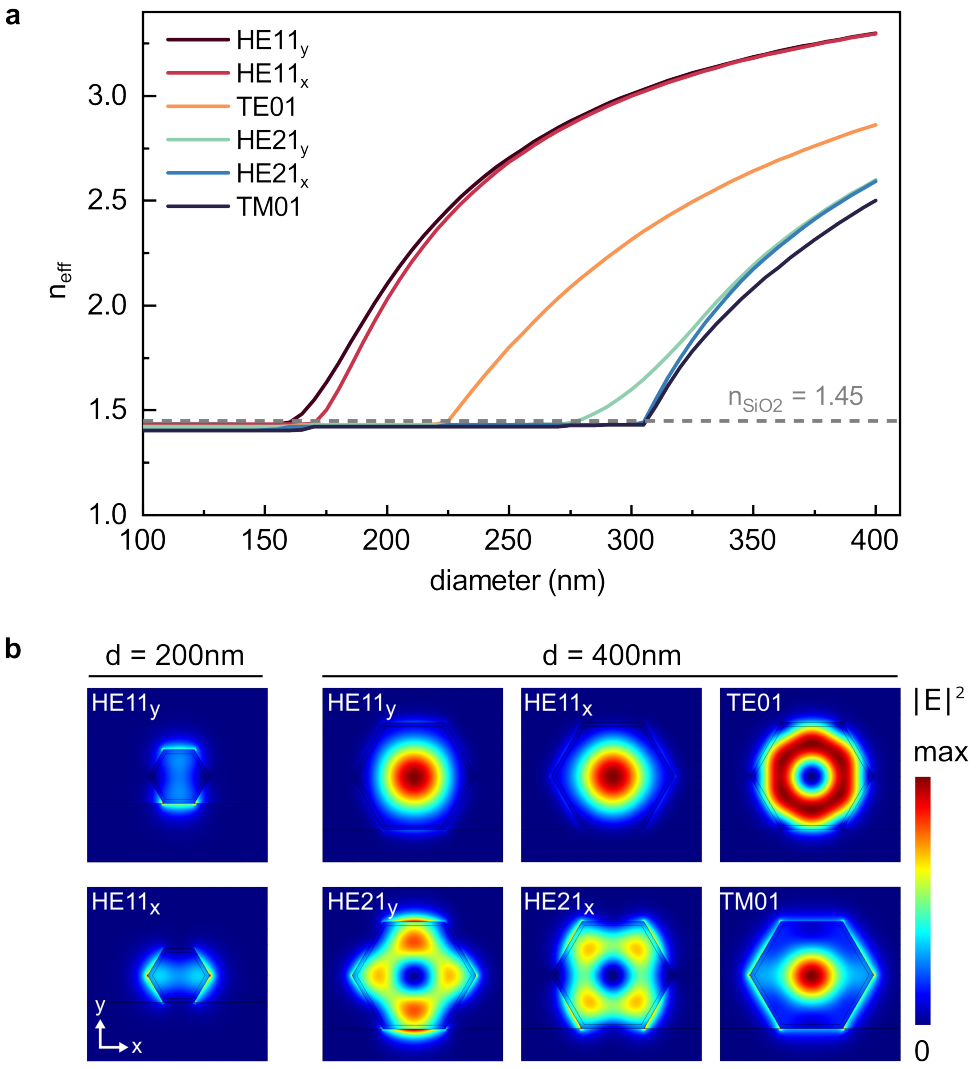

Figure 10.4: Waveguide modes at $\lambda = 820\,\text{nm}$ in a nanowire lying on a SiO_2 substrate. (a) Effective mode index as a function of nanowire diameter showing the emergence of different mode branches at a certain diameter, also referred to as mode cut-off diameter. The effective indices adopt values between the index of the SiO_2 substrate ($n = 1.45$) and GaAs ($n = 3.67$). Close to the mode cut-off diameter, the degeneracy between the $HE11_y$ and the $HE11_x$ as well as between the $HE21_y$ and the $HE21_x$ mode is lifted as the SiO_2 substrate has different influence on electric fields with polarization parallel or perpendicular to the substrate surface. (b) Intensity distribution of the different modes. For a nanowire with $d = 200\,\text{nm}$ (left panel) only the fundamental $HE11_{x,y}$ modes exist whose intensity is partially pushed out of the nanowire. The right panel shows the first six waveguide modes that exist in a nanowire with a comparatively thick diameter of $d = 400\,\text{nm}$. Note that the color scale is not the same for the different modes.

10.4 Lasing threshold and confinement factor

Light amplification and lasing inside a Fabry-Pérot cavity is reached when the round-trip gain exceeds the round trip losses, or, in other words, the light beam must gain more photons than it loses after traveling the path $2L$, with L being the cavity length. Hence, the net gain per round trip must be higher than the sum of all losses [121, 132]. The threshold condition is fulfilled when gain and losses are exactly balanced and is defined as [9, 122, 133, 134]

$$\Gamma g_{\mathrm{th}} = \alpha_p + \alpha_m, \tag{10.5}$$

where Γ is the confinement factor, g_{th} the threshold gain, α_{p} the modal propagation losses and α_m the mirror losses given by $\alpha_m = \frac{1}{2L}\ln\left(\frac{1}{R_1 R_2}\right)$ with R_1 and R_2 being the effective reflection coefficients on each end facet.

The confinement factor Γ is a dimensionless parameter which describes the mode overlap with the active region, or gain medium respectively. It is traditionally defined as the ratio of the optical power inside the active region to the total optical power [122]. Intuitively, Γ is then always less or equal than unity, where $\Gamma = 1$ implies a maximum overlap of the light field with the gain medium. However, this is solely true for conventional lasers with weak confinement and does not hold for nanowire waveguides with strong optical confinement.

An illustrative picture is given by Maslov *et al.* [135]: Considering a simple planar waveguide, a guided wave can be represented as a plane wave that propagates through the waveguide at a certain angle with respect to the longitudinal z-axis and is frequently reflected at the boundaries due to the large refractive index contrast (total internal reflection). Hence, the distance traveled by the guided (plane) wave is larger than that of a simple plane wave traveling through the bulk material. If a significant part of this wave is localized inside the gain material, the net gain per unit length in z-direction can be larger than in the bulk counterpart and thus exceed unity.

By assuming an isotropic gain along the axial direction, a more accurate definition for the confinement factor is [9, 18, 122, 130, 131, 136–138]

$$\Gamma = \frac{c\epsilon_0 n_b \iint_{\mathrm{active}} \frac{1}{2}|\mathbf{E}|^2 \, dA}{\iint_{\mathrm{tot}} \frac{1}{2}\mathrm{Re}\left[\mathbf{E}\times\mathbf{H}^*\right]\hat{\mathbf{e}}_z \, dA}, \tag{10.6}$$

where $\mathbf{E}$ and $\mathbf{H}$ are the complex electric and magnetic fields of the propagating wave, c the speed of light, ϵ_0 the vacuum permittivity and n_b the refractive index of the bulk gain material (at the free space wavelength λ), which is $n_{\mathrm{GaAs}} = 3.67$ in our case. The integral in the numerator is over the active region only, i.e. the GaAs core cross-section area, while the expression in the denominator is integrated over the entire cross-sectional waveguide structure. The stimulated emission, and hence the gain, is related to the intensity of the light field, which is proportional to $|\mathbf{E}|^2$. As the integrand in the denominator is the z-component of the Poynting vector (and therefore a measure of power), the confinement factor in Eq. 10.6 can be thought of the amount of intensity overlapping the gain medium

per unit input power [130].
Using the numerical COMSOL simulations introduced in Sec. 10.3, we calculate the confinement factor Γ according to Eq. 10.6 for each mode and each nanowire diameter. The results are plotted in Fig. 10.5 (a) (solid lines). Note that we do not show results below the mode cut-off as the simulation yields unphysical values in this range. For all waveguide modes, the confinement factor is low close to the mode cut-off and rises as the diameter increases. It is seen that it even exceeds unity above a certain diameter. This may seem counter-intuitive, but is a direct result of strong optical waveguiding, as explained above. It occurs that the gain for higher order modes, and hence the confinement factor, is even larger, which is noticeable for the $HE21_{x,y}$ modes in Fig. 10.5 (a), where the $HE21_x$ mode reaches a maximum of $\Gamma = 1.6$ at $d = 320\,\text{nm}$. As a result of strong confinement, the guided modes have a slow group velocity v_g (and hence a high group index n_g), and will gain more energy by traveling along the waveguide compared to the plane wave counterpart. Larger confinement factors $\Gamma > 1$ can thus be also understood in terms of large group indices with $n_g > n_b$.
According to Eq. 10.5, a large confinement factor allows to reduce the threshold gain, which is a general aim in the design of nanolasers in order to establish low power consuming devices. Another consideration that arises in this context is the minimization of all possible losses. The mirror losses α_m, based on imperfectly reflecting end facets, will not be further specified within the framework of this thesis, as the determination of realistic values for R is not straightforward due to the differently shaped end facets from wire to wire. Numerical approaches to determine the reflectivity of different modes on a flat nanowire end facet can be found for example in Refs. [111, 139, 140]. Here, we will focus on the modal propagation losses α_p which result from the absorbing properties of the GaAs core. They are defined as the imaginary part of the effective propagation constant $\tilde{\beta}$ and are therefore expressed as [18, 141]

$$\alpha_p = 2k_0 \text{Im}(\tilde{n}_{\text{eff}}), \tag{10.7}$$

with $k_0 = 2\pi/\lambda_0$ being the free space wave vector. The calculated values of α_p for the different modes are plotted in the same graph as the confinement factor in Fig. 10.5 (a) as dashed lines. Intriguingly, the mode propagation losses show the same trend with respect to the wire diameter as the confinement factor Γ. When we now reformulate the relation in Eq. 10.5, we see that the lasing threshold is directly proportional to $g_{\text{th}} \propto \alpha_p/\Gamma$, which will give us a useful figure of merit in connection with the modal contribution to the lasing threshold. In the case of a nanowire lying on SiO_2, the results of the threshold proportionality factor α_p/Γ are shown in Fig.10.5 (b). For each mode, the threshold features a sharp increase for small diameters close to the mode cut-off, which is expected given the small confinement factors in this range. This is similar to what was experimentally observed in Ref. [127] for photonic lasing modes in CdS nanowires. With increasing diameter however, the losses and the confinement are balanced and reach a minimum value of $\alpha_p/\Gamma \approx 4.5 \times 10^3\,\text{cm}^{-1}$ in our simulation.

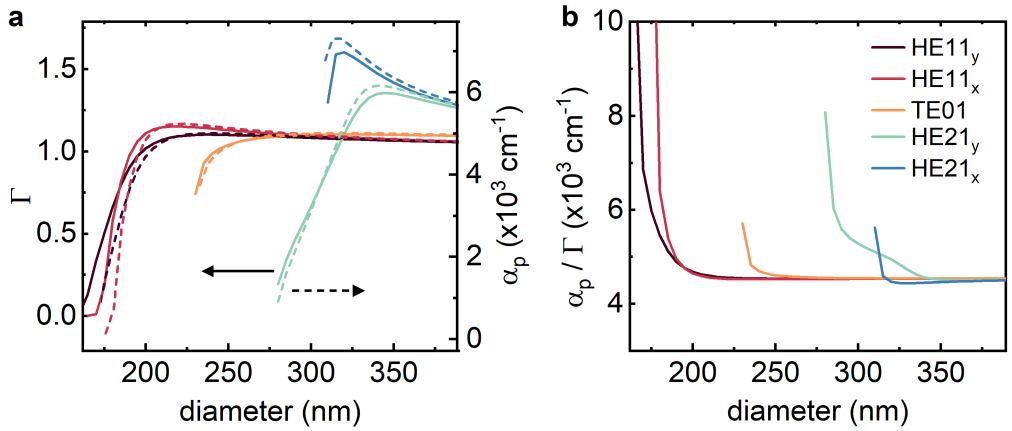

Figure 10.5: Mode confinement and propagation losses of nanowires on SiO_2. (a) Mode confinement factor Γ as a function of nanowire diameter for the first five waveguide modes (solid lines). Due to the strong optical confinement in a waveguide, the confinement factor can exceed unity as compared to conventional, weakly confined laser systems. (b) Diameter dependence of the lasing threshold proportionality constant α_p/Γ. Due to a weak confinement, the threshold rapidly rises for each mode when the diameter approaches the mode cut-off. With increasing diameter, the losses and confinement are balanced and reach a minimum value of $\alpha_p/\Gamma \approx 4.5 \times 10^3\,\mathrm{cm}^{-1}$.

10.5 Laser rate equations

Semiconductor nanolasers are often characterized by their input-output characteristics, which are modeled using coupled rate equations that relate the number of cavity photons to the charge carrier density. Fitting experimental data with rate equations provides estimates of key parameters such as the spontaneous emission factor β, which represents the proportion of emission that couples into a specific laser mode [142]. This factor is extremely important in the threshold behavior of a laser and frequently used as a benchmark for the laser quality within the nanolaser community. We therefore want to illustrate how this factor influences the measured quantities, such as the power-dependent emission intensity, by providing a simplified theoretical concept for these laser dynamics. The exact form of the rate equation depends on the gain material, the cavity design and the pumping method [143]. We will use the expressions for the two coupled rate equations proposed by Ma *et al.* [144] based on the light output properties of a microcavity laser defined in Ref. [145]:

$$\frac{dn}{dt} = p - An - \beta\Gamma As(n - n_0), \tag{10.8}$$

$$\frac{ds}{dt} = \beta An + \beta\Gamma As(n - n_0) - \gamma s, \tag{10.9}$$

where p is the pump power, Γ is the mode confinement factor, A the spontaneous emission rate, γ the sum of propagation and cavity losses and n_0 defines the carrier density where the gain medium is transparent. The first equation describes the rate of change of the electron-hole-pair density n with the first term accounting for the pumping rate and the second and third term for the carrier loss through spontaneous and stimulated emission, respectively. $(n - n_0)$ thus denotes a measure of population inversion. The second equation models the rate of change of the number of cavity photons s with the first and second term accounting for photons generated by spontaneous and stimulated emission, respectively, and the final term for photons that get lost from the cavity.
To obtain an idea of how the spontaneous emission factor β influences the lasing behavior of a nanolaser, we solve the rate equation assuming steady-state conditions, hence $dn/dt = ds/dt = 0$. Additionally, we assume an ideal four-level system with rapid ground level depletion and set $n_0 = 0$. Equations 10.8 and 10.9 can then be reformulated as

$$s^2 + \left(\frac{1}{\beta\Gamma} - \frac{p}{\gamma}\right)s - \frac{p}{\Gamma\gamma} = 0, \tag{10.10}$$

resulting in the following expression for the power-dependent photon density inside the cavity [146]:

$$s(p) = -\frac{1}{2}\left(\frac{1}{\beta\Gamma} - \frac{p}{\gamma}\right) + \frac{1}{2}\sqrt{\left(\frac{1}{\beta\Gamma} - \frac{p}{\gamma}\right)^2 + 4\frac{p}{\Gamma\gamma}}, \tag{10.11}$$

and the carrier density:

$$n(p) = \frac{p}{A\,(1 + \beta\Gamma s)}. \tag{10.12}$$

We plotted the functions $s(p)$ and $n(p)$ with different β-factors in Figs. 10.6 (a) and (b), respectively. Note that all other factors were set to unity, as they may shift the curves on the x-axis or change the slope, but they do not influence the overall curve shape. The axes are therefore both presented in arbitrary units. For the open cavity case ($\beta \ll 1$), the output characteristic closely resembles that of conventional lasers, as shown by the light brown curve in the inset of Fig. 10.6 (a), where $\beta = 0.001$: At low pump powers p, the laser is in the spontaneous emission (SE) regime and the majority of spontaneously emitted photons are lost from the cavity. Hence, the number of photons inside the cavity s remains very low. Around threshold (here at $p \approx 1$), where the gain exceeds the cavity losses, stimulated emission sets in and the photon number rises very rapidly, which is referred to as amplified spontaneous emission (ASE). Note that in the linear representation (inset in (a)), the curves were normalized to $p' = \beta^{-1}p$, and correspondingly $s' = \beta s$, in order to bring all curves to the same scale for comparison purposes. This super-linear increase becomes more clear by the double-logarithmic plot in of Fig. 10.6 (a) (light brown curve), showing the typical "S"-shape of a laser input-output characteristic, where the photon density s abruptly increases by several orders of magnitude, when the pump reaches the threshold (here at $p \approx 1000$) [147]. Above threshold, all photons emit into a single laser mode, the gain is saturated and the photon density rises linearly with the pump power again. At the same time, the charge carrier density n (light brown curve in Fig. 10.6 (b)) increases linearly in the spontaneous emission regime and saturates after the threshold is reached, as the concomitant enhancement of recombination rate inhibits the carrier density to further increase.
To summarize, in the open cavity case where $\beta \ll 1$, a lasing threshold is easy to determine from the input-output curve by the kink in the linear plot or the super-linear section in the double-logarithmic representation and also by the saturation of carrier density.
However, for increasing β, these clear markers of the lasing threshold vanish and the photon number gradually changes from the SE-dominant regime to the stimulated emission-dominant one without a distinct transition [145]. As a result, the kink in the linear representation smooths out and the super-linear transition vanishes more and more with increasing β until it totally flattens in the extreme case of a closed microcavity ($\beta = 1$). Here, every emitted photon couples to a resonant laser mode, suggesting a "thresholdless" behavior according to the photon density s. However, as constituted by Ma *et al.* [144], the term "thresholdless" should be rather understood as "lack of a threshold behavior" than as an instant onset of laser action at infinitely small pump intensities. There is still a transition visible in the pumping dependence of the charge carrier density, which points to a finite threshold required to clamp the upper-state population n, even in the case of $\beta = 1$. Nevertheless, the quantitative determination of a precise lasing threshold is challenging when the spontaneous emission factor approaches unity. The shift of the super-linear regime in Fig. 10.6 (a) and the kink in Fig. 10.6 (b) to lower pump

intensities, however, clearly indicate a reduction of lasing threshold with increasing β. A high β-factor is therefore desirable to enhance the optical efficiency of laser structures. This can be achieved by shrinking the modal volume of the resonator which enhances the light-material interaction strength [145, 148] and also the number of modes competing for gain. The small resonator size of nanowire lasers is therefore a beneficial feature. Recent approaches even exploit the coupling of optical modes to surface plasmon polaritons (SPPs) of a metal to reduce the mode volume to a size below the diffraction limit of light. This will be an essential part of Chs. 12 and 13.

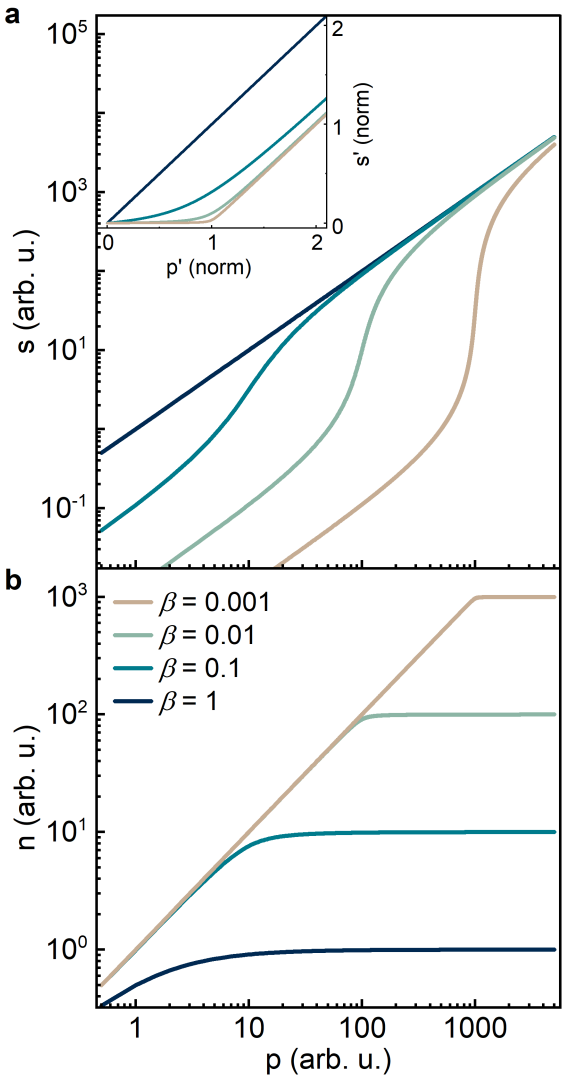

Figure 10.6: Influence of the spontaneous emission factor β on the laser characteristic of a microcavity laser. (a) Photon density s as a function of pump intensity for β-factors ranging from $\beta = 0.001 - 1$. Small β laser systems reveal the characteristic "S"-shape with a distinct super-linear increase at the threshold pump p (ASE regime), marking the transition from spontaneous emission (below threshold) to lasing (above threshold). With increasing β the curve flattens, making the threshold less obvious until it totally vanishes in the extreme case of $\beta = 1$. Inset: Linear representation of the same curves but normalized to obtain the same scale. The kink in the curve for $\beta = 0.001$ at $p' = 1$ clearly marks the lasing threshold, while it smooths out with increasing β until it becomes completely linear for $\beta = 1$. (b) Upper state carrier density n as a function of pump intensity. The population is clamped above threshold due to an enhanced spontaneous emission rate, suggesting a finite threshold even for $\beta = 1$.

11 Evidence of Fabry-Pérot cavity in nanowires on SiO_2

11.1 Fabry-Pérot resonances in PL emission

In order to investigate their lasing properties in a lying position, all nanowires were transferred from the growth substrate onto another substrate. In this chapter, nanowires lying on a dielectric substrate, namely SiO_2, are presented. All NWs investigated in the present and subsequent chapters with respect to their lasing behavior have comparatively thick GaAs core diameters of around 200 nm, a thin $Al_{0.36}Ga_{0.64}As$ shell of nominally 15 nm and are capped with approximately 5 nm of GaAs. All diameter information in the following refers to the total core/shell/cap diameter.
We investigate the individual wires by µ-PL spectroscopy, using a non-resonant, pulsed excitation of 690 nm wavelength at repetition frequencies ranging from $1 - 80$ MHz. The laser beam is focused onto the sample through a 20× objective with NA = 0.45, resulting in a laser spot size of $4 - 5$ µm which illuminates the entire nanowire. A redirection of the luminescence signal, collected by the same objective, enables us to locate isolated nanowires on the substrate as well as directly image their luminescence profile in real space. The real space image of a typical nanowire is shown in Fig. 11.1 (a). While the body of the nanowire is only faintly luminescent, two bright spots are observed at the nanowire ends. This behavior suggests that the PL, emitted from the nanowire, is guided along the wire axis and only couples out at the end facets due to scattering. The scattered light furthermore resembles two point sources according to the emergence of Airy disks around them. The corresponding scanning electron micrograph of this wire is shown in Fig. 11.1 (b). The nanowire has a total diameter of 200 nm, the stem a length of $L = 4.63$ µm and the total length, including the tip, is $L = 5.28$ µm. The power-dependent PL spectra of this wire are shown in Fig. 11.1 (c). The low-excitation spectra (light-brown curves) exhibit a single, broad PL peak centered at 823 nm. By gradually increasing the excitation power, the broad spontaneous emission spectrum is superimposed by periodically occurring peaks, equidistantly distributed over the gain

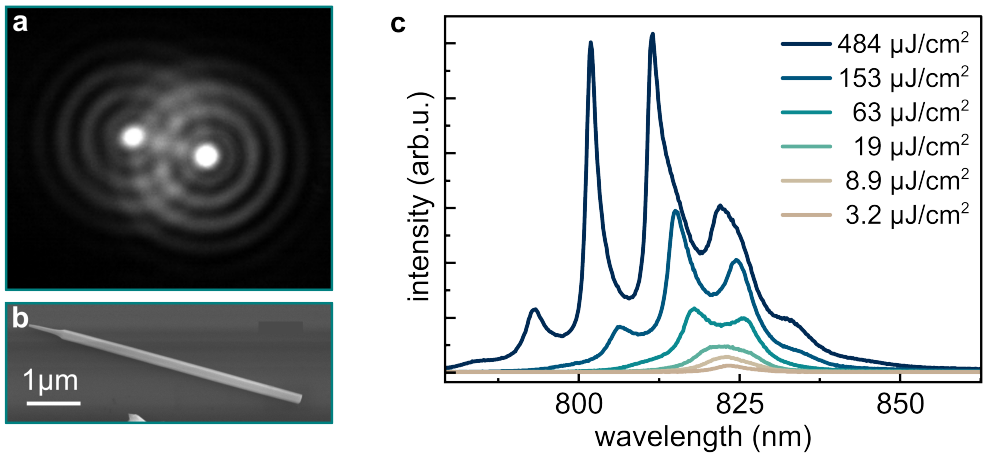

Figure 11.1: Evidences of Fabry-Pérot resonances in nanowires lying on a SiO2-substrate. (a) Characteristic luminescence profile of a nanowire. The poor intensity at the nanowire body combined with the strong out-coupling at the end facets are indicative of waveguiding behavior. (b) Corresponding SEM of the wire shown in (a) (not to scale). (c) Power-dependent PL spectra of the same wire. At low excitation density, the wire exhibits a single, broad spontaneous emission peak. With gradually increasing excitation power, a transition from spontaneous to amplified spontaneous emission is demonstrated by the equidistantly emerging peaks, insinuating that optical gain inside the nanowire Fabry-Pérot cavity is achieved.

spectrum. Together with the strong signs of waveguiding implicated by the emission profile in Fig. 11.1 (a), this behavior clearly indicates the occurrence of optical gain inside the nanowire cavity, with those wavelengths being amplified that correspond to the longitudinal Fabry-Pérot modes of the resonator. Hence, we observe a transition from the spontaneous emission (SE) regime to the amplified spontaneous emission (ASE) regime in Fig. 11.1 (c) at an excitation density of 63 $\mu J/cm^2$, where the first Fabry-Pérot (FP) modes begin to evolve. They develop into narrow peaks up to the highest excitation density of 484 $\mu J/cm^2$. Nevertheless, the spectrum at highest excitation still exhibits an intense spontaneous emission background, which implies that the lasing regime is not yet reached. Note that the GaAs core in the presented wires is too thick to feature any contribution of quantum confinement effects to the spectra. Recombination from excited higher subbands, as it was the case in part II of this thesis, can therefore be excluded.
As further verification that the spectra in Fig. 11.1 (c) are governed by optical gain inside the nanowire cavity, we examine the dependence of the mode spacing on the nanowire length, as shown in Fig. 11.2 (a). We plot the mode spacing of four different nanowires with statistical length distribution as a function of the reciprocal of the nanowire length L. The diameters of the presented wires range from $d = 200 - 210\,\text{nm}$. Unfortunately, on this sample, the yield of nanowires showing FP modes was quite low, which hinders

us from producing a larger statistic. Nevertheless, the linear relationship of $\Delta\lambda \propto 1/L$ according to Eq. 10.2 is still recognized in Fig. 11.2 (a) (black spheres). For this plot, we took the length of the nanowire stem without the tapered tip. At the tapered nanowire end, the detailed position of wave reflection can hardly be determined and we therefore chose a length error of ±100 nm. The wavelength error of ±0.2 nm results from the finite resolution of the spectrometer. At this point, another reason for the not-perfectly linear relationship should be emphasized: MBE grown nanowires not only statistically differ in length, but also slightly in diameter, which changes the group index of the guided light and hence also the mode spacing. Especially in the diameter range around 200 nm, we are close to the mode cut-off where the effective index and consequently also the group index change significantly with small diameter variations. As a result, the mode spacing also varies with changes in diameter. From the linear regression (dashed line in Fig. 11.2 (a)), we estimate an average group index of $n_g = 5.2$, according to Eq. 10.2, which is much higher than the refractive index of bulk GaAs ($n_{\mathrm{GaAs}} = 3.67$), pointing towards a high optical confinement.
Another intriguing effect in this diameter range is the slight non-degeneracy of the $\mathrm{HE11_x}$ and $\mathrm{HE11_y}$ mode (cf. Sec. 10.3), which consequently have a different effective index at the same diameter. As outlined above, a change in effective index affects the mode spacing which makes the two modes spectrally distinguishable, as shown in the spectrum in Fig. 11.2 (b). At each longitudinal mode position, there is a clear double-peak, with each of them corresponding to a different transversal mode (labeled with "1" and "2"), most probably to the $\mathrm{HE11_x}$ and $\mathrm{HE11_y}$, as no other modes exist in this diameter range. We observe this in two of the presented wires and the corresponding mode spacing of the second mode is plotted in (a) (turquoise spheres). The data that correspond to the same wire are encircled. Obviously, the spacing is different for the two peaks, which confirms our suggestion that two different transversal modes are amplified inside the nanowire cavity.
To conclude, we have a clear evidence that our nanowires form a Fabry-Pérot like cavity and that we are able to achieve optical gain. Nevertheless, with the available optical pumping power, no lasing was observed from those nanowires as there is still a strong SE background in the spectrum. In addition, the yield of wires where we achieved light amplification in the ASE regime was sparse, which indicates that the quality of the cavity is poor. This may be due to the tapered end facet which does not act as a satisfactory mirror and thus induces huge mirror losses that push the threshold to high pump intensities. The deterioration of reflectivity caused by tapering will be discussed next.

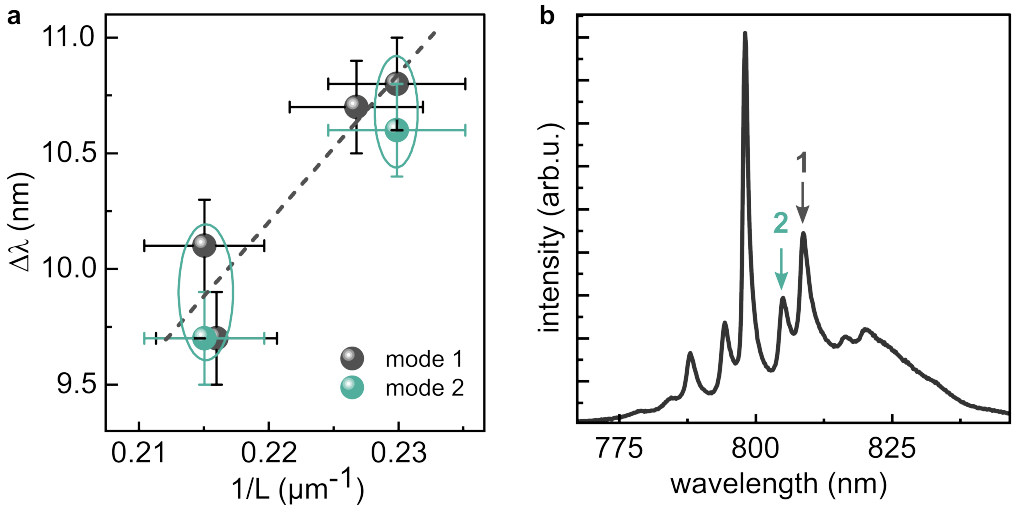

Figure 11.2: Mode spacing in nanowire cavities. (a) Longitudinal mode spacing versus inverse cavity length. The linear relationship confirms the Fabry-Pérot like behavior of the nanowire cavity. The data points belonging to the same wire are encircled. (b) High-excitation spectrum of a nanowire cavity in which two transversal modes are amplified. The resonances of the individual modes are labeled by "1" and "2".

11.2 Tapering induced cavity losses

For various applications, the strong end facet tapering is exploited to enhance the extraction efficiency of a NW waveguide due to the increased and directional transmission on the facet [149, 150]. For lasing purposes however, this property is counterproductive as it vastly diminishes positive optical feedback. We now give a qualitative picture of how the conical tapering of the nanowire end facet impairs the reflectivity and thus the quality of the cavity. Quantitatively, calculations considering a three-dimensional structure are required by taking into account the *modal* reflectivity as a function of nanowire taper, which is beyond the scope of this work. We can still illustrate the reduction of the reflectivity. The simulations in Fig. 11.3 present our qualitative picture.
The procedure is the same as the one described in Sec. 8.4, but now we adapted an isosceles triangle at the right edge of the wire that represents the tip. The tip length is defined as the distance from the triangle base to the tip. Figs. (a) - (c) show the scattered electric field intensity for tip lengths of 0.02 µm, 1.0 µm and 2.0 µm, respectively. When the end facet is nearly flat in (a), a large part of the wave is reflected back, which leads to a standing wave pattern inside the wire. With increasing tip length, the reflection is significantly reduced and most of the light transmits through the tip, which is highlighted by the vanishing interference pattern, most strongly demonstrated in (c) for the longest tip. To further quantify this, we plotted the reflectance as a function of tip length in Fig. 11.3 (d), which is defined as the ratio of the power that is reflected back to the entry

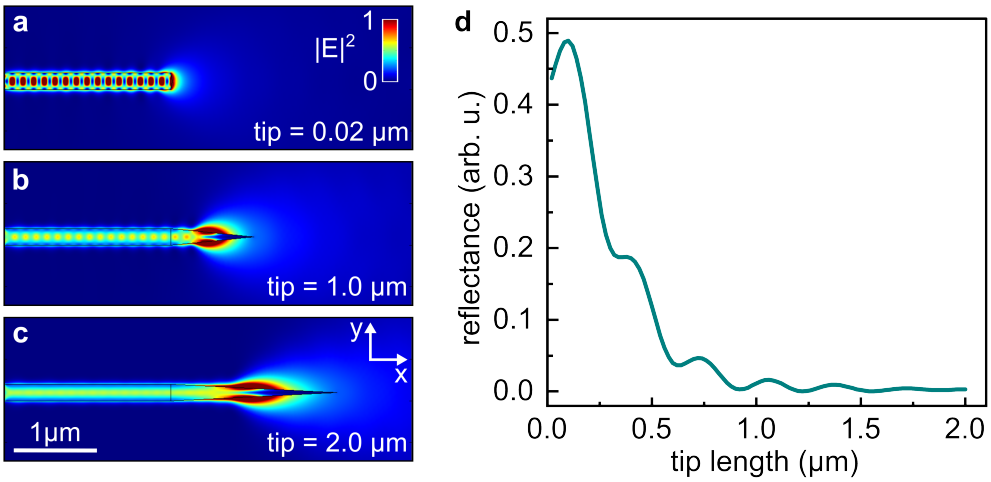

Figure 11.3: Influence of the tip length on the end facet reflectivity. (a) - (c) Scattered electric field intensity for tip lengths of 0.02 µm, 1.0 µm and 2.0 µm, respectively. The vanishing standing-wave pattern inside the nanowire indicates a reduction of reflectivity on the right end of the wire as a result of conical tapering. (d) Reflectance as a function of nanowire tip length, clearly showing a significant reduction from 0 – 1 µm. The simulation procedure is the same as the one described in Sec. 8.4.

port (left border of the wire). The graph clearly shows how drastically the reflectance is reduced when the length of the tip increases. The reflectance decreases already from 0.48 to 0.01 when the tip increases from 0.12 to 1.0 µm and approaches zero for higher values. It should be mentioned at this point that tips in this length interval are indeed common among our NWs. The oscillations appearing in the curve arise from longitudinal resonances when the effective cavity length just matches a multiple of the wavelength inside resonator. To summarize, a strong end facet tapering has tremendous negative effects on lasing properties, as it severely degrades the quality of the resonator.

11.3 Reduction of mirror losses through tip detachment

As the strong conical tapering of the nanowire end facets reduces the reflectivity of the tip. Hence, nanowires with shortest possible tips are preferable. In the growth process however, one can not prevent the formation of such tips since there is always nucleation beneath the gold-gallium droplet during the radial shell growth (see Sec. 3.3.2). In order to reduce the mirror losses, we tried to implement a detachment of the tip after the growth process. Instead of a complex lithography and etching process, we present here a simpler method for removing the tip and show how the resonator quality is improved. Here. we

use thicker nanowires with diameters of 320 – 350 nm. Due to the prolonged radial growth time, these wires posses conical tips with a length of over 2 µm. The PL emission profile under pulsed excitation of such a wire is shown in Fig. 11.4 (a). There exist three bright spots where the light emitted from the nanowire is scattered into free space, namely where the form of the crystal deviates from the perfect wire-like shape. These are the nanowire bottom end facet, the junction between stem and tapered end facet, and a spot close to the tip. When we excited this wire with the same laser under continuous wave (cw) mode, the upper left emission spot vanished, as can be seen in Fig. 11.4 (b) showing the profile after cw excitation. The constant pumping under cw mode obviously heated the material in a way that the crystal was fully destroyed in the upper left part of the nanowire, as can be seen in the respective SEM in Fig. 11.4 (c). The conical end of the wire was tangent to a gold digit of the substrate's coordinate system. Obviously, the induced heat was strongest at contact point between the semiconductor material and the gold digit, as the crystal is destroyed, or even fully vaporized, between that point and the nanowire stem. The nanowire now terminates with a rather flat end instead of a long cone. The concomitant improvement of resonator quality becomes evident by comparing the emission spectra of the same wire before and after the heat-induced damage. The PL spectrum before cw excitation (Fig. 11.4 (c)) is quite broad with a FWHM of 41 nm and shows rudiments of FP-resonances. In the emission after the damage, however, the spectrum reveals a sharp lasing peak at $\lambda = 806$ nm and a FWHM = 1.3 nm (Fig. 11.4 (d)). The detachment of the tip significantly enhanced the optical gain such that the NW was able to lase. We only observed this in the presented, comparatively thick nanowires with $d \gg 300$ nm. We assume that a sufficient amount of gain material is needed to excite enough carriers to heat the crystal in this extend. Additionally, the larger diameter increases the absorption cross section and therefore the net excitation intensity of the wire.
Although this is a fast and easy method to improve the cavity reflectance, it involves some coincidence as the wire must be tangent to the gold on the right spot, which makes the control more difficult as the wires a randomly dispersed on the substrate. In other cases, the high cw excitation destroys the semiconductor in a way that it degrades the optical activity instead of improving the resonator quality. In further studies however, other methods for removing the tip should be explored, for example by improving the control of nanowire deposition or by the utilization of etching methods.

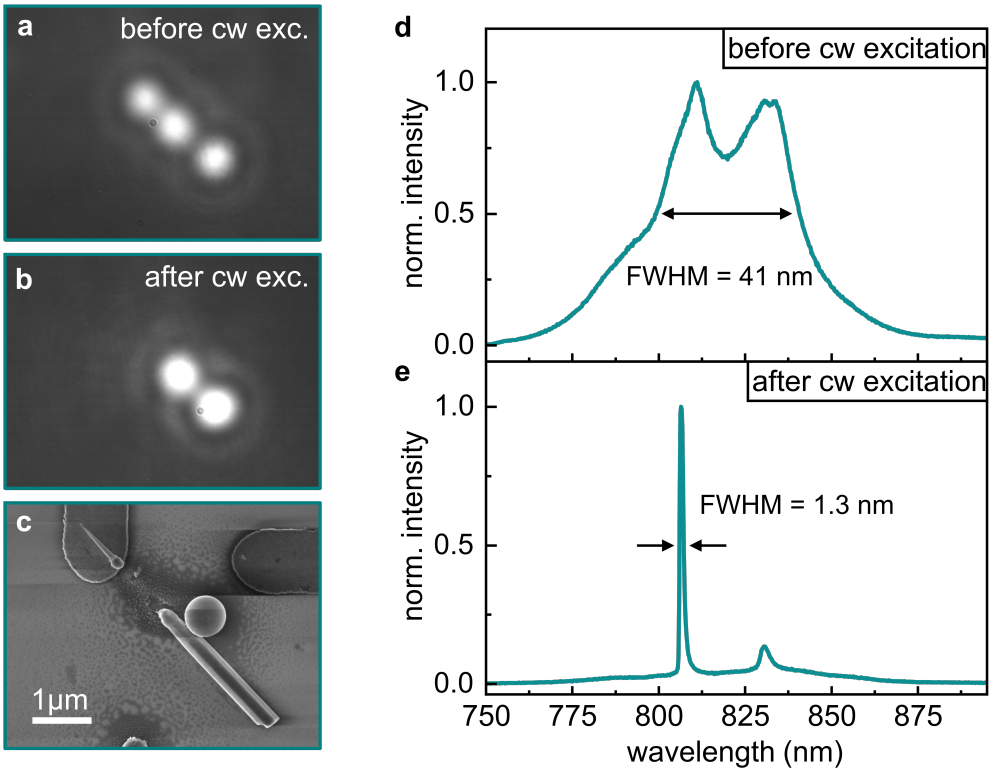

Figure 11.4: Detachment of the conical nanowire tip by heat-induced damage. (a) The PL emission profile exhibits three bright luminescence spots from the flat end, the transition where the tapering begins and from close to the thin tip. (b) After the nanowire was briefly excited with cw laser light at full power, the upper left spot vanished. (c) SEM of the respective wire, recorded after cw excitation. The micrograph shows the damages in the crystal induced by the high excitation. The material even fully vaporized between the nanowire stem and the spire. (d) The PL spectrum before cw excitation is quite broad and shows rudiments of FP-resonances, while in the spectrum after the damage a lasing peak is observed, shown in (e). Through the damage, the nanowire now terminates with a rather flat end instead of a long, conical tip, which significantly improves the reflectivity. The concomitant improvement of resonator quality then allows the nanowire to develop lasing. The spectra in (d) and (c) are recorded under pulsed excitation.

11.4 Conclusion

In this section, we have examined nanowires lying on a dielectric SiO_2 substrate in terms of their lasing capabilities. We have shown that their natural, elongated shape allows them to simultaneously act as optical waveguides as well as FP resonators which facilitate positive optical feedback through stimulated emission. We have further verified that the occurring emission peaks correlate very well with the longitudinal resonances of a nanowire cavity. In addition, we have outlined how the conical tapering strongly reduces the reflectivity of the end facet by means of numerical simulations and presented an experiment which showed how the resonator quality is improved when the tip is removed.
In further experiments, a more controlled method to detach the tip could improve the yield of nanowire lasers lying on a dielectric substrate, even for nanowire diameters around 200 nm, which is more desirable to ensure a sole amplification of the fundamental mode. In samples presented in Sec. 11.1, the resonator quality was not quite sufficient to observe lasing. In the next chapters, we present how to harness the field enhancement in the vicinity of a metal, in order to achieve lasing, by placing the nanowires onto a metallic surface.

12

GaAs nanowires as plasmonic nanolasers

The development of plasmonic devices has significantly advanced over the past twenty years and builds the basis of a large range of novel technological applications [151]. Among others, devices which are coupled to surface plasmons, benefit from a high optical power, the possibility of subwavelength optical confinement and a fast response enabling ultrafast modulation [152]. The localization of optical field by overcoming the diffraction limit is mandatory for the development of information processing in photonic integrated circuits. There is also a variety of other methods that exploit the field enhancement in the vicinity of a metal, such as surface-enhanced Raman scattering (SERS), surface-enhanced infrared spectroscopy (SEIRA) or surface plasmon-enhanced fluorescence spectroscopy (PEF) [153], to name but a few.
In this chapter, we show that through the deposition of nanowires onto a gold substrate, we increase the optical gain in a way that we are able to observe lasing in single nanowires. We first introduce the principle of surface plasmon polaritons (SPPs) and show how the coupling of propagating optical modes to SPPs changes their dispersion inside a nanowire. We then systematically evaluate the lasing behavior of single nanowires lying on gold by μ-PL spectroscopy and by comparing our experimental results with numerical simulations.

12.1 Basic principle of surface plasmon polaritons

Below the plasma frequency, a metal only supports evanescent electromagnetic fields, which exponentially decay into the bulk metal. The induced charge oscillations near the surface then form the class of *surface plasmon polaritons* (SPPs) [154]. These quasi-particles have combined character of an electromagnetic wave and surface charges as the charge oscillations at the surface induce an electric field normal to the surface

(y-direction) with a transverse magnetic component, as shown in Fig. 12.1 (a). The normal electric field E_y is enhanced near the surface and exponentially decays with distance from the metal/dielectric interface. The decay length δ_d into the dielectric is of the order of the half-wavelength of the created electromagnetic wave, and δ_m is determined by the skin depth of the metal [155]. The evanescent character of the wave reflects the bound and non-radiative nature of SPPs, as the optical power is inhibited to propagate away from the surface, while the propagation length of SPPs on a flat metal/dielectric interface can be on the order of tens of µm [152]. In the simplified example illustrated in Fig. 12.1 (a), the dispersion relation of SPPs propagating at the interface is expressed as [155]

$$k_{\mathrm{SPP}} = k_0 \sqrt{\frac{\epsilon_{\mathrm{d}} \epsilon_{\mathrm{m}}}{\epsilon_{\mathrm{d}} + \epsilon_{\mathrm{m}}}}, \tag{12.1}$$

with k_0 being the free space wave vector and ϵ_{m} and ϵ_{d} the frequency-dependent permittivity of the metal and the dielectric, respectively. The surface plasmon-dispersion is sketched in Fig. 12.1 (b) together with the light line, which describes the propagation of free space photons. The SPP dispersion curve lies on the right side of the light line and approaches the surface-plasmon resonance ω_{SPP} for large k_z. The surface plasmon resonance is thereby defined as $\omega_{\mathrm{SPP}} = \omega_{\mathrm{p}}/\sqrt{1 + \epsilon_{\mathrm{m}}}$, where ω_{p} is the plasma frequency of the metal. The coupling between electromagnetic field with charge oscillations thus increases the momentum as compared to a free space photon of the same energy. The large momentum therefore allows a much tighter spatial confinement of the SPP field as opposed to the diffraction limited light field.
Fig. 12.1 (b) shows that there is no crossing between the photon dispersion and the SPP dispersion. Hence, it is not possible to directly excite SPPs by illuminating the metal surface from the dielectric, since the energy and momentum conservation can not be satisfied between the photon and the SPP. Reversely, a SPP does not inherently radiate unless a mechanism of momentum transfer, like a grating or prism coupling, is applied.
When an emitter is located inside the SPP field, the enhanced E-field induces a change in emission rate according to Fermi's golden rule. Conversely, an emitter can excite an SPP by non-radiative energy transfer [156]. In the next chapter, we show how the dispersion and the mode profile change when the SPPs are coupled to the optical modes of our nanowire waveguide.

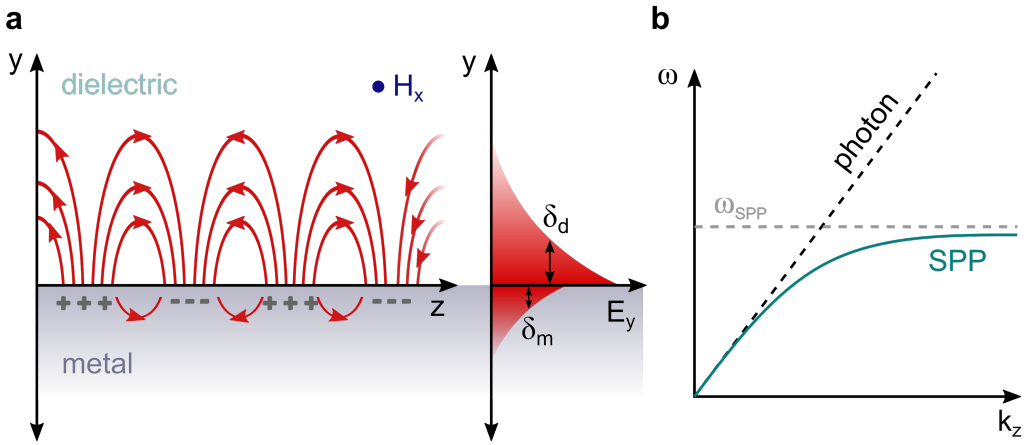

Figure 12.1: Basic principle of surface plasmon polaritons. (a) Sketch of the normal electric and transverse magnetic field that emerge through charge oscillations at the surface of a metal, building the class of surface plasmon polaritons. (b) Dispersion relation of SPPs compared with the dispersion of free space photons. Adapted from Ref. [155].

12.2 Transversal plasmonic waveguide modes

The coupling of optical fields to surface plasmon polaritons at the metal surface induces new waveguide eigenmodes. To illustrate the emergence of these new modes, we numerically evaluate the arising new dispersion in the context of the modal effective index as a function of wire diameter, as we did in Sec. 10.3 for the case of a nanowire lying on SiO_2. The simulation procedure is the same as described in Sec. 10.3, but now the SiO_2 substrate is replaced by a gold (Au) substrate with a refractive index of $\tilde{n}_{\mathrm{Au}} = 0.16 - 5.08i$ [157]. The results of the FEM simulations are shown in Fig. 12.2. The dispersion plot in Fig. 12.2 (a) reveals two new eigenmodes that arise from propagating surface plasmon polaritons, coupled to the optical waveguide, here plotted as gray dashed lines (SPP1 and SPP2). Both modes have a smaller cut-off diameter and a higher effective index than the purely photonic modes, pointing out their ability of larger field confinement due to a larger momentum as discussed in Sec. 12.1. Their field profiles can be seen in the respective images in Fig. 12.2 (b), displayed for a nanowire diameter of $d = 220\,\mathrm{nm}$. The red and blue arrows indicate the in-plane electric and magnetic field components (E_x, E_y) and (B_x, B_y), respectively. The fundamental surface plasmon polariton mode, designated as SPP1, is strongly confined within the interface between the metal substrate and the nanowire and has a field maximum in the center of the tangent facet. As defined for a SPP, the mode has a TM character with the magnetic field (blue arrows) transversely polarized and the electric field polarized normal to the metal surface. The higher order, SPP2 mode has two maxima close to the edges of the tangent nanowire facet with oppositely polarized, normal electric field components and is also strongly bound to the gold/NW interface.

We also plot the field distribution of the photonic $HE11_x$ and $HE11_y$ modes for the same diameter of $d = 220\,\text{nm}$ in Fig. 12.2 (b). The presence of surface plasmons distorts their mode profile as compared to the uncoupled photonic case discussed in Sec. 10.3. As a result of coupling to SPPs, a significant part of the propagating electromagnetic field is localized at the interface to the gold surface. In larger-diameter nanowires, the photonic modes decouple from the surface plasmons and regain their photonic character. Their mode profiles more and more resemble those of the photonic modes described in Sec. 10.3, as it is exemplarily shown for the largest calculated diameter of $d = 400\,\text{nm}$ in Fig. 12.2 (c). Hence, we refer to them as *photonic* modes in the following and employ the same mode designation ($HE11_x$, $HE11_y$, ...), as in Sec. 10.3. These photonic modes, which are plotted in color, only take effective index values between $n_{\text{eff}} = 1$ (light in free space) and the refractive index of GaAs. Together with their minimum cut-off diameter at around 200 nm for the $HE11_x$ mode (as in Sec. 10.3), this additionally points out their photonic character as they are subject to the diffraction limit. By contrast, the mode cut-off diameters of the plasmonic SPP1 and SPP2 modes are at $d = 70\,\text{nm}$ and $d = 140\,\text{nm}$, respectively. In addition, the effective mode indices can exceed the refractive index of GaAs. The SPP1 mode already takes an effective index of $n_{\text{eff}} = 3.83$ at $d = 150\,\text{nm}$, which indicates that the plasmonic modes posses a stronger optical confinement than it is possible in photonic waveguides.
The simulations shown in Fig. 12.2 demonstrate that the coupling to surface plasmons enables optical waveguiding below the photonic mode cut-off, which is at $d \approx 200\,\text{nm}$ for our GaAs nanowires. The photon-plasmon interaction thus may offer the opportunity to operate nanolasers at wire diameters much smaller than 200 nm. We will use these results to classify and interpret the experimental observations concerning the lasing behavior of our GaAs nanowires on gold in the subsequent sections.

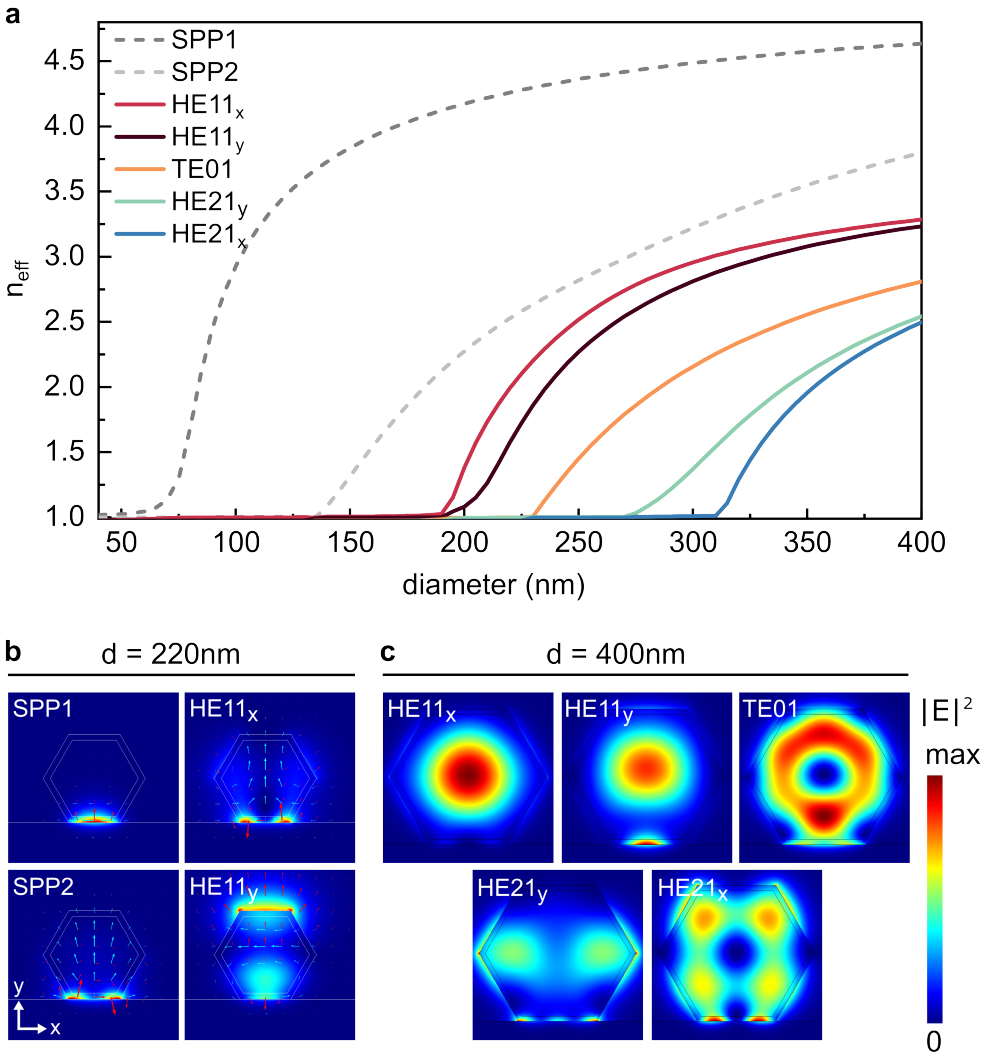

Figure 12.2: Wave propagation in nanowires lying on a gold substrate. (a) Effective modes index as a function of nanowire diameter. Two new eigenmodes arise due to the generation of surface plasmons (SPP1, SPP2), which have a smaller cut-off diameter and a larger effective index compared to the photonic modes, which points out a large optical confinement that is not restricted by the diffraction limit of light. (b) Electric field intensity profile for the four propagating modes in a wire with $d = 220\,\text{nm}$ (left side) with the electric and magnetic field components (E_x, E_y) and (B_x, B_y) as red and blue arrows, respectively. The field profiles show how the $\text{HE11}_{x,y}$ modes are influenced by the metal as a large part of the field is pushed to the metal boundary. This influence weakens at larger wire diameters, as the field distribution of the photonic modes, here exemplarily shown for $d = 400\,\text{nm}$ (right side), strongly resembles those of a nanowire lying on SiO_2. The color scale is not the same in the different images.

12.3 µ-PL characterization of nanowires on gold

12.3.1 Sample preparation

As presented in Sec. 12.2, the coupling of optical modes to surface plasmons concentrates a high fraction of the energy into propagation at the interface of the optical cavity and the metal surface. In order to ensure a long propagation distance of the coupled SPP modes, metal substrates with an atomically flat surface are desired: A large surface roughness or many grain boundaries would lead to high scattering of SPPs, accompanied by high propagation losses and thus impractically high lasing thresholds [158]. To avoid the problem of polycrystalline Au films, that are for example provided by deposition methods like sputtering or thermal evaporation, we produce our plasmonic devices using molecular-beam epitaxy. For the basis substrate, we use commercial GaAs(001) wafers. These wafers are initially transferred into the III-V MBE chamber to grow an atomically flat GaAs buffer. After the GaAs deposition, the wafers are *in-situ* transferred into the metal/oxide-MBE chamber. First, a thin 1 nm iron (Fe) layer is grown, before depositing Au onto the substrate. The thin Fe layer acts as diffusion barrier and prevents the gold from interacting with GaAs. As shown in Fig. 12.3 (a) and (b), the presence of the thin Fe layer makes a great difference in surface roughness. The upper panels show the atomic force micrographs (AFM) of a structure without an Fe barrier layer (a) and with an inserted Fe layer (b). The evaluation of the micrographs yield root mean square (rms) values of $rms = 0.22\,\text{nm}$ without and $rms = 0.11\,\text{nm}$ with a Fe barrier layer. Hence, the average surface roughness has halved through the integration of a 1 nm thin Fe layer between the GaAs substrate and the Au. The improvement of surface roughness is also seen in the respective SEM images (lower panel) of the two structures. In (a), there are clear irregularities on the gold surface, while the gold surface in (b) is very smooth. The scratches in the upper left part of the SEM images were intentionally added to allow the adjustment of the focus of the microscope. The atomically smooth surface of the structure in Fig. 12.3 (b) makes it the perfect substrate for plasmonic waveguiding and is therefore applied as the substrate for our nanowires. The final device layout with the NW on top is illustrated in Fig. 12.3 (c).

12.3.2 Lasing characteristics and analysis

We now present the power-dependent µ-PL studies performed on individual nanowires lying on a MBE-grown Au substrate. An exemplary power series is shown in Fig. 12.4 (a), recorded under pulsed excitation at 40 MHz repetition frequency and a non-resonant excitation wavelength of 690 nm. The nanowire stems from the same MBE growth run as the wire presented in Fig.11.1 (c) on SiO_2. It has a total diameter of $d = 230\,\text{nm}$ and a length of $L = 5.73\,\mu\text{m}$. At the lowest pump pulse fluence of $p = 38\,\mu\text{J/cm}^2$, the spectrum consists of a single, broad spontaneous emission peak (light brown curve), centered around $\lambda = 819\,\text{nm}$. The periodic modulation of the spectrum with increasing excitation furthermore reflects the manifestation of longitudinal Fabry-Pérot modes inside

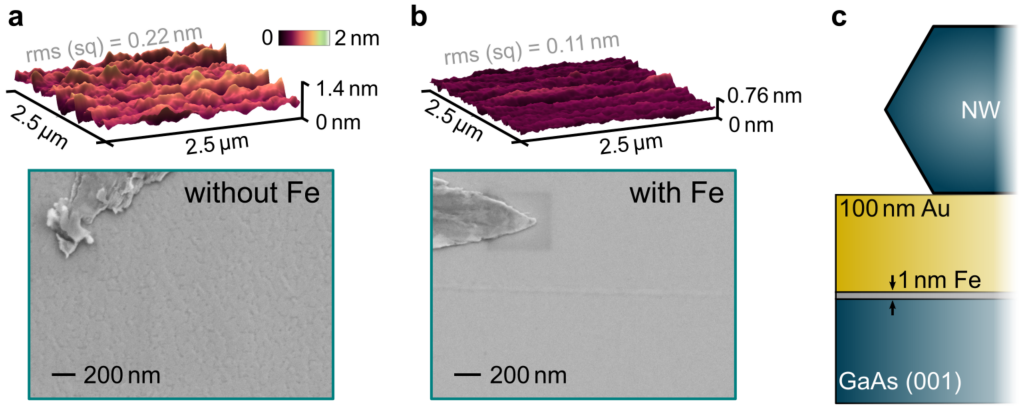

Figure 12.3: Sample preparation for plasmonic experiments. (a) AFM (upper panel) and SEM (lower panel) images of the metal substrate when the Au was directly deposited onto the GaAs substrate. The gold reacts with the underlying GaAs, which causes a higher surface roughness. (b) By inserting a thin Fe layer between the GaAs and the Au layer, the surface roughness can be significantly improved. (c) Final device structure that is used for plasmonic experiments.

the nanowire cavity, as discussed in Sec. 11.1. In contrast to the excitation dependence of the wires in SiO_2 (see Fig. 11.1 (c)), we now observe a sudden increase in emission intensity of one of the FP resonances centered around $\lambda = 813\,\text{nm}$, which we interpret as lasing of this single NW. At the highest chosen excitation of $p = 458\,\mu\text{J/cm}^2$ (dark blue), the peak intensity is almost two orders of magnitude higher than the spontaneous emission background (note the logarithmic scale on the y-axis). This indicates that the cavity gain now exceeds all cavity losses and all emitted photons emit into this one lasing mode, while the gain for the remaining frequencies is clamped. The clamping is evident at higher pump intensities, where the spontaneous emission background does not significantly change anymore over a wide range of excitation power (note the little differences in the SE background between the turquoise and the dark-blue spectra). Another indication of our excitation of coherent laser emission is given by the appearance of an interference pattern of the emitted light at high excitations, as seen in the real-space emission profile of a lasing wire from the same substrate in the inset of Fig. 12.4 (a). The interference pattern emerges as the scattered light at the nanowire end facets behaves as two point sources, which emit the coherent light that is amplified inside the nanowire cavity [18, 159, 160].

For a further analysis of the lasing behavior of this particular wire, we now investigate the input-output (I-O) characteristic that was introduced in Sec. 10.5. Technically, the I-O characteristic, from which essential lasing parameters like the lasing threshold or the β-factor are commonly determined, is strongly influenced by how the output power is defined. We demonstrate this by the analysis shown in Fig. 12.4 (b). Here, the output intensity was extracted from the power-dependent emission spectra, shown in (a), in three

different ways: The squares feature the global intensity maximum as a function of pump intensity ("max. intensity"), the circles represent the output power when the spectra are integrated over the entire energy range, and the triangles the integrated area underneath the lasing peak only (integrated in the spectral range from 811 nm − 819 nm), without the spontaneous emission background. In order to compare these three output-curves, each of them was normalized to their maximum intensity. We recognize the following: The output characteristic of the maximal intensity and the integrated lasing peak follow almost the same dependence. They exhibit a smooth, but still obvious kink, or "knee-like" behavior, which marks the transition from the spontaneous emission to the lasing regime. However, the I-O characteristic is substantially different when we integrate over the entire spectrum and thus take the spontaneous emission background into account. In that case, there is no obvious transition from the SE to the lasing regime and the output intensity follows a roughly linear dependence on the input power. We attribute the lack of visible lasing transition in the "full spectrum" curve to an overestimation of the spontaneous emission intensity as compared to the collected laser emission from the NW. As the spontaneous emission homogeneously radiates into all spatial directions, the collection efficiency into the objective is larger than for the laser light, which mainly radiates away from the NW in axial direction [19, 143]. This becomes evident when we compare the integrated intensity of the full spectrum, the integrated intensity of the SE background (integrated spectrum without the lasing peak) and the integrated intensity of the lasing peak only, which are plotted in Fig. 12.4 (c) on a double-logarithmic scale. Until an excitation of 100 $\mu J/cm^2$, the total intensity is dominated by the spontaneous emission, which saturates for higher pump powers due to gain clamping, but is still by a factor of ten stronger than the lasing peak intensity. The lasing peak, on the other hand, increases by almost two orders of magnitude between $p = 100\,\mu J/cm^2$ and $p = 458\,\mu J/cm^2$, and clearly displays the transition from the super-linearly increasing ASE regime to the linearly increasing lasing regime. The two linear regions are traced by the red lines to guide the eye. Hence, by calculating the light output through integration of the full spectrum, the overestimation of spontaneous emission intensity may lead to an incorrect evaluation of the spontaneous emission factor β as well as of the lasing threshold [143]. However, when we only take the lasing peak into account, the spontaneous emission is completely neglected and the data do not reveal the typical "S"-shape. For a consistent evaluation of all our lasing nanowires, we therefore take the maximum intensity of the emission spectra as lasing output.

The corresponding, final I-O characteristic of this wire together with the FWHM is presented in Fig. 12.4 (d). The light output now exhibits the characteristic, non-linear "S"-shape (blue curve), and the line width (red curve) promptly drops from 10 nm to 1 nm, which is a clear indication of the onset of lasing. The lasing threshold pump power is marked by the gray dashed line in the graph. The high β-factors of such nanolasers makes the transition to the lasing regime and thus a distinct threshold less obvious (cf. Fig. 10.6 (a)). Hence, we determine the threshold by linearly fitting the output curve (on a linear scale) at high pump intensities, where the x-axis intercept of this straight line then denotes the threshold pump power, as shown in panel (b). For the presented nanowire,

we determine a lasing threshold of $p_{\mathrm{th}} = 190\,\mu\mathrm{J/cm^2}$. To ensure a consistent threshold evaluation, this procedure was applied for all lasing nanowires throughout this thesis.

12.3.3 Mode identification

In the previous section, a stable lasing behavior of a nanowire on gold was demonstrated. However, we only observe lasing properties for a small share of nanowires lying on the gold substrate, which implies that the majority of the measured nanowires does not form a cavity with high enough quality to ensure low-loss optical waveguiding and sufficient positive optical feedback. For the optimal design of nanolasers, it is crucial to understand the internal mechanisms that lead to lasing, including the knowledge of which optical mode is amplified in the nanocavity, as well as geometrical factors that affect the resonator quality. We have already discussed in Sec. 11.2, that the end facet tapering plays a major role in resonator quality, since we found a long, conical tip to significantly diminish the mirror reflectivity. The total wire diameter also is a key parameter, as it defines the presence of optical modes that can be amplified. Hence, we experimentally investigated how the shape of the nanowires affects their lasing capability: A total of 45 nanowires were examined in terms of their lasing performance using µ-PL spectroscopy, before their dimensions were determined via SEM. The presented nanowires have a diameter of $d = 200(\pm 30)$ nm. In Fig. 12.5 (a), we summarize all nanowires studied in this context and plot their total diameter, as determined by SEM, as a function of their tip length. The wires that exhibited a clear lasing behavior are plotted as turquoise spheres, while the black squares represent those wires for which the PL emission did not exceed the ASE regime. It can be seen from this statistics that, among these data, no lasing was observed for wires with diameters below a critical diameter $d = 200\,\mathrm{nm}$. Moreover, among the nanowires with $d > 200\,\mathrm{nm}$, lasing could only be observed in those where the tip length did not exceed 1.5 µm, with the exception of the 230 nm wire. For the sake of completeness, it should be mentioned here that we did not observe any dependence of the lasing behavior on the total NW length, or resonator length L, respectively, which ranges from $L \approx 5 - 7\,\mu\mathrm{m}$. Based on the results in Fig. 12.5 (a), we find it highly unlikely that the dominant lasing mode is a plasmonic SPP mode. On the one hand, most of the SPP mode's energy propagates along the NW/gold interface and does not directly impinge on the NW end facet, or tip, respectively. The reflectivity, and thus the corresponding resonator quality, of an SPP mode should therefore not be dependent on the shape of the NW end facet. On the other hand, the determined, critical lasing diameter coincides with the mode cut-off of the photonic HE11 modes of $d \approx 200\,\mathrm{nm}$ (cf. Fig. 12.2 (a)), which underlines the assumption that only photonic modes are amplified.
To verify this, we numerically evaluate the group indices n_g of the different modes for various diameters and compare them with the experimentally determined group indices of all measured NWs that showed at least FP resonances. To numerically evaluate the

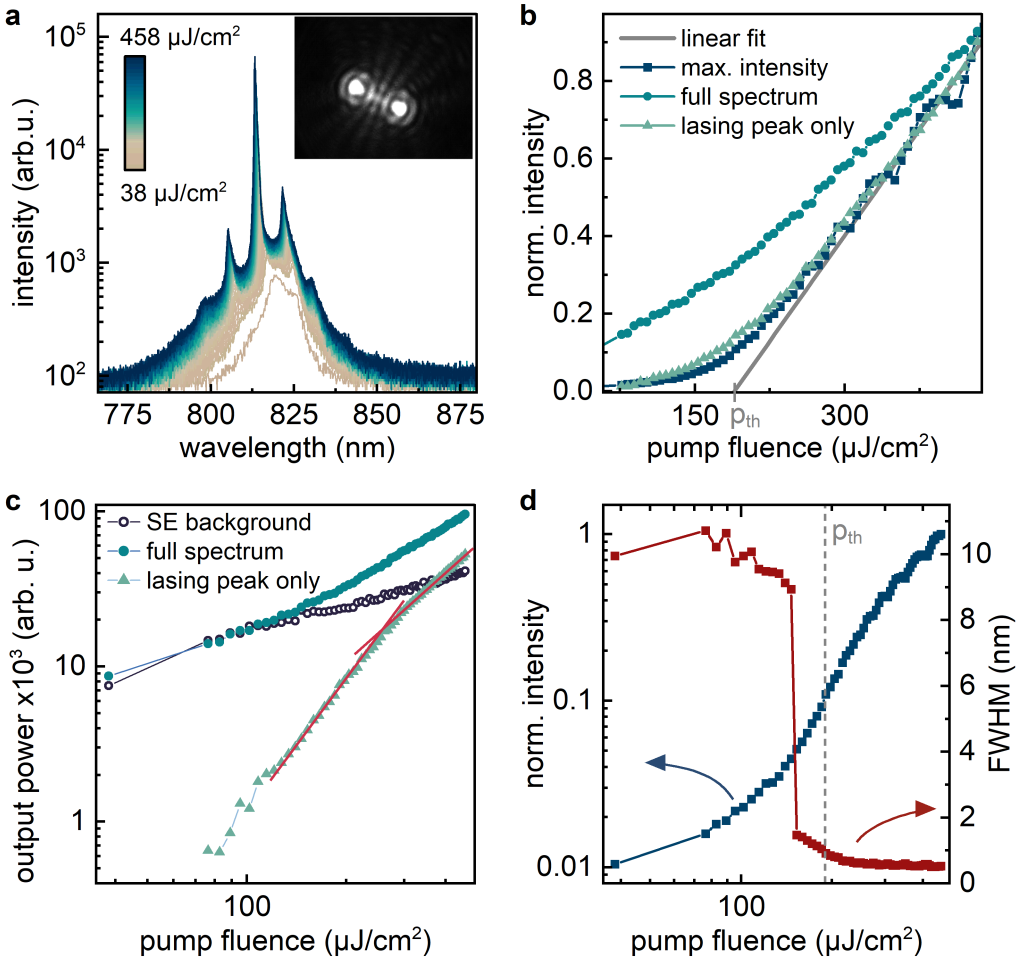

Figure 12.4: Lasing characteristic of a nanowire on gold with $d = 230$ nm and $L = 5.73$ µm. (a) Power dependent emission spectra with several FP resonances and one amplified lasing peak. Inset: Emission profile of a lasing nanowire showing clear interference fringes that are indicative of coherent radiation generated inside the NW cavity. (b) Linear representation of the intput-output curves evaluated by three different methods. (c) Comparison of the integrated intensities of the entire spectrum with the SE background and the lasing peak. The graph reveals how the SE is overestimated as a result of varying collection efficiency of spontaneous emission and laser output. (d) I-O plot of the maximum intensity value showing the characteristic, non-linear "S"-shape. The concomitant line width drop is a strong indication of the onset of lasing.

group index, we use Eq. 10.3:

$$n_g = n_{\text{eff}} - \lambda \left(\frac{\mathrm{d}n_{\text{eff}}}{\mathrm{d}\lambda} \right),$$

and simulate the frequency dependence of n_{eff} in the range of $\lambda = 750 - 850\,\text{nm}$ for the first four modes and for various diameters. For each mode and each diameter, $(\mathrm{d}n_{\text{eff}}/\mathrm{d}\lambda)$ was then obtained by a linear interpolation of $n_{\text{eff}}(\lambda)$. The experimentally determined group indices are determined according to Eq. 10.2 by using the measured, longitudinal mode spacing $\Delta\lambda$ of the each investigated nanowire:

$$n_g = \frac{\lambda^2}{2L\Delta\lambda}.$$

We determined the group indices for a wavelength of $\lambda = 820\,\text{nm}$. For the resonator length L, we took the length of the nanowire stem. The obtained theoretical and experimental values are plotted together in Fig. 12.5 (b). Apparently, the plasmonic modes, SPP1 and SPP2, have moderate and nearly constant group indices of $n_g = 5$ for all diameters above $d = 150\,\text{nm}$. The measured nanowires, however, all exhibit very large group indices of values between 6 and 9, depending on the diameter, which is in excellent agreement with the calculated values of the HE11_x and HE11_y mode. This, together with our observation from Fig. (a), confirms our suggestion that the photonic HE11 mode is the dominant lasing mode.
Due to the high overlap of the two photonic HE11 modes, Fig. 12.5 (b) does not indicate which polarization state is more likely to lase. To that end, the polarization analysis presented in Figs. (c) and (d) should provide further information on which of the two modes is the dominant one. As outlined in Sec. 8.4, we expect a dominantly y-polarized guided wave (polarization normal to the substrate) to show a far-field radiation intensity which is dominantly polarized along the nanowire axis (z-direction). Hence, the dominant polarization of the HE11_y mode, analyzed in the far-field, is parallel to the wire axis (z-polarization), while the polarization of the HE11_x mode is predominantly polarized perpendicular to the wire axis (x-polarization). This was also deduced in Ref. [139] for photonic modes in single InP nanowires. Fig. 12.5 (c) shows the bimodal lasing spectra of a typical lasing nanowire ($d = 190\,\text{nm}$, $L = 5.1\,\mu\text{m}$), analyzed parallel (black) and perpendicular (red) to the wire axis and the respective emission profiles (insets). The emission profiles indicate strong optical waveguiding as almost no luminescence radiates into the far-field until the light is scattered from the end facets. Additionally, the perpendicularly (x-polarized) emission is much brighter than the parallel (z-polarized) emission, which is also observed in the total PL intensity of the lasing spectra. The angle-resolved PL intensity in a polar plot is shown in Fig. 12.5 (d) together with the SEM image of this wire. The integrated intensity reveals a high degree of linear polarization, regardless of whether we consider the entire spectrum or only one lasing peak (the polarization analysis in Fig. (d) was performed for the longitudinal mode centered around $\lambda = 807\,\text{nm}$). Both curves reveal the same angular dependence. We extract high degrees

of linear polarization of DLP = 0.86 for the full spectrum and DLP = 0.74 for the lasing peak. Hence, all data shown in Figs. 12.5 (c) and (d) strongly suggest that the $HE11_x$ mode is the dominant transverse lasing mode.
Summarizing, we have systematically evaluated the lasing behavior of our GaAs nanowire lying on gold in terms of their geometrical shape and morphology. Moreover we have identified the dominant lasing mode by comparing the experimentally and theoretically determined group indices combined with a detailed polarization analysis. To probe the cause of our observation, we will further analyze the confinement factor and modal threshold of nanowires on gold in Sec. 12.4. Before that, we will briefly discuss the main differences between lasing operation in cw and pulsed mode in the next section.

12.3.4 Continuous wave and pulsed operation

So far, we have focused on the analysis of nanowire lasers that are optically pumped using pulsed laser excitation. Pulsed excitation benefits from a lower risk of heat-induced damage to the crystal, since optically induced heat can easily dissipate to the surrounding or the substrate between the excitation pulses [161]. Furthermore, the concentration of the laser energy to short pulses raises the peak intensity of the exciting laser light and consequently facilitates population inversion. We find our nanowires, however, also to operate in the cw mode, which may be required for some practical applications, but is often difficult to achieve as the high optical, time-integrated power necessary to obtain lasing can induce strong heating effects (see Sec. 11.3). In this section, we therefore concisely summarize the main differences in emission between pulsed and cw excitation.
In Fig. 12.6, the pulsed (a) and cw (b) mode of a lasing wire are compared. In Fig. 12.6 (a), the power-dependent emission spectra of the wire under pulsed excitation are shown. The multiple longitudinal modes clearly feature a strong blue-shift with increasing excitation and the individual peaks exhibit a broad low-energy tail. By contrast, the blue-shift of the peaks in cw mode is less prominent and all peaks are homogeneously broadened. The spectral blue-shift of the peaks can be explained by the effect of band filling, which increases with pump power and shifts the emission to higher energies [162]. The stronger shift under pulsed excitation compared with the cw excitation indicates that the higher peak intensity of the excitation pulses generates more charge carriers, which is accompanied by a more efficient band filling. The generated carrier density, however, is not steady during one excitation cycle, but degrades after the excitation is terminated (which is after the duration of our excitation pulse laser of $\sim 50\,\mathrm{ps}$). Hence, population inversion is not guaranteed for all times. After the initial, fast depopulation through stimulated emission, the emission afterwards is affected by parasitic ASE and SE, which are lower in energy. As a result, the time-integrated spectra under pulsed excitation feature various states of band filling which leads to the low energy tail of the individual peaks. In cw mode, however, a steady-state condition for gain and losses is established, resulting in a homogeneous broadening of the resonance peaks [161].

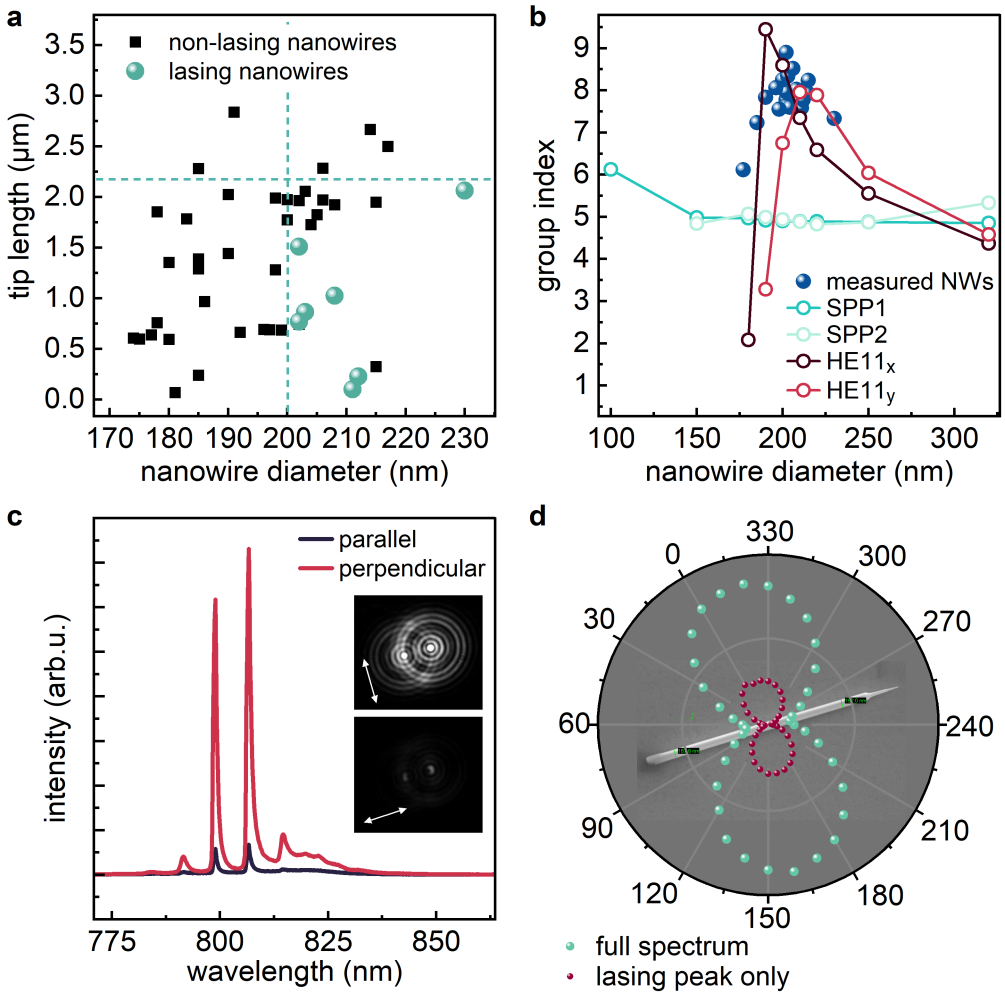

Figure 12.5: Mode identification of nanowires lying on gold. (a) Summary of in total 45 nanowires, investigated with regard to their lasing capability. The occurrence of lasing is dependent on the total nanowire diameter and the length of the tapered end facet. (b) Group indices as a function of nanowire diameter. The comparison between the theoretically and experimentally determined group indices shows a high agreement of the measured values with the photonic $HE11_x$ or $HE11_y$ mode. (c) Polarization resolved lasing spectra of an exemplary lasing nanowire (d = 190 nm, L = 5.1 µm), which clearly shows a dominant linear polarization perpendicular to the wire axis. The respective emission profile (insets) further indicate strong optical waveguiding. (d) Polar plot of the PL intensity integrated over the full spectrum (turquoise spheres) and over the lasing peak only (red spheres), both showing the same angular dependence and high DLP values of DLP = 0.86 and DLP = 0.74, respectively. From the observations made in Figs. (a)-(d), it can be concluded, that the $HE11_x$ mode is the dominant mode in our GaAs nanowires on gold.

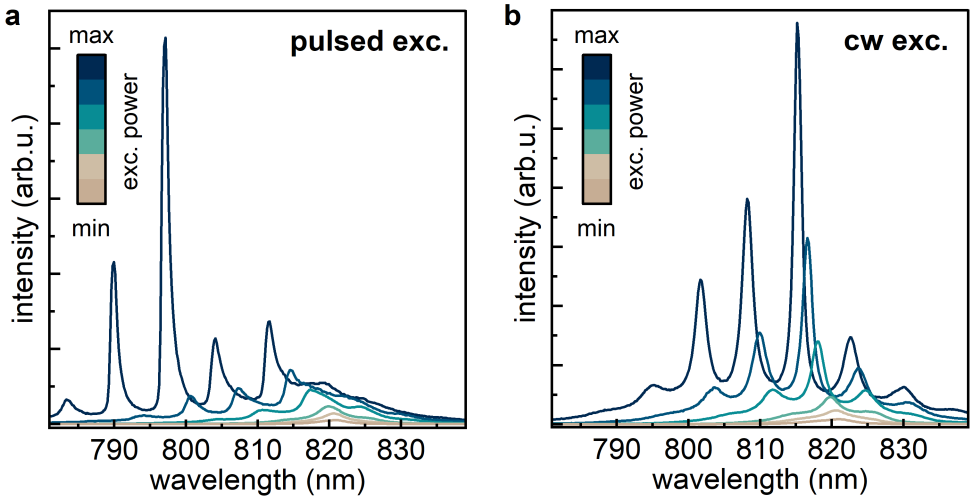

Figure 12.6: Spectral differences between a nanowire laser operating in pulsed and cw mode. (a) Power-dependent spectra under pulsed excitation. With increasing excitation intensity, a strong blue-shift of the longitudinal modes is observed. The amplified peaks furthermore reveal an asymmetrical shape. (b) The peaks of the longitudinal modes of the nanolaser operating in cw mode are homogeneously broadened and the blue-shift is less pronounced as compared to the pulsed mode shown in (a).

12.4 Confinement factor and modal threshold of nanowires on gold

After the systematic experimental analysis on the lasing behavior of GaAs nanowires lying on gold, presented in the previous sections, we now want to gain a better understanding of the underlying mechanisms. In this section, we therefore further analyze the key factors that can be extracted from the numerical FEM simulations, as it was already presented in Sec. 10.4 for nanowires on SiO_2. The calculated, diameter-dependent confinement factor Γ is shown in Fig. 12.7 for the SPP1, SPP2, $HE11_{x,y}$ and TE01 mode. Though the optical energy of plasmonic modes is strongly localized at the NW/metal interface and thus tightly confined within an infinitely small region, the confinement factor, calculated according to Eq. 10.6, is much smaller than for the photonic modes. This is because the overlap of the electric energy with the gain medium - the GaAs core - is small for the SPP1 and SPP2 mode compared to the total transported energy. On gold, we find the confinement factor of the photonic modes to be even larger than that of their counterparts in the case of a SiO_2 substrate (cf. Fig. 10.5 (a)). Here, the $HE11_x$ mode reaches a maximum value of $\Gamma = 1.8$ at $d = 225$ nm.
The propagation losses α_p of the plasmonic modes (SPP1 and SPP2), shown in Fig. 12.7 (b), exceed those of the photonic modes nearly over the entire diameter range, which directly reflects the ohmic damping caused by a high field overlap of the waveguide

modes with the metal substrate. We can again estimate the diameter-dependent, *modal* threshold of a nanowire laser, now on gold, represented by the relation α_p/Γ in Fig. 12.7 (c). Over the entire diameter range, the plasmonic SPP1 mode has a very high and almost constant modal threshold gain value of $\alpha_p/\Gamma > 12 \times 10^3\,\mathrm{cm}^{-1}$, suggesting that lasing from the SPP1 mode is more difficult to achieve as it requires higher pump intensities. Experimentally, we solely observe lasing in GaAs nanowires that exhibit a total diameter larger than $d = 200\,\mathrm{nm}$. At this diameter, the modal threshold gain is lowest for the $\mathrm{HE11_y}$ mode, closely followed by the $\mathrm{HE11_x}$ mode. This result is in contrast to the experimental findings (Sec. 12.3.3), where we evaluated the $\mathrm{HE11_x}$ mode to be the dominant lasing mode and therefore the mode with the lowest threshold. The reason for this discrepancy has yet to be established, but it is likely that the critical parameter here is the modal reflectivity on the end facets, which can be different for the $\mathrm{HE11_x}$ and $\mathrm{HE11_y}$ mode, especially when the degeneracy between these two modes is lifted [18, 111].
For comparison, we added the diameter-dependent threshold of the fundamental HE11 mode of a nanowire on SiO_2 (cf. Fig. 10.5 (a)) to the graph (dashed line). For all diameters above $d = 170\,\mathrm{nm}$, our simulations reveal, that the modal threshold of the purely photonic HE11 mode of a NW on SiO_2 is lower than for all waveguide modes in a NW lying on gold. From only the simulations, one could assume that lasing in nanowires is easier to achieve when they are lying on a dielectric SiO_2 substrate. However, this is in contrast to our experimental results, since only the nanowires on gold exhibited lasing. One hypothesis may be the more efficient reflection of the excitation laser on the gold surface, as we discuss in the next section.

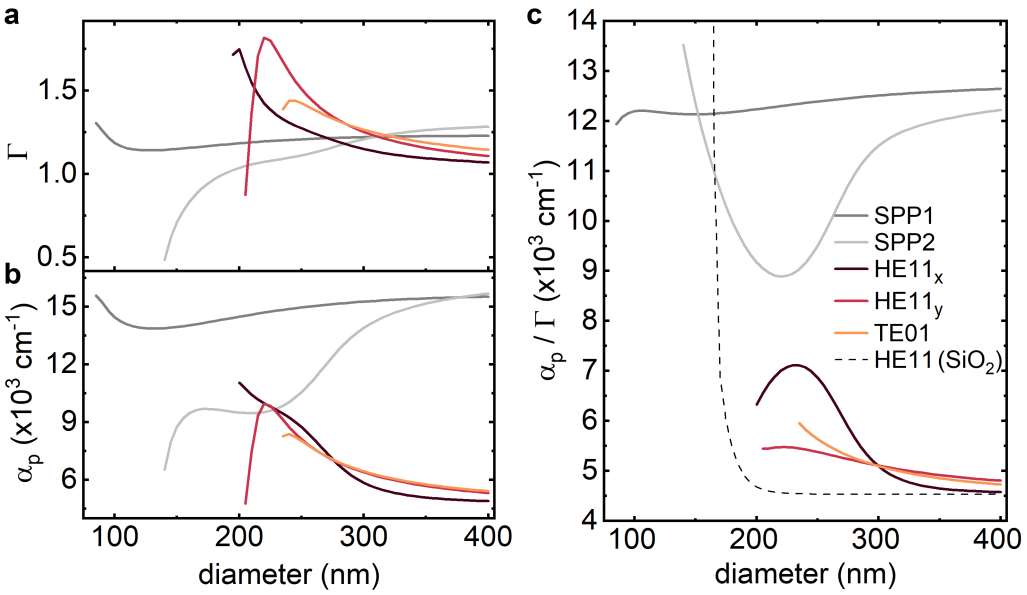

Figure 12.7: Modal threshold gain of a nanowire lying on a gold substrate. (a) Calculated confinement factor as a function of total nanowire diameter of the SPP1, SPP2, HE11$_{x,y}$ and TE01 mode. (b) Respective mode propagation loss α_p. The high propagation losses of the plasmonic modes are caused by ohmic damping and a large overlap of the optical field with the metal. (c) Threshold gain estimate α_p/Γ. The high damping results in much higher threshold values for the plasmonic modes as compared to the photonic modes, which makes it more difficult to achieve lasing of the plasmonic modes. The dashed line is the modal threshold of the fundamental HE11 mode on SiO_2 (cf. Fig. 10.5 (b)) and serves as reference.

12.5 Conclusion

In contrast to nanowires lying on a dielectric substrate, nanowires on a gold substrate are capable of lasing with the optical pumping available in the present study. In this chapter, we have systematically investigated the lasing characteristic of our GaAs nanowires and identified the dominant lasing mode with the support of numerical FEM simulations. We showed that through the presence of surface plasmons, two new waveguide eigenmodes (SPP1 and SPP2) appear, which are based on surface plasmon propagation and therefore tightly confined to the NW/metal interface. Though both of these modes have a smaller mode cut-off diameter than the photonic modes, no lasing was experimentally achieved in nanowires with diameters smaller than the photonic mode cut-off of $d \approx 200\,\mathrm{nm}$. Based on this, we have identified the photonic-like $\mathrm{HE11_x}$ mode as the dominant experimental lasing mode in all studied lasing NWs. Furthermore, our numerical simulations have revealed a significantly higher modal threshold for the SPP modes than for the photonic modes, as a result of damping.
Our simulations have also shown a lower modal threshold for the HE11 mode on SiO_2 than for the respective mode one the gold substrate. This is in contrast to our experimental results, as no lasing was observed in nanowires on a SiO_2 substrate. The specific cause for the improved lasing performance of the investigated nanowires on the gold substrate, as compared to the SiO_2 substrate, is to be the subject of future studies. Nonetheless, we want to propose three effects that may lead - alone or in combination - to an enhanced lasing efficiency when the nanowires are lying on a metal substrate. These effects mainly result from an increased light-matter interaction of the charge carriers with the enhanced field close to the metal: (1) A SPP enhanced emission rate into the lasing mode can lower the threshold [80]. This emission rate enhancement is for example also used in surface plasmon-enhanced luminescence, fluorescence or Raman spectroscopy [153, 163, 164]. (2) The energy transfer from SPPs to the excitons in the gain material modulates the carrier concentration and improves the efficiency of band filling, which is also referred to as SPP-enhanced Burstein-Moss effect [165]. (3) Another reason for the improved lasing performance may simply be the better reflection of the excitation laser light on the metal substrate than compared to a dielectric substrate. The enhanced reflection increases the net power with which the nanowire is stimulated and thus makes the provided pump power of our excitation laser sufficient to induce lasing.
To further study the role that photonic-plasmonic coupling may play in connection with lasing in nanowires, we experimentally investigate the hybridized plasmonic waveguide design in the next chapter.

13

Hybrid-plasmonic waveguides and lasers

The idea of hybrid-plasmonic waveguides aims to reach a trade-off between advantages (optical confinement) and limitations (propagation length, plasmonic damping) of plasmon lasers [154]. In this chapter, we realize this concept and examine it in terms of the lasing performance of our GaAs nanowires. First, the general concept of mode hybridization is introduced with respect to the change in mode propagation in comparison with the previous structures, presented in Chs. 11 and 12. We will further present how the mode dispersion changes in the photonic limit when we increase the dielectric spacer thickness. Afterwards, similar to Sec. 12.3.3, we identify the dominant lasing mode in our NW waveguides and finally evaluate how the integration of the insulating gap affects the lasing performance.

13.1 Concept of a hybrid-plasmonic waveguide with a nanoscale dielectric layer

In photonic devices, the light confinement is diffraction limited, while in devices coupled to surface plasmons, the overlap of an optical mode with the metal results in ohmic damping. Subsequently, the latter suffer from high losses, which induce high lasing threshold values. An auspicious concept is the so-called hybridized plasmonic waveguide structure, where a few nanometer thick, low-index dielectric layer is sandwiched between the high-index, semiconductor NW and the plasmonic metal substrate. This design is meant to overcome the limitations of the purely photonic and purely plasmonic concepts and in addition combine their advantages [166]. The concept was first theoretically proposed by Oulton *et al.* in 2008 [141] and subsequently experimentally verified by the same group in 2009 [127]. They demonstrated lasing from a hybridized mode in a CdS nanowire, which was separated by a nanometer thin, insulating MgF_2 gap from a silver surface. In the following, we present the realization and the concept of a hybrid-plasmonic

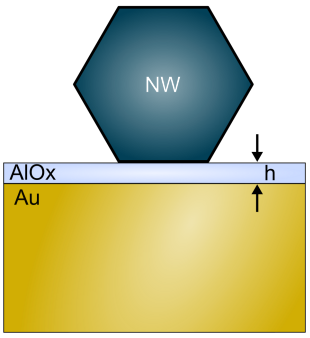

Figure 13.1: Device structure of the hybridized waveguide design. The substrate fabrication is equal to the one presented in Sec. 12.3.1, but now a thin, dielectric AlOx-layer was deposited on top. This layer serves as low-index, dielectric spacer between the NWs and the metal substrate.

waveguide with our wurtzite GaAs core-shell nanowires, placed on a metallic Au-substrate that is coated with an insulating aluminum oxide layer of variable thickness.

13.1.1 Sample design

The samples, which we will present in this chapter, are similar to those presented in Sec. 12.3.1, but the atomically flat gold layer is covered with a thin, dielectric layer. As dielectric material, we use thin layers of aluminum oxide (AlOx), which were deposited on top of the gold either by an atomic layer deposition (ALD) process, or *in-situ* after the gold deposition in the metal/oxide MBE chamber. In the following sections, we will investigate and compare the lasing behavior of nanowires, which are dispersed on substrates coated with different AlOx layer thicknesses of $h = 5\,\text{nm}$, $h = 7\,\text{nm}$, $h = 10\,\text{nm}$, $h = 15\,\text{nm}$ and $h = 20\,\text{nm}$. These AlOx layers will serve as a low-index, dielectric spacer between the nanowires and the metal substrate. The final structure is sketched in Fig. 13.1.

13.1.2 Hybridized waveguide modes

The integration of a thin, low-index dielectric spacer between the nanowire and the gold substrate significantly changes the way of how an electromagnetic wave propagates along the waveguide. In analogy to the structures described in the previous chapters, we simulate the mode dispersion with an integrated, thin AlOx layer between the gold substrate and the nanowire. We approximate the refractive index of the AlOx layer by assuming a mono-crystalline Al_2O_3 material with $n_{Al_2O_3} = 1.76$ [167]. The other numerical parameters are the same as in Secs. 10.3 and 12.2, respectively. The effective indices of the first four modes are shown in Fig. 13.2 (a). The coupling of the photonic modes to the surface-plasmon field generates new eigenmodes, here referred to as *hybrid*

surface plasmon (HSP) modes. We identify two of these strongly coupled modes, the fundamental HSP1 mode (dark brown curve) and a higher order, HSP2 mode (green curve). The HSP1 mode exhibits the highest effective index over the entire diameter range and has a small cut-off diameter of $d = 75\,\text{nm}$. Similar to what we observe for the purely plasmonic SPP modes of a nanowire lying on gold (cf. Fig. 12.2 (a)), the lower limit of the mode indices of the HSP modes is $n_{\text{eff}} = 1$. However, in contrast to the SPP modes, the mode index of the HSP1 mode does not exceed $n_{\text{GaAs}} = 3.67$, which reflects the plasmonic/photonic hybrid nature of the HSP modes.
We will now discuss the calculated mode profiles in Fig. 13.2 (b) in more detail: Regardless of the NW diameter, the HSP1 mode is strongly confined within the thin AlOx layer (see HSP1 profile at $d = 190\,\text{nm}$ and $d = 400\,\text{nm}$) and neither displays characteristics of a pure SPP mode nor that of a pure photonic mode. However, the presence of SPPs and the continuity of the displacement field lead to a strong enhancement of the normal electric field component inside the thin AlOx layer (note the red arrows, which denote the E-field polarization). Additionally, the dielectric discontinuity of the NW/AlOx interface produces polarization charges, which interact with the SPPs at the Au/AlOx interface and thus create a "capacitor-like", subwavelength energy storage in the small gap region [141].
We can also see, that the coupling between the higher order SPP2 mode with photonic modes can significantly change the mode profile for comparatively small wire diameters. This is exemplarily shown for the HE11_{x} mode at a diameter of $d = 190\,\text{nm}$ in Fig. 13.2 (b). The coupling leads to the same capacitive energy storage, now with the formation of two oppositely, normal (y-)polarized maxima within the gap region. The resulting, main polarization inside the nanowire region is still along the x-direction. For this mode, the coupling to the SPPs ceases with increasing wire diameter: As an example, at a diameter of $d = 400\,\text{nm}$, the HE11_{x} mode displays its purely photonic characteristic with the entire energy being stored inside the NW. The HSP2 and TE01 mode, on the other hand, still exhibit a strong plasmonic coupling, even at a comparatively large diameter of $d = 400\,\text{nm}$. It can be seen that modes with a high share of y-polarized field components couple much stronger to SPPs due to the congruence in mode symmetry with electric field components of the surface plasmons. The HSP2 mode shows similar features as the HSP1 mode, but a much larger cut-off diameter at $d \approx 200\,\text{nm}$ and much lower effective mode indices, indicative for the weaker optical confinement. This weaker confinement can directly be seen in the intensity distribution in Fig. 13.2 (b), as, in contrast to the HSP1 mode, a considerable amount of the HSP2 mode's electromagnetic energy propagates inside the NW, instead of being bound to the metal surface [168].
To gain a better understanding of the origin of the presented modes, we will further investigate the mode development in the photonic limit by increasing the AlOx spacer thickness in the next section.

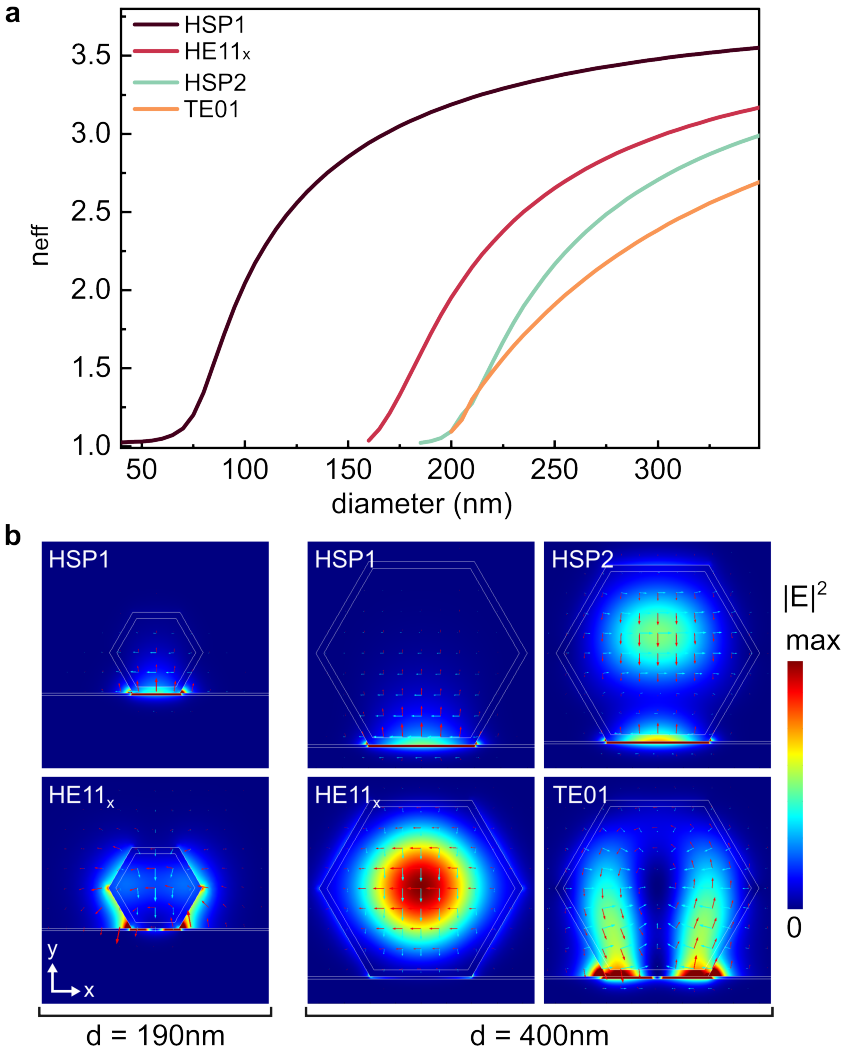

Figure 13.2: Waveguide modes emerging from the hybrid-plasmonic design with an integrated AlOx layer of $h = 5$ nm between the NW and the Au substrate. (a) Effective mode indices as a function of NW diameter for the first four modes. We identify two strongly coupled *hybridized surface plasmon* (HSP) modes, HSP1 (brown) and HSP2 (green). (b) Corresponding field profiles of the waveguide modes in (a) for two different diameters of $d = 190$ nm and $d = 400$ nm. The arrows mark the in-plane polarization of the E-field (red) and the H-field (blue). The color scale is not the same for different images.

13.1.3 Mode hybridization in the photonic limit

In order to understand the origin of the hybridized surface plasmon modes HSP1 and HSP2, we now analyze the mode dispersion in dependence of the dielectric spacer thickness h. The dispersion curves of the first four modes are shown in Fig. 13.3 for spacer thicknesses between $h = 5\,\text{nm}$ and $h = 200\,\text{nm}$.
While the dispersion curves of the $HE11_x$ and the TE01 mode stay nearly constant when the spacer thickness increases, the dispersion curves of the hybridized modes change significantly. Already at $h = 20\,\text{nm}$, the HSP1 and $HE11_x$ mode are almost degenerate at the highest diameter, while for small NW diameters the hybridization is apparent from the high effective index in the range of $d = 70 - 180\,\text{nm}$. Following the evolution of the HSP1 mode for continuously increasing spacer thicknesses, the mode dispersion progressively approaches that of the $HE11_x$ mode. At $h = 200\,\text{nm}$, the plasmonic coupling is entirely suppressed and the hybridized HSP1 mode fully converts to the photonic $HE11_y$ mode. The transition from the SPP-like to the photonic nature can be traced in the images $1 - 3$ at the right-hand side of Fig. 13.3. The images show the intensity distribution at $h = 50\,\text{nm}$ for the diameters (1) $d = 140\,\text{nm}$, (2) $d = 240\,\text{nm}$ and (3) $d = 340\,\text{nm}$ (also marked in the plot for $h = 50\,\text{nm}$). For the comparatively small NW diameter of (1) $d = 140\,\text{nm}$, the waveguide mode features a SPP-like behavior with the electric field intensity being stored within the gap region and strongly bound to the metal/dielectric interface. At the intermediate, 240 nm wire diameter, the energy is distributed over both the NW and the adjacent metal/dielectric interface. At the high NW diameter of $d = 340\,\text{nm}$, the mode is fully converted to the photonic $HE11_y$ mode.
A similar behavior can be observed for the higher order, HSP2 mode. With increasing AlOx layer thickness and hence decreasing plasmonic coupling, the HSP2 mode approaches more and more the photonic mode branch of the $HE21_y$ mode. At $h = 200\,\text{nm}$, the mode dispersion then fully resembles that of a NW lying on a dielectric SiO_2 substrate (cf. Sec. 10.3) with an effective mode index cut-off of $n_{\text{eff}} = n_{Al_2O_3} = 1.76$. Thus, we conclude, that the field generated by surface plasmons affects the photonic modes, which exhibit a dominant polarization normal to the metal surface (y-polarization), much stronger than the modes with dominant polarization parallel to the metal surface (x-polarization). This strong coupling with the SPP field then successively leads to a hybridization of the modes, which becomes stronger with a decreasing distance to the metal.

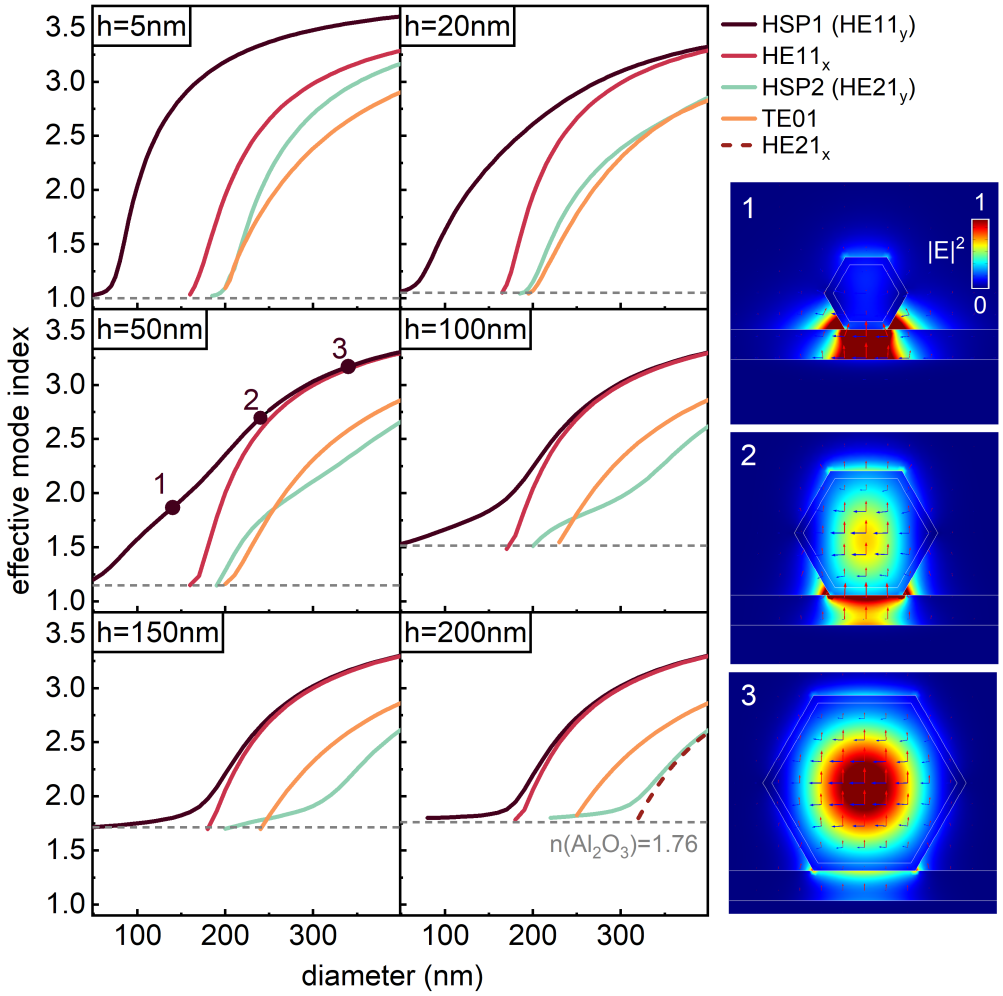

Figure 13.3: Mode dispersion of the hybrid-plasmonic waveguide design in the photonic limit. The effective indices of the first four waveguide modes are shown for different AlOx layer thicknesses between $h = 5\,\text{nm}$ and $h = 200\,\text{nm}$. With increasing spacer thickness, the HSP1 mode approaches the mode branch of the HE11_y mode, and the HSP2 mode that of the higher order HE21_y mode. The dispersion with the highest AlOx layer thickness ($h = 200\,\text{nm}$) resembles that of a NW lying on a dielectric SiO_2 substrate (see Sec. 10.3). The images on the right-hand side show the transition from the SPP-like HSP1 to the photonic-like HE11_y mode with increasing diameter. The positions from where the images were extracted are marked in the mode dispersion for $h = 50\,\text{nm}$. The color scale is equal for the images $1 - 3$.

13.2 Mode identification

We have just shown how new eigenmodes develop in the hybrid-plasmonic waveguide design. In the present section, we now systematically investigate the lasing behavior of NWs that are lying on a Au/AlOx substrate with $h = 5\,\text{nm}$. The applied evaluation method is similar to the one presented in Sec. 12.3.3 for NWs lying on a Au substrate. The dependence of the lasing capability on the NW morphology is presented in Fig. 13.4 (a). On this sample, we have examined over 70 NWs with respect to their ability to lase. After they were spectroscopically analyzed, their dimensions were determined via SEM. The diameters and the tip lengths of the measured NWs are plotted in Fig. 13.4 (a). Again, we distinguish between nanowires that showed a proper lasing behavior, plotted as turquoise spheres, and those, which did not show lasing, but at most FP resonances (black squares). We observe a similar trend as for the NWs lying on gold: Only above a diameter of $d = 197\,\text{nm}$, NWs with lasing capability are found. Additionally, Fig. 13.4 (a) reveals that a pronounced and long tip is obstructive for lasing, as no lasing was observed in nanowires with a tip longer than 1.1 µm. This can be explained by a strong reduction in end facet reflectivity due to the pronounced tapering (cf. Sec. 11.2). We therefore exclude the HSP1 mode to be the dominant lasing mode in these nanowires for two reasons: The minimum diameter of $d = 197\,\text{nm}$ suggests that the amplified mode has a mode cut-off diameter at this point. This is not the case for the HSP1 mode, which has a mode cut-off at $d \approx 75\,\text{nm}$. Secondly, we presume that the tip formation should not have a great influence on the lasing performance of the HSP1 mode, as most of the mode's energy propagates within the AlOx layer. Hence, as the wave does not directly impinge on the end facet, the tip shape should not significantly reduce the reflectance and thus not have a great influence on the cavity quality.
We further confirm our assumptions by comparing the experimentally determined group indices with the simulated values in Fig. 13.4 (b). The procedure of the group index calculation is the same as described in Sec. 12.3.3. The measured NWs exhibit group indices between $n_g = 6.3$ and $n_g = 7.2$, which strongly deviate from the simulated values of the hybrid-plasmonic HSP1 mode. Above a NW diameter of $d = 150\,\text{nm}$, the group index of the HSP1 mode stays almost constant at a comparatively low value of around $n_g = 3.6$. Compared to the HSP1 mode, the simulated group indices for the $HE11_x$ and HSP2 mode are very high in the diameter range of $d = 180 - 250\,\text{nm}$ and coincide very well with the experimentally determined values of the measured nanowires. Concerning the emission polarization, the investigated lasing wires showed a similar behavior to the one presented in Fig. 12.2 (c) and (d), namely a dominant linear polarization perpendicular to the nanowire axis (not shown here). This lets us assume that the photonic $HE11_x$ is the dominant lasing mode. Note, that not all of the measured wires shown in Fig. 13.4 (b) were able to lase, but exhibited at least FP resonances, which allowed us to determine the mode spacing $\Delta\lambda$. The differences between the experimentally and theoretically evaluated group indices may be due to a slight refractive index deviation between the deposited, poly-crystalline AlOx layer and the literature value of a mono-crystalline Al_2O_3 material, which was assumed in the simulations.

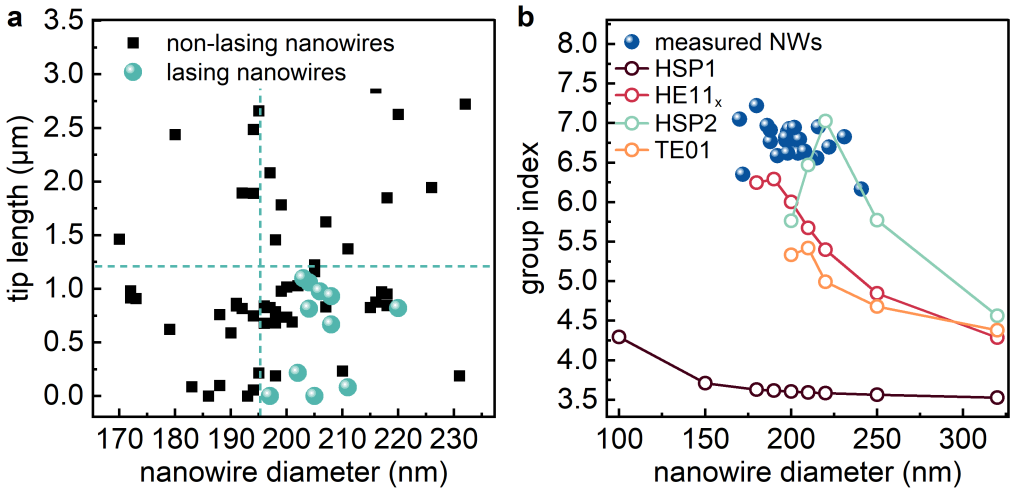

Figure 13.4: Mode identification of NWs lying on an Au/AlOx substrate with $h = 5$ nm. (a) Statistic of the measured nanowires: The total diameter is plotted against the tip length. No lasing was observed in nanowires with $d < 197$ nm and tip lengths exceeding 1.1 µm. (b) Experimentally determined group indices of the measured nanowires, which showed at least FP resonances, compared with the group indices of the first four modes, determined by the numerical simulations. The group indices of the measured wires are in good agreement with the $HE11_x$ and the HSP2 mode.

13.3 Threshold characteristics

We now study the influence of the dielectric spacer thickness on the lasing performance. To this end, we have analyzed several nanowires regarding their lasing threshold on the substrates with different AlOx spacer thicknesses of $h = 0, 5, 7, 10, 15$ and 20 nm. The investigated wires are measured under similar conditions: They were excited with a 690 nm laser under pulsed operation. The exciting laser was focused onto the wires through a 20× objective (NA = 0.45) and the laser repetition frequency was set between 10 − 80 MHz. Note that, as we represent the excitation pump power in energy density per pump pulse ($\mu J/cm^2$), the repetition rate does not influence the threshold determination. Furthermore, at least three orders of magnitude of the carrier density decays within the first 10 ns after excitation, which is still below the time between two excitation pulses of 12.5 ns at the highest repetition frequency of 80 MHz. We can therefore assume that the the system is restored to equilibrium before the subsequent pump pulse arrives.
The results of this study are summarized in Fig. 13.5 (a): Each sphere represents the determined threshold value of one lasing nanowire on the respective substrate (x-axis) and the orange circles indicate the average threshold value among all nanowires on the respective substrate. Though the threshold values scatter up to $\pm 100\,\mu J/cm^2$ within one substrate, which is due to the differences in NW morphology, a clear trend can be observed: The nanowires directly lying on the gold surface ($h = 0$ nm) exhibit the highest average threshold. The threshold is then significantly reduced for the nanowires on the substrates with a thin AlOx spacer of 5 and 7 nm, respectively. The lowest absolute lasing threshold value amounts to $p_{th} = 76\,\mu J/cm^2$ on the substrate with $h = 5$ nm. This trend reverses for increasing spacer thicknesses, for which we observe a higher average lasing threshold again.
We further compare the input-output characteristic of representative lasing nanowires from the different devices in Fig. 13.5 (b). In order to get comparable results, we took the data from the wires with lowest threshold from the devices with $h = 0$ nm, $h = 7$ nm, $h = 15$ nm and $h = 20$ nm. The samples $h = 5$ nm and $h = 10$ nm are omitted, because for the particular wires, not enough data points around the lasing threshold were recorded. The output intensity of each curve in (b) was normalized to the intensity at p_{th}, such that $I(p_{th}) = 1$, and the threshold pump power for each laser is marked by the dashed line in the respective color. The nanowires for which we compare the I-O characteristics are furthermore encircled in Fig. 13.5 (a). The reduction in lasing threshold obviously leads to an increase in the spontaneous emission factor β, which can be seen by the differences in the "S"-shape of the curves in (b). This becomes evident when comparing the curves with comparatively high threshold, as for $h = 0$ nm or $h = 20$ nm, with the I-O curves of the lasers with lower threshold ($h = 15$ nm and $h = 7$ nm). The "S"-shape continuously flattens with decreasing lasing threshold, which in turn indicates a higher β-factor (cf. Sec. 10.5). Hence, in our samples, the reduction in lasing threshold is directly correlated to a higher β-factor. Vice versa, we here demonstrate for our core/shell wires, that an increase of the β-factor is achieved when integrating a sufficiently thin, low-index dielectric spacer between the NW and the metal substrate.

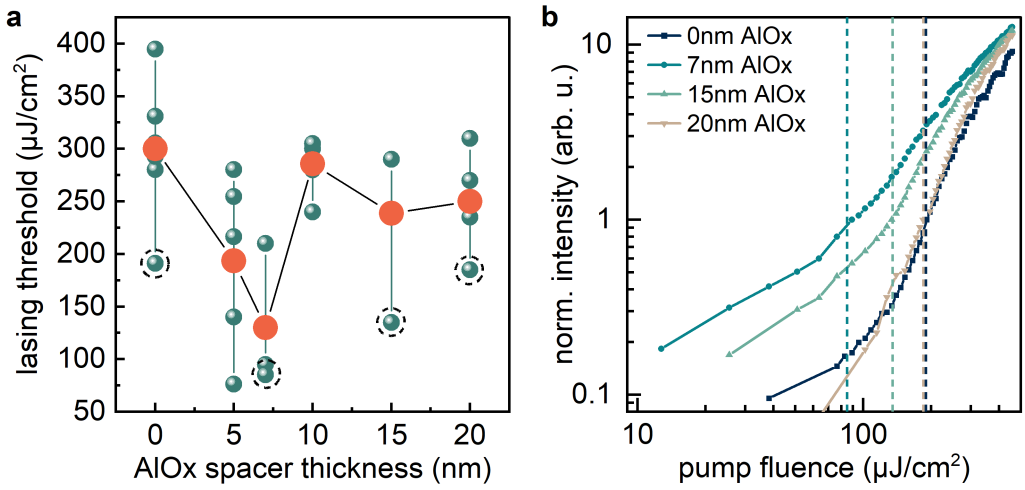

Figure 13.5: Threshold characteristics of lasing nanowires on substrates with different AlOx spacer thicknesses. (a) Summary of threshold values determined from several nanowires on each sample. Each green sphere represents one nanowire laser and the orange circles indicate the calculated average threshold from all nanowires on the respective substrate. (b) I-O characteristic of some representative lasing nanowires from the different devices. The nanowires to which the curves belong are encircled in (a).

13.4 Conclusion

In this chapter, we have tested the concept of the hybrid-plasmonic waveguide design based on the integration of a nanometer-scale, low-index dielectric layer between the metal substrate and the nanowire. Experimentally, this concept was realized by applying a thin AlOx layer onto the MBE-grown GaAs/Au substrate. Our numerical eigenmode analysis predicted two new eigenmodes that substantially differ from purely photonic or purely plasmonic modes. As these states are a result of mode hybridization, we refer to them as *hybridized surface plasmon* mode, HSP1 and HSP2. We have furthermore demonstrated that these modes convert to the photonic $HE11_y$ and $HE21_y$ modes in the photonic limit, when increasing the thickness of the dielectric: We have shown this by numerically simulating the diameter-dependent mode dispersion for various AlOx spacer thicknesses from $h = 5\,\text{nm}$ up to $h = 200\,\text{nm}$. This leads us to the assumption that the y-polarized modes exhibit a much stronger coupling to SPP-fields due to the correlation in mode symmetry.

Despite the predicted, simultaneous existence of these strongly coupled, hybridized waveguide modes on substrates with thin dielectric spacer, we identified the $HE11_x$ mode, having mainly photonic character, to be the dominant mode of the observed lasing. This is similar to what was determined for the nanowires in direct contact with the gold substrate ($h = 0\,\text{nm}$) in the previous chapter (Ch. 12). Concerning the lasing performance of the $HE11_x$ mode, our tested, hybrid-plasmonic devices are attractive when the dielectric

spacer is very thin: We observe a measurable reduction in average lasing threshold from the nanowires on a substrate with 5 nm and 7 nm AlOx spacer as compared to the NWs that are in direct contact with the gold surface. The threshold then increases again with increasing spacer thickness. An attempt to interpret the presented results by summarizing and comparing all of our findings from Chs. 11 to 13 is given in the following chapter.

14

Nanowire waveguides and lasers on various substrates - summary and analysis

We now conclude the insights on the lasing behavior of our nanowires, gained from the previous chapters, and summarize the results of this part.
In Ch. 11, we investigated wurtzite GaAs nanowires with diameters of $d = 200(\pm 30)$ nm, lying on a dielectric SiO_2 substrate, regarding their lasing capability. We were able to drive some of these NWs into the ASE regime as they featured distinct FP resonances in their emission spectrum under high excitation intensity. However, no lasing behavior was observed from nanowires on a SiO_2 substrate. By contrast, a clear lasing behavior was observed from the same nanowires when they are deposited onto a Au or Au/AlOx substrate (Chs. 12 and 13). A statistical evaluation on the nanowire geometry furthermore revealed, that a minimum diameter of $d = 200$ nm is necessary for our GaAs core/shell wires to achieve lasing. We thereby find the lasing performance to be strongly dependent on the nanowire morphology. In particular, we found the shape of the end facet to constitute a major practical challenge, as a long conical tip, which - up to a certain length - can not be avoided in core/shell NW MBE, severely reduces the cavity quality.
To identify the dominant lasing mode, we evaluated the group indices and analyzed the polarization of the nanowire emission. We thereby found the photonic-like $HE11_x$ mode to be the dominant transverse mode in all our investigated lasing nanowires, both on Au and Au/AlOx. This is in line with numerical simulations, which predict a mode cut-off diameter of $d \approx 200$ nm for the HE11 mode in all our investigated structures. We did not observe lasing from the newly forming optical modes, resulting from strong coupling to surface plasmons, neither from the SPP modes on the Au substrate, nor from the HSP modes on the Au/AlOx substrate. These modes are predicted to dominate lasing at wire diameters below 200 nm. A technical reason for the absence of observation of lasing might be that the excitation lasers available in this thesis do not provide sufficient power to stimulate these new modes in the narrowest NWs. This could be tested in the future with higher power lasers. Nevertheless, concerning the photonic modes, such as the $HE11_x$, it is noteworthy that the presence of a metal substrate is apparently a necessary condition to

attain lasing in our GaAs nanowires.
In literature, there are many examples of single NW-based photonic lasers [18, 139, 169–177], based on various semiconductor materials, operating in the visible to the IR range. None of these reports, however, studies the impact of the NW environment, or substrate, respectively, on the lasing performance and the threshold. On the other hand, all reports about plasmonic [20, 178, 179] and hybrid-plasmonic lasers [124, 127, 158, 180–182], so far only focus on the possibility subwavelength waveguiding and lasing of optical modes, which are strongly coupled to surface plasmons (SPP1, SPP2 or HSP1), by using NWs with diameters below the photonic mode cut-off. For the first time, we compare GaAs/AlGaAs NWs with diameters close to the photonic mode cut-off within these three different waveguide designs with respect to the lasing performance. Indeed, we have found the photonic $HE11_x$ mode to be the dominant one that is amplified in all structures. What has also not yet been discussed: At diameters close to the mode cut-off, the coupling to surface plasmons also modifies the $HE11_x$ mode, which is particularly well demonstrated by the simulated electric field distribution in Figs. 12.2 and 13.2. Hence, we also observe decisive differences in the lasing behavior between the nanowires on a Au and those on a Au/AlOx substrate: The integration of a thin dielectric AlOx layer allows to reduce the lasing threshold of the photonic-like $HE11_x$ mode, which we have experimentally shown in Sec. 13.3.
We now want to confirm these findings by comparing the different waveguide designs with respect to their modal threshold gain α_p/Γ, determined from our numerical simulations, in Fig. 14.1. Panel (a) displays the calculated values in the case of a NW lying on a Au substrate and panel (b) the same analysis in the case of a NW on a Au/AlOx substrate with $h = 7\,\text{nm}$, for which we determined the lowest average threshold (Sec. 13.3). The diameter range of the nanowires investigated in Chs. 11, 12 and 13 is shaded in gray. For comparison, the threshold of the fundamental HE11 mode of a NW placed on SiO_2 is plotted as dashed line in both graphs. The threshold calculation of the structure with the 7 nm thin AlOx spacer (Fig. 14.1 (b)) reveals some intriguing results: Over the entire diameter range, the modal threshold values of the hybridized modes (HSP1 and HSP2) are indeed lower than those of the purely plasmonic SPP modes in (a). This is in line with the observations in various reports on hybrid-plasmonic waveguides and lasers [124, 127, 158, 180–182]. Secondly, the modal threshold for the HSP1 mode (Fig. 14.1 (b)), below the photonic mode cut-off, is clearly higher than for the $HE11_x$ mode, which supports our hypothesis that stronger excitation is required to induce lasing in NWs with $d < 200\,\text{nm}$. The most striking result to emerge from Fig. 14.1 (b), however, is the low threshold of the $HE11_x$ mode on the Au/AlOx substrate, which is similar to the purely photonic case (HE11 mode on SiO_2), and therefore lower than the threshold of the $HE11_x$ mode on a pure Au substrate (Fig. 14.1 (a)). This approves our experimental observation of threshold reduction of NW lasers when a thin, dielectric AlOx spacer is integrated between the NW and the gold substrate, even for the photonic-like $HE11_x$ mode.
Our analysis also leaves some open questions: In the investigated diameter range, Fig. 14.1 predicts the modal threshold of the HE11 mode on SiO_2 to be as low as of the $HE11_x$ mode on the Au/AlOx substrate with 7 nm spacer. The lasing threshold for nanowires

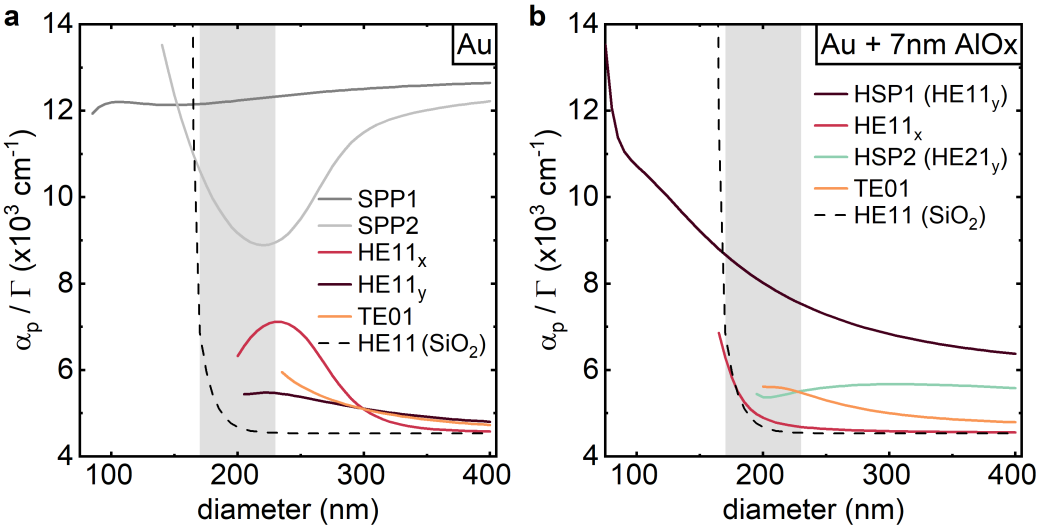

Figure 14.1: Comparison of the modal threshold between the plasmonic and hybrid-plasmonic waveguide design. (a) Modal lasing threshold as a function of nanowire diameter for the first five waveguiding modes in a nanowire lying on an Au substrate (also shown in Fig. 12.7 (c)). (b) Same graph as in (a) for the first four modes of the hybrid-plasmonic waveguide design (NW on Au + 7 nm AlOx spacer). As stated in literature [124, 127, 158, 180–182], the HSP modes exhibit a lower threshold than the SPP modes as a result of reduced plasmonic damping. More intriguingly, also the threshold of the $HE11_x$ mode is reduced in the structure with a 7 nm thin AlOx spacer and is comparable to the purely photonic case (dashed curves in (a) and (b)). This underlines our experimental results of threshold reduction in the hybrid-plasmonic design.

on SiO_2 should therefore be lower than for the nanowires on a bare Au substrate. In our experiments, however, we could not drive the nanowires on SiO_2 into the lasing regime, while this was indeed possible on the Au substrate and even more efficient with an integrated, thin AlOx layer. At this point, it should be mentioned, that the numerical simulations presented in this thesis are solely based on Maxwell's equations, which only include the dielectric constants of the materials. Any effects on excited charge carriers or carrier dynamics inside the GaAs nanowires are not included. In Sec. 12.5, we discussed some possible reasons why lasing on a metallic Au substrate might be more efficient than on a dielectric SiO_2 substrate.

In summary, we have shown that the hybrid-plasmonic waveguide design indeed combines the "best of both worlds" [166]. Not only concerning the possibility of subwavelength confinement to newly plasmonic modes, but also in terms of the lasing performance of dominant photonic modes. Hence, a Au substrate covered with a thin dielectric AlOx spacer of $5 - 7$ nm is very promising for future studies on single-wire lasing.

15

Final conclusion and outlook

In this thesis, we have studied single, direct-bandgap GaAs nanowires under various aspects. The unique ability to synthesize nanowires in the meta-stable wurtzite crystal phase, combined with their dielectrically peculiar, elongated shape, has led us to focus on two main areas: On the one hand, the tunability of the core diameter and the shell thickness in our advanced MBE growth process offers a unique access to spectroscopy in the 1D quantum regime in semiconductors. Our combined spectral-, polarization- and time-resolved experiments complement previous studies on the band alignment and the peculiar optical properties of wurtzite GaAs. Secondly, we have exploited the inherent dual functionality of semiconductor nanowires to simultaneously act as both, optical gain medium and photonic cavity. Inspired by previous studies on plasmonic and hybridized plasmonic waveguides and lasers, we have investigated our own material system, based on GaAs/AlGaAs core/shell nanowires, with respect to their lasing behavior in different waveguide designs.
In particular, photoluminescence studies on semiconductor nanowires always involve the subtle interplay between electronic and dielectric properties. As such, both parts of this work require a detailed study of the light-matter interaction between the emitting material and the photonic effects inherent to semiconducting nanostructures, which are strongly dependent on the wire dimensions. We provide the essential tools for understanding the physics and operation of our GaAs nanowires acting as nanophotonic structures. Keeping this in mind, we will now summarize the essential results of this work:

In part II, we focused on the 1D physical properties of phase-pure wurtzite GaAs/AlGaAs core/shell quantum wires. A thorough analysis of the excitation power dependency demonstrated that our ultrathin GaAs cores provide large confinement energies of up to several tens of meV, allowing us to resolve up to four subband transitions in the PL spectrum of a single wire for the first time. Furthermore, we experimentally elucidated the peculiar polarization selection rules of wurtzite wires in the 1D quantum regime. Similar to bulk wurtzite GaAs, dipole transitions including valence subbands with dominant hh character

are much stronger for polarizations perpendicular to the wire axis, while subbands with lh character do not favor a particular polarization. These polarization selection rules, as well as the $1/\sqrt{E}$ dependence of the joint density of states, characteristic for 1D quantum regimes, were consolidated by $\mathbf{k}\cdot\mathbf{p}$-based calculations, which were contributed to us by Dr. Paulo E. Faria Junior as part of our collaboration.
Motivated by these findings, we further experimentally disentangled the wurtzite quantum wire structure through a polarization-resolved analysis. The key finding was that the polarization behavior of our wurtzite quantum wire is not only dependent on the internal electronic structure of the involved valence bands, but also significantly affected by external, photonic effects. We systematically studied the influence of these external photonic polarization anisotropies by varying the thickness of the AlGaAs shell around the ultrathin GaAs cores. This allowed us to modify the dielectric diameter and thus tune the photonic properties of our nanowires, while the ultrathin GaAs cores, exhibiting strong spatial quantum confinement, were still maintained. Together with numerical FEM simulations, we demonstrated that the electronic polarization selection rules in wires with dielectrically thin diameters are superimposed by the dielectric mismatch effect. This photonic effect strongly suppresses light with perpendicular polarization inside wires with dielectric diameters below $d = 200\,\text{nm}$, and thus selectively reduces the probability of hh transitions. In quantum wires with larger diameter than 200 nm, purely electronic polarization selection rules, which are predicted by the band structure, can be observed. In this diameter range, the emission into optical waveguide modes has to be taken into account at the same time.

A detailed study on optical waveguiding and lasing was then conducted throughout part III of this thesis. The investigated core/shell nanowires have comparatively thick core diameters of around $d = 200\,\text{nm}$ and are passivated with only a thin AlGaAs shell of nominally 15 nm. Hence, the cores do not exhibit size quantization effects, but the large core diameter provides sufficient gain to amplify light inside the nanowire resonator: The emitted light is guided along the wire axis and reflected at the end facets, which enables the single nanowire to act as standalone Fabry-Pérot type cavity.
On SiO_2, stimulated emission was observed through the emergence of FP resonances in the emission spectrum of these nanowires. However, none of the investigated wires could be driven into the lasing regime with the provided optical power of our excitation laser. Hence, we shifted our perspective towards metallic substrates, with the objective to explore possible coupling of our nanowires to the surface plasmon polaritons of a metal surface. Intriguingly, the same nanowires are capable of lasing when they are deposited onto a Au substrate with atomically flat surface. To further explore the role that plasmonic coupling plays in connection with lasing nanowires, we investigated the hybridized plasmonic waveguide design by placing our GaAs nanowires onto a Au substrate coated with thin dielectric AlOx layers. By varying the spacer thickness between the nanowires and the gold surface, we found a significant reduction in lasing threshold when the AlOx layer is sufficiently thin of $5 - 7\,\text{nm}$. At the same time, the lasing performance of the wires on the Au/AlOx substrates is thereby strongly dependent on the nanowire

morphology, i.e. the shape of the end facet and the total wire diameter. No lasing could be achieved in nanowires, which exhibited a long conical tip or a total diameter smaller than $d = 200\,\text{nm}$.
Together with a comprehensive experimental study, we use numerical FEM simulations to identify the transverse waveguide modes inside each of the structures. Despite the presence of plasmonic modes in the investigated diameter range, the photonic-like $HE11_x$ mode was found to be the dominant lasing mode. However, we were able to show that even waveguide modes with dominant photonic character are modified through the coupling to surface plasmons. In this sense, the integration of a thin dielectric spacer between the lasing nanowires and the metal substrate could reduce ohmic losses - also for the photonic-like $HE11_x$ mode - and therefore lower the lasing threshold of our GaAs wires.
While commonly being eminent through the ability of subwavelength confinement, we have shown that the hybridized waveguide design is very promising with respect to the lasing efficiency in general. We found the lowest threshold for the photonic-like $HE11_x$ mode on a Au substrate with a 7 nm thin AlOx spacer.
No lasing emission was observed that emerges from purely plasmonic, or hybridized plasmonic modes.

At the end of this thesis, by combining both parts of this work, the way is paved for the development and realization of quantum wire lasers in GaAs. Such lasers are predicted to have the maximum allowable performance and operate under extremely low excitation, a property that has, to the best of our knowledge, never been reported in bottom-up fabricated single GaAs quantum wires. Through their larger density of states at the bottom of the subbands, quantum wire lasers exhibit larger differential gain than compared to bulk or quantum well lasers [183–185]. This can result in a significant reduction of the lasing threshold, making them promising candidates to outperform existing nanolaser structures.
Our results provide insights into the design of such lasers, including the optimization of the overlap between the targeted electronic subband transition and the photonic cavity mode. We have already proven the one-dimensional quantum nature of our wurtzite GaAs wires and furthermore demonstrated how to optimize the waveguide design with respect to the lasing efficiency. So far, optical waveguiding in bottom-up fabricated quantum wires has not been addressed, as their diameters commonly fall below the mode cut-off. However, we were able to show that a dielectric diameter suitable for optical waveguiding can be achieved by radially overgrowing the GaAs quantum wire cores with a thick AlGaAs shell, while the 1D size quantization effects are still maintained.
Admittedly we have not observed lasing from our dielectrically thick quantum wires so far. We believe, that the major obstacle thereby is the undesirable conical tip of the NW top facet, the formation of which we observe during shell growth. As the pronounced tapering significantly reduces the reflectivity, we believe that quality of the quantum wire cavity is not yet sufficient to create positive optical feedback. In Sec. 3.3.3, we have already established the starting point for future studies on the synthesis of quantum wire waveguides without this tip formation.

Overall, the technical capabilities and deep understanding of the optical properties of wurtzite quantum wires and nanolasers developed throughout this work provide an ideal and solid basis for future investigations in the field of nanophotonics. Furthermore, we are closing in on establishing the full potential of quantum wire lasers.

Appendix

A

Spectroscopy on quantum wires

A.1 Effects of high excitation - pulsed and cw

In Sec. 6.1, we discuss the subband filling of our GaAs quantum wires under high excitation. The investigated quantum wires are excited with a pulsed laser light. Here, we want to show the difference of the subband PL spectra when the wires are excited under cw mode. Fig. A.1 (a) and (b) show the power series of a representative quantum wire with a core diameter of approximately 30 nm and a total, dielectric diameter of $d = 230$ nm. In panel (a), the wire is excited with 1.8 eV laser pulses and 40 MHz repetition frequency. The spectrum exhibits three distinct subband transition peaks, which do barely shift in energy with increasing excitation intensity.
When the same quantum wire is excited with the same laser diode in cw mode, a significant shift of the subband peaks to lower energies is observed. From the lowest to the highest excitation power, the ground state peak shifts over a 100 meV from $E = 1.532$ eV to $E = 1.482$ eV. Additionally, the line width broadening of each individual peak is much more pronounced than in the power series under pulsed excitation in panel (a).
We attribute these difference to two main effects: Under cw excitation, the carrier density is constantly kept high, which promotes many-body interactions that induce bandgap renormalization and hence a red-shift of the PL spectrum [186, 187]. Secondly, phonon emission due to carrier relaxation may increase the lattice temperature of the nanowire and thus reduce the bandgap energy. This effect is less pronounced under pulsed excitation, as optically induced heat can easily dissipate to the surrounding between the excitation pulses [161].

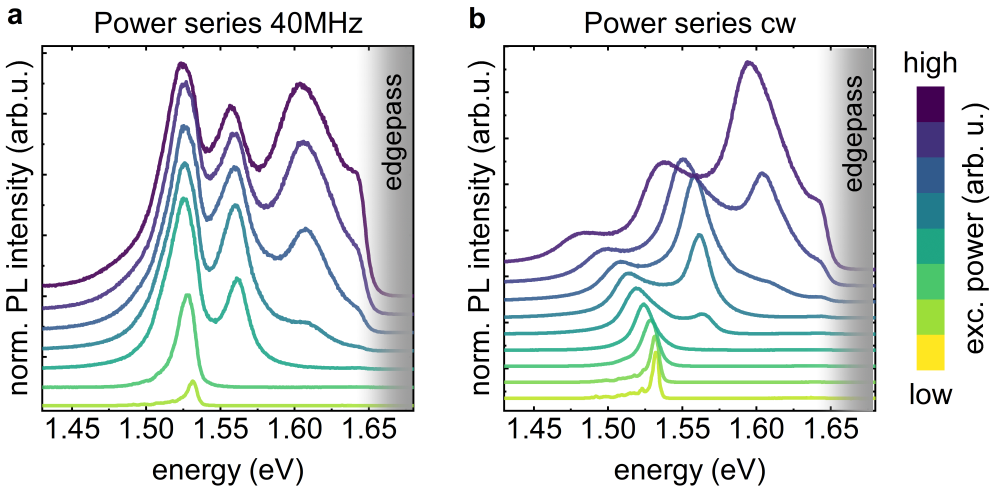

Figure A.1: Differences in quantum wire luminescence between pulsed and cw excitation. (a) Power series of a quantum wire PL spectrum, excited by a pulsed laser with an energy of 1.8 eV and 40 MHz repetition frequency. (b) Same wire excited with the same laser diode, operating in cw mode. The gray shaded area indicates the range above which the spectrum is blocked by an optical edgepass filter.

A.2 Electric field evaluation from numerical simulations

Numerical methods offer possibilities where classical, theoretical analyses come to the limits of their capabilities. One advantage is, once the simulation has run, one can easily integrate a resulting value over the desired surface or area.
We want to demonstrate this by the example shown in Fig. A.2. The simulations are conducted in the same way as described in Sec. 7.2. For simplicity, the nanowire exhibits a cylindrical cross section and the substrate is omitted, so that the wire is solely surrounded by air. In Fig. A.2 (a) the diameter dependent electric fields, $|E_\perp|$ and $\left|E_\parallel\right|$, in the center-point of the nanowire (point evaluation) are plotted as a function of unit free $n^* d/\lambda$, where $\lambda = 800\,\text{nm}$ is the wavelength at which the simulation is conducted. While for $n^* d/\lambda < 1$, $|E_\perp|$ and $\left|E_\parallel\right|$ strongly deviate from each other, they assimilate at larger values and oscillate around 1. These results are similar to the theoretical model proposed by Ruda *et al.* [108], who calculated the polarization anisotropies of the NW luminescence by considering an effective dipole in the center of the NW. In reality, however, luminescence occurs throughout the whole NW volume, which requires an integration over the entire cross-section and can only be performed numerically.
When the electric field values $|E_\perp|$ and $\left|E_\parallel\right|$ are integrated over the entire cross-section in our simulation, the results are significantly different, as can be seen in Fig. A.2 (b). The resulting, diameter dependent values still feature strong oscillations, but with a higher

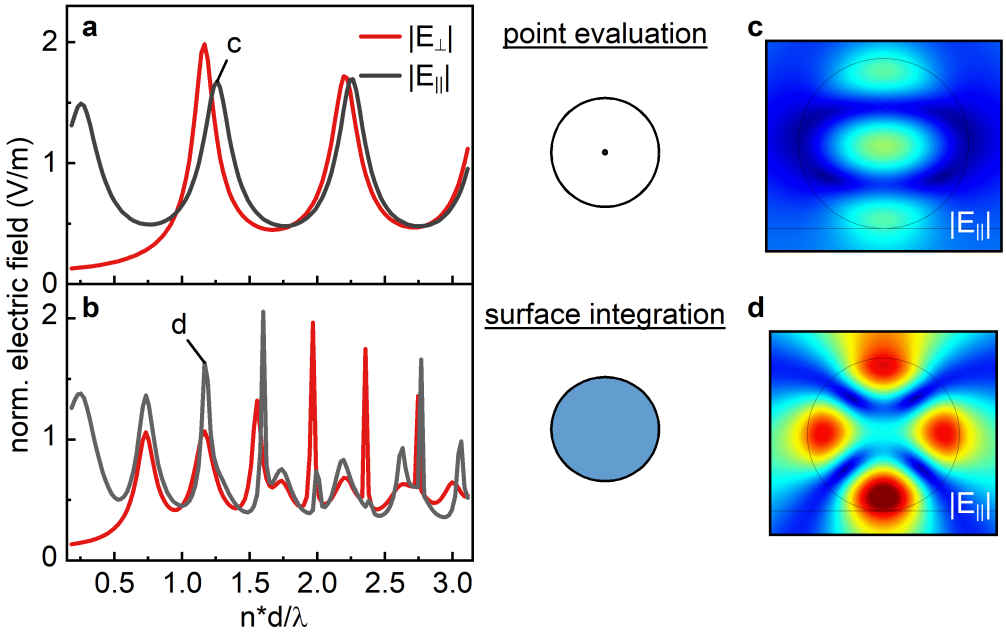

Figure A.2: Electric field determination from numerical FEM simulations. (a) $|E_\perp|$ and $|E_\parallel|$ as a function of n^*d/λ determined by point evaluation at the nanowire center. (b) Corresponding curves when the electric field is determined by surface integration over the entire nanowire cross section. (c) Example of $|E_\parallel|$ at the resonance $n^*d/\lambda = 1.26$, labelled in (a), with field maximum in the nanowire center. (d) Exemplary resonance of $|E_\parallel|$ at $n^*d/\lambda = 1.17$ with field minimum in the nanowire center, labelled in (b).

frequency than the electric field values in the center of the NW, shown in panel (a). The peaks in both graphs arise from field enhancements when the incident light is reflected at the NW/air boundary. At certain diameters, the reflection causes constructive interference and thus leads to resonance phenomena. These resonances appear more frequently in the evaluation shown in (b) than in the one shown in panel (a). The reason for this will now be explained with the help of Figs. A.2 (c) and (d), showing the field distribution of $|E_\parallel|$ around the nanowire at the values marked in panels (a) and (b). While the point evaluation in (a) only "detects" resonances that exhibit a field maximum in the nanowire center, like the one shown in panel (c), all appearing resonances inside the NW are identified when the field is integrated over the entire cross-section. An exemplary resonance, with a field *minimum* in the center, is shown in Fig. A.2 (d). The shown field distribution would not result in a peak of $|E_\parallel|$, when their values were taken only from the NW center. Hence, the evaluation method of surface integration comprises more information than the point evaluation. In conclusion, due to the possibility of surface integration, numerical methods can have advantages over analytical approaches and lead to more precise results.

Bibliography

[1] T. Giamarchi and O. U. Press, *Quantum Physics in One Dimension*, International Series of Monographs on Physics (Clarendon Press, 2004).

[2] B. J. van Wees, H. van Houten, C. W. J. Beenakker, J. G. Williamson, L. P. Kouwenhoven, D. van der Marel, and C. T. Foxon, *Quantized conductance of point contacts in a two-dimensional electron gas*, Physical Review Letters **60**, 848 (1988).

[3] A. Girdhar, V. Ashokan, N. D. Drummond, K. Morawetz, and K. N. Pathak, *Electron correlation and confinement effects in quasi-one-dimensional quantum wires at high density*, Physical Review B **105**, 115140 (2022).

[4] J. D. Sau, S. Tewari, R. M. Lutchyn, T. D. Stanescu, and S. Das Sarma, *Non-Abelian quantum order in spin-orbit-coupled semiconductors: Search for topological Majorana particles in solid-state systems*, Physical Review B **82**, 214509 (2010).

[5] Y. Sato *et al.*, *Strong electron-electron interactions of a Tomonaga-Luttinger liquid observed in InAs quantum wires*, Physical Review B **99**, 155304 (2019).

[6] V. V. Deshpande, M. Bockrath, L. I. Glazman, and A. Yacoby, *Electron liquids and solids in one dimension*, Nature **464**, 209 (2010).

[7] F. Qian, S. Gradečak, Y. Li, C.-Y. Wen, and C. M. Lieber, *Core/Multishell Nanowire Heterostructures as Multicolor, High-Efficiency Light-Emitting Diodes*, Nano Letters **5**, 2287 (2005).

[8] P. Krogstrup, H. I. Jørgensen, M. Heiss, O. Demichel, J. V. Holm, M. Aagesen, J. Nygard, and A. Fontcuberta i Morral, *Single-nanowire solar cells beyond the Shockley–Queisser limit*, Nature Photonics **7**, 306 (2013).

[9] G. Koblmüller, B. Mayer, T. Stettner, G. Abstreiter, and J. J. Finley, *GaAs–AlGaAs core–shell nanowire lasers on silicon: invited review*, Semiconductor Science and Technology **32**, 053001 (2017).

[10] E. M. Purcell, H. C. Torrey, and R. V. Pound, *Resonance Absorption by Nuclear Magnetic Moments in a Solid*, Physical Review **69**, 37 (1946).

[11] J. Bleuse, J. Claudon, M. Creasey, N. S. Malik, J.-M. Gérard, I. Maksymov, J.-P. Hugonin, and P. Lalanne, *Inhibition, Enhancement, and Control of Spontaneous Emission in Photonic Nanowires*, Physical Review Letters **106**, 103601 (2011).

[12] F. Dirnberger *et al.*, *Tuning Spontaneous Emission through Waveguide Cavity Effects in Semiconductor Nanowires*, Nano Letters **19**, 7287 (2019).

[13] B. Loitsch *et al.*, *Tunable Quantum Confinement in Ultrathin, Optically Active Semiconductor Nanowires Via Reverse-Reaction Growth*, Advanced Materials **27**, 2195 (2015).

[14] N. Vainorius, S. Lehmann, A. Gustafsson, L. Samuelson, K. A. Dick, and M.-E. Pistol, *Wurtzite GaAs Quantum Wires: One-Dimensional Subband Formation*, Nano Letters **16**, 2774 (2016).

[15] P. Corfdir *et al.*, *Crystal-Phase Quantum Wires: One-Dimensional Heterostructures with Atomically Flat Interfaces*, Nano Letters **18**, 247 (2018).

[16] F. Dirnberger *et al.*, *Ultralong spin lifetimes in one-dimensional semiconductor nanowires*, Applied Physics Letters **114**, 202101 (2019).

[17] S. Meier, P. E. F. Junior, F. Haas, E.-S. Heller, F. Dirnberger, V. Zeller, T. Korn, J. Fabian, D. Bougeard, and C. Schüller, *Intersubband excitations in ultrathin core-shell nanowires in the one-dimensional quantum limit probed by resonant inelastic light scattering*, Physical Review B **104**, 235307 (2021).

[18] D. Saxena, S. Mokkapati, P. Parkinson, N. Jiang, Q. Gao, H. H. Tan, and C. Jagadish, *Optically pumped room-temperature GaAs nanowire lasers*, Nature Photonics **7**, 963 (2013).

[19] B. Mayer *et al.*, *Lasing from individual GaAs-AlGaAs core-shell nanowires up to room temperature*, Nature Communications **4**, 2931 (2013).

[20] J. Ho, J. Tatebayashi, S. Sergent, C. F. Fong, S. Iwamoto, and Y. Arakawa, *Low-Threshold near-Infrared GaAs-AlGaAs Core-Shell Nanowire Plasmon Laser*, ACS Photonics **2**, 165 (2015).

[21] E. Bermúdez-Ureña, G. Tutuncuoglu, J. Cuerda, C. L. C. Smith, J. Bravo-Abad, S. I. Bozhevolnyi, A. Fontcuberta i Morral, F. J. García-Vidal, and R. Quidant, *Plasmonic Waveguide-Integrated Nanowire Laser*, Nano Letters **17**, 747 (2017).

[22] M. Moewe, L. C. Chuang, S. Crankshaw, C. Chase, and C. Chang-Hasnain, *Atomically sharp catalyst-free wurtzite GaAs/AlGaAs nanoneedles grown on silicon*, Applied Physics Letters **93**, 023116 (2008).

[23] M. Heiss *et al.*, *Direct correlation of crystal structure and optical properties in wurtzite/zinc-blende GaAs nanowire heterostructures*, Physical Review B **83**, 045303 (2011).

[24] T. B. Hoang, A. F. Moses, H. L. Zhou, D. L. Dheeraj, B. O. Fimland, and H. Weman, *Observation of free exciton photoluminescence emission from single wurtzite GaAs nanowires*, Applied Physics Letters **94**, 133105 (2009).

[25] H. Zeng, X. Yu, H. A. Fonseka, G. Boras, P. Jurczak, T. Wang, A. M. Sanchez, and H. Liu, *Preferred growth direction of III–V nanowires on differently oriented Si substrates*, Nanotechnology **31**, 475708 (2020).

[26] K. A. Dick, P. Caroff, J. Bolinsson, M. E. Messing, J. Johansson, K. Deppert, L. R. Wallenberg, and L. Samuelson, *Control of III–V nanowire crystal structure by growth parameter tuning*, Semiconductor Science and Technology **25**, 024009 (2010).

[27] M. I. McMahon and R. J. Nelmes, *Observation of a Wurtzite Form of Gallium Arsenide*, Physical Review Letters **95**, 215505 (2005).

[28] A. De and C. E. Pryor, *Predicted band structures of III-V semiconductors in the wurtzite phase*, Physical Review B **81**, 155210 (2010).

[29] F. Bechstedt and A. Belabbes, *Structure, energetics, and electronic states of III-V compound polytypes*, Journal of Physics: Condensed Matter **25**, 273201 (2013).

[30] B. Ketterer, M. Heiss, E. Uccelli, J. Arbiol, and A. Fontcuberta i Morral, *Untangling the Electronic Band Structure of Wurtzite GaAs Nanowires by Resonant Raman Spectroscopy*, ACS Nano **5**, 7585 (2011).

[31] C. Wilhelm, A. Larrue, X. Dai, D. Migas, and C. Soci, *Anisotropic photonic properties of III–V nanowires in the zinc-blende and wurtzite phase*, Nanoscale **4**, 1446 (2012).

[32] J. L. Birman, *Polarization of Fluorescence in CdS and ZnS Single Crystals*, Physical Review Letters **2**, 157 (1959).

[33] J. L. Birman, *Some Selection Rules for Band-Band Transitions in Wurtzite Structure*, Physical Review **114**, 1490 (1959).

[34] P. Y. Yu and M. Cardona, *Fundamentals of Semiconductors*, Graduate Texts in Physics (Springer Berlin Heidelberg, 2010).

[35] M. Murayama and T. Nakayama, *Chemical trend of band offsets at wurtzite/zinc-blende heterocrystalline semiconductor interfaces*, Physical Review B **49**, 4710 (1994).

[36] G. Signorello, E. Lörtscher, P. Khomyakov, S. Karg, D. Dheeraj, B. Gotsmann, H. Weman, and H. Riel, *Inducing a direct-to-pseudodirect bandgap transition in wurtzite GaAs nanowires with uniaxial stress*, Nature Communications **5**, 3655 (2014).

[37] M. De Luca, S. Rubini, M. Felici, A. Meaney, P. C. M. Christianen, F. Martelli, and A. Polimeni, *Addressing the Fundamental Electronic Properties of Wurtzite GaAs Nanowires by High-Field Magneto-Photoluminescence Spectroscopy*, Nano Letters **17**, 6540 (2017).

[38] N. Vainorius, S. Kubitza, S. Lehmann, L. Samuelson, K. A. Dick, and M. E. Pistol, *Temperature dependent electronic band structure of wurtzite GaAs nanowires*, Nanoscale **10**, 1481 (2018).

[39] J. H. Davies, *The Physics of Low-dimensional Semiconductors* (Cambridge University Press, 1997).

[40] T. Mayer, *Epitaxial heterostructures of topological insulators: band engineering and electronic transport*, PhD thesis (Universität Regensburg, 2021).

[41] K. A. Dick, *A review of nanowire growth promoted by alloys and non-alloying elements with emphasis on Au-assisted III–V nanowires*, Progress in Crystal Growth and Characterization of Materials **54**, 138 (2008).

[42] P. L. Edwards and R. J. Happel, *Beryllium Oxide Whiskers and Platelets*, Journal of Applied Physics **33**, 943 (1962).

[43] R. S. Wagner and W. C. Ellis, *VAPOR-LIQUID-SOLID MECHANISM OF SINGLE CRYSTAL GROWTH*, Applied Physics Letters **4**, 89 (1964).

[44] V. G. Dubrovskii, N. V. Sibirev, J. C. Harmand, and F. Glas, *Growth kinetics and crystal structure of semiconductor nanowires*, Physical Review B **78**, 235301 (2008).

[45] V. G. Dubrovskii, G. E. Cirlin, I. P. Soshnikov, A. A. Tonkikh, N. V. Sibirev, Y. B. Samsonenko, and V. M. Ustinov, *Diffusion-induced growth of GaAs nanowhiskers during molecular beam epitaxy: Theory and experiment*, Physical Review B - Condensed Matter and Materials Physics **71**, 5 (2005).

[46] V. G. Dubrovskii, N. V. Sibirev, G. E. Cirlin, J. C. Harmand, and V. M. Ustinov, *Theoretical analysis of the vapor-liquid-solid mechanism of nanowire growth during molecular beam epitaxy*, Physical Review E **73**, 021603 (2006).

[47] V. G. Dubrovskii, *Influence of the group V element on the chemical potential and crystal structure of Au-catalyzed III-V nanowires*, Applied Physics Letters **104**, 053110 (2014).

[48] V. G. Dubrovskii and J. Grecenkov, *Zeldovich nucleation rate, self-consistency renormalization, and crystal phase of au-catalyzed gaas nanowires*, Crystal Growth and Design **15**, 340 (2015).

[49] F. Glas, J.-C. Harmand, and G. Patriarche, *Why Does Wurtzite Form in Nanowires of III-V Zinc Blende Semiconductors?*, Physical Review Letters **99**, 146101 (2007).

[50] F. Glas, J. C. Harmand, and G. Patriarche, *Nucleation antibunching in catalyst-assisted nanowire growth*, Physical Review Letters **104**, 2 (2010).

[51] J. Hubmann, *GaAs nanowires: Epitaxy, crystal structure-related properties and magnetic heterostructures*, PhD thesis (Universität Regensburg, 2015).

[52] A. Rudolph, *MBE growth of GaAs Nanowires and Nanowire Heterostructures*, PhD thesis (Universität Regensburg, 2010).

[53] F. Dirnberger, *New directions for semiconductor nanowires: Demonstrating robust spins and long-lived excitons*, PhD thesis (Universität Regensburg, 2019).

[54] S. Furthmeier, F. Dirnberger, J. Hubmann, B. Bauer, T. Korn, C. Schüller, J. Zweck, E. Reiger, and D. Bougeard, *Long exciton lifetimes in stacking-fault-free wurtzite GaAs nanowires*, Applied Physics Letters **105**, 222109 (2014).

[55] J.-C. Harmand, G. Patriarche, F. Glas, F. Panciera, I. Florea, J.-L. Maurice, L. Travers, and Y. Ollivier, *Atomic Step Flow on a Nanofacet*, Physical Review Letters **121**, 166101 (2018).

[56] D. Jacobsson, F. Panciera, J. Tersoff, M. C. Reuter, S. Lehmann, S. Hofmann, K. A. Dick, and F. M. Ross, *Interface dynamics and crystal phase switching in GaAs nanowires*, Nature **531**, 317 (2016).

[57] C. B. Maliakkal, "In Situ TEM Studies of III-V Nanowire Growth Mechanism", in *Nanowires - recent progress* (IntechOpen, 2021).

[58] J. Jakob, P. Schroth, L. Feigl, D. Hauck, U. Pietsch, and T. Baumbach, *Quantitative analysis of time-resolved RHEED during growth of vertical nanowires*, Nanoscale **12**, 5471 (2020).

[59] J. Jo, Y. Tchoe, G.-C. Yi, and M. Kim, *Real-Time Characterization Using in situ RHEED Transmission Mode and TEM for Investigation of the Growth Behaviour of Nanomaterials*, Scientific Reports **8**, 1694 (2018).

[60] J. Harmand, M. Tchernycheva, G. Patriarche, L. Travers, F. Glas, and G. Cirlin, *GaAs nanowires formed by Au-assisted molecular beam epitaxy: Effect of growth temperature*, Journal of Crystal Growth **301-302**, 853 (2007).

[61] J. C. Harmand, G. Patriarche, N. Péré-Laperne, M.-N. Mérat-Combes, L. Travers, and F. Glas, *Analysis of vapor-liquid-solid mechanism in Au-assisted GaAs nanowire growth*, Applied Physics Letters **87**, 203101 (2005).

[62] O. Demichel, M. Heiss, J. Bleuse, H. Mariette, and A. Fontcuberta i Morral, *Impact of surfaces on the optical properties of GaAs nanowires*, Applied Physics Letters **97**, 201907 (2010).

[63] C.-C. Chang *et al.*, *Electrical and Optical Characterization of Surface Passivation in GaAs Nanowires*, Nano Letters **12**, 4484 (2012).

[64] I. Pelant and J. Valenta, *Luminescence Spectroscopy of Semiconductors* (OUP Oxford, 2012).

[65] A. Einstein, *Zur Quantentheorie der Strahlung*, Physikalische Zeitschift **18**, 121 (1917).

[66] P. A. M. Dirac, *The quantum theory of the emission and absorption of radiation*, Proceedings of the Royal Society of London. Series A, Containing Papers of a Mathematical and Physical Character **114**, 243 (1927).

[67] P. W. Milonni, *Why spontaneous emission?*, American Journal of Physics **52**, 340 (1984).

[68] M. Pelton, *Modified spontaneous emission in nanophotonic structures*, Nature Photonics **9**, 427 (2015).

[69] M. Fox, *Quantum Optics: An Introduction*, Oxford Master Series in Physics Vol. 6 (OUP Oxford, 2006).

[70] V. Weisskopf, *Probleme der neueren Quantentheorie des Elektrons*, Die Naturwissenschaften **23**, 631 (1935).

[71] S. Noda, M. Fujita, and T. Asano, *Spontaneous-emission control by photonic crystals and nanocavities*, Nature Photonics **1**, 449 (2007).

[72] E. M. Purcell, "Spontaneous Emission Probabilities at Radio Frequencies", in (1995), p. 839.

[73] W. L. Barnes, S. A. R. Horsley, and W. L. Vos, *Classical antennas, quantum emitters, and densities of optical states*, Journal of Optics **22**, 073501 (2020).

[74] E. Yablonovitch, *Inhibited Spontaneous Emission in Solid-State Physics and Electronics*, Physical Review Letters **58**, 2059 (1987).

[75] S. John, *Strong localization of photons in certain disordered dielectric superlattices*, Physical Review Letters **58**, 2486 (1987).

[76] D. Englund, D. Fattal, E. Waks, G. Solomon, B. Zhang, T. Nakaoka, Y. Arakawa, Y. Yamamoto, and J. Vučković, *Controlling the Spontaneous Emission Rate of Single Quantum Dots in a Two-Dimensional Photonic Crystal*, Physical Review Letters **95**, 013904 (2005).

[77] D. Englund, A. Faraon, I. Fushman, N. Stoltz, P. Petroff, and J. Vučković, *Controlling cavity reflectivity with a single quantum dot*, Nature **450**, 857 (2007).

[78] M. D. Leistikow, *Controlling sponaneous emission with nanostructures*, PhD thesis (University of Twente, 2010).

[79] W. L. Barnes, *Fluorescence near interfaces: The role of photonic mode density*, Journal of Modern Optics **45**, 661 (1998).

[80] S. Noda, *Seeking the Ultimate Nanolaser*, Science **314**, 260 (2006).

[81] S. Ahmed, A. H. A. Clayton, T. Korte, A. Herrmann, R. Machán, M. Hof, G. Wright, and J.-B. Sibarita, *Practical Manual for Fluorescence Microscopy Techniques*, www.picoquant.com (2016).

[82] R. W. Robinett, *Quantum mechanics of the two-dimensional circular billiard plus baffle system and half-integral angular momentum*, European Journal of Physics **24**, 231 (2003).

[83] P. Harrison, *Quantum Wells, Wires and Dots* (John Wiley & Sons, Ltd, 2005).

[84] T. Cheiwchanchamnangij and W. R. L. Lambrecht, *Band structure parameters of wurtzite and zinc-blende GaAs under strain in the GW approximation*, Physical Review B **84**, 035203 (2011).

[85] P. Kusch, S. Breuer, M. Ramsteiner, L. Geelhaar, H. Riechert, and S. Reich, *Band gap of wurtzite GaAs: A resonant Raman study*, Physical Review B **86**, 075317 (2012).

[86] V. Zeller, N. Mundigl, P. E. Faria Junior, J. Fabian, C. Schüller, and D. Bougeard, *Wurtzite Quantum Wires with Strong Spatial Confinement: Polarization Anisotropies in Single-Wire Spectroscopy*, Physical Review Applied **18**, 054014 (2022).

[87] P. E. Faria Junior, T. Campos, and G. M. Sipahi, *Interband polarized absorption in InP polytypic superlattices*, Journal of Applied Physics **116**, 193501 (2014).

[88] P. E. Faria Junior, G. Xu, Y.-F. Chen, G. M. Sipahi, and I. Žutić, *Wurtzite spin lasers*, Physical Review B **95**, 115301 (2017).

[89] R. Cingolani, H. Lage, L. Tapfer, H. Kalt, D. Heitmann, and K. Ploog, *Quantum confined one-dimensional electron-hole plasma in semiconductor quantum wires*, Physical Review Letters **67**, 891 (1991).

[90] A. C. Maciel, J. F. Ryan, R. Rinaldi, R. Cingolani, M. Ferrara, U. Marti, D. Martin, F. Morier-Gemoud, and F. K. Reinhart, *Hot-carrier photoluminescence from GaAs V-groove quantum wires*, Semiconductor Science and Technology **9**, 893 (1994).

[91] P. Ils, A. Forchel, K. H. Wang, P. Pagnod-Rossiaux, and L. Goldstein, *Lateral subband transitions in the luminescence spectra of a one-dimensional electron-hole plasma in $In_{0.53}Ga_{0.47}As/InP$ quantum wires*, Physical Review B **50**, 11746 (1994).

[92] M. Yoshikawa, M. Kunzer, J. Wagner, H. Obloh, P. Schlotter, R. Schmidt, N. Herres, and U. Kaufmann, *Band-gap renormalization and band filling in Si-doped GaN films studied by photoluminescence spectroscopy*, Journal of Applied Physics **86**, 4400 (1999).

[93] W. R. Tribe, M. J. Steer, D. J. Mowbray, M. S. Skolnick, A. N. Forshaw, J. S. Roberts, G. Hill, M. A. Pate, C. R. Whitehouse, and G. M. Williams, *Emission mechanisms and band filling effects in GaAs–AlGaAs V-groove quantum wires*, Applied Physics Letters **70**, 993 (1997).

[94] Z. Y. Xu, V. G. Kreismanis, and C. L. Tang, *Photoluminescence of GaAs-$Al_xGa_{1-x}As$ multiple quantum well structure under high excitations*, Applied Physics Letters **43**, 415 (1983).

[95] E. Kapon, K. Kash, E. M. Clausen, D. M. Hwang, and E. Colas, *Luminescence characteristics of quantum wires grown by organometallic chemical vapor deposition on nonplanar substrates*, Applied Physics Letters **60**, 477 (1992).

[96] P. Ils, C. Gréus, A. Forchel, V. D. Kulakovskii, N. A. Gippius, and S. G. Tikhodeev, *Linear polarization of photoluminescence emission and absorption in quantum-well wire structures: Experiment and theory*, Physical Review B **51**, 4272 (1995).

[97] H. Akiyama, T. Someya, and H. Sakaki, *Optical anisotropy in 5-nm-scale T-shaped quantum wires fabricated by the cleaved-edge overgrowth method*, Physical Review B **53**, R4229 (1996).

[98] F. Vouilloz, D. Y. Oberli, M.-A. Dupertuis, A. Gustafsson, F. Reinhardt, and E. Kapon, *Polarization Anisotropy and Valence Band Mixing in Semiconductor Quantum Wires*, Physical Review Letters **78**, 1580 (1997).

[99] L. Landau, Lifshitz, and L. Pitaevskii, *Electrodynamics of Continuous Media*, Second Edition, Vol. 8, Course of theoretical physics (Pergamon, 1984).

[100] J. Wang, M. S. Gudiksen, X. Duan, Y. Cui, and C. M. Lieber, *Highly Polarized Photoluminescence and Photodetection from Single Indium Phosphide Nanowires*, Science **293**, 1455 (2001).

[101] H. E. Ruda and A. Shik, *Polarization-sensitive optical phenomena in semiconducting and metallic nanowires*, Physical Review B **72**, 115308 (2005).

[102] M. De Luca, A. Zilli, H. A. Fonseka, S. Mokkapati, A. Miriametro, H. H. Tan, L. M. Smith, C. Jagadish, M. Capizzi, and A. Polimeni, *Polarized Light Absorption in Wurtzite InP Nanowire Ensembles*, Nano Letters **15**, 998 (2015).

[103] I. Strzalkowski, S. Joshi, and C. R. Crowell, *Dielectric constant and its temperature dependence for GaAs, CdTe, and ZnSe*, Applied Physics Letters **28**, 350 (1976).

[104] I. H. Malitson, *Interspecimen Comparison of the Refractive Index of Fused Silica*,†*, Journal of the Optical Society of America **55**, 1205 (1965).

[105] C. Z. Tan, *Determination of refractive index of silica glass for infrared wavelengths by IR spectroscopy*, Journal of Non-Crystalline Solids **223**, 158 (1998).

[106] D. E. Aspnes, S. M. Kelso, R. A. Logan, and R. Bhat, *Optical properties of $Al_xGa_{1-x}As$*, Journal of Applied Physics **60**, 754 (1986).

[107] R. Paniagua-Domínguez, G. Grzela, J. G. Rivas, and J. A. Sánchez-Gil, *Enhanced and directional emission of semiconductor nanowires tailored through leaky/guided modes*, Nanoscale **5**, 10582 (2013).

[108] H. E. Ruda and A. Shik, *Polarization-sensitive optical phenomena in thick semiconducting nanowires*, Journal of Applied Physics **100**, 024314 (2006).

[109] Q. Gu and Y. Fainman, *Semiconductor Nanolasers* (Cambridge University Press, 2017).

[110] G. Wunner and A. Pelster, eds., *Selforganization in Complex Systems: The Past, Present, and Future of Synergetics*, Understanding Complex Systems (Springer International Publishing, 2016).

[111] J. Zheng, X. Yan, W. Wei, C. Wu, N. Sibirev, X. Zhang, and X. Ren, *A Low-Threshold Miniaturized Plasmonic Nanowire Laser with High-Reflectivity Metal Mirrors*, Nanomaterials **10**, 1928 (2020).

[112] H. Li, Y. Chen, Z. Wei, and R. Chen, *Optical property and lasing of GaAs-based nanowires*, Science China Materials **63**, 1364 (2020).

[113] T. Sidiropoulos, *Enhanced light-matter interactions in laser systems incorporating metal-based optical confinement*, PhD thesis (Imperial College London, 2014).

[114] C. Couteau, A. Larrue, C. Wilhelm, and C. Soci, *Nanowire Lasers*, Nanophotonics **4**, 90 (2015).

[115] M. G. A. Bernard and G. Duraffourg, *Laser Conditions in Semiconductors*, physica status solidi (b) **1**, 699 (1961).

[116] M. Bernardi, D. Vigil-Fowler, C. S. Ong, J. B. Neaton, and S. G. Louie, *Ab initio study of hot electrons in GaAs*, Proceedings of the National Academy of Sciences **112**, 5291 (2015).

[117] J. Shah, *Ultrafast Spectroscopy of Semiconductors and Semiconductor Nanostructures*, Vol. 115, Springer Series in Solid-State Sciences (Springer Berlin Heidelberg, 1999).

[118] T. Elsaesser, J. Shah, L. Rota, and P. Lugli, *Initial thermalization of photoexcited carriers in GaAs studied by femtosecond luminescence spectroscopy*, Physical Review Letters **66**, 1757 (1991).

[119] R. W. Schoenlein, W. Z. Lin, E. P. Ippen, and J. G. Fujimoto, *Femtosecond hot-carrier energy relaxation in GaAs*, Applied Physics Letters **51**, 1442 (1987).

[120] J. F. Young, T. Gong, P. M. Fauchet, and P. J. Kelly, *Carrier-carrier scattering rates within nonequilibrium optically injected semiconductor plasmas*, Physical Review B **50**, 2208 (1994).

[121] K. Barnham and D. Vvedensky, *Low-Dimensional Semiconductor Structures* (Cambridge University Press, 2001).

[122] M. A. Zimmler, F. Capasso, S. Müller, and C. Ronning, *Optically pumped nanowire lasers: invited review*, Semiconductor Science and Technology **25**, 024001 (2010).

[123] K. K. N. Simon M. Sze, *Physics of Semiconductor Devices*, edited by V. K. Jain and A. Verma, Environmental Science and Engineering (Springer International Publishing, 2014), p. 815.

[124] Z. Wu *et al.*, *All-Inorganic $CsPbBr_3$ Nanowire Based Plasmonic Lasers*, Advanced Optical Materials **6**, 1800674 (2018).

[125] S. Arab, P. D. Anderson, M. Yao, C. Zhou, P. D. Dapkus, M. L. Povinelli, and S. B. Cronin, *Enhanced Fabry-Perot resonance in GaAs nanowires through local field enhancement and surface passivation*, Nano Research **7**, 1146 (2014).

[126] A. Siegman, *Lasers* (University Science Books, 1986).

[127] R. F. Oulton, V. J. Sorger, T. Zentgraf, R.-M. Ma, C. Gladden, L. Dai, G. Bartal, and X. Zhang, *Plasmon lasers at deep subwavelength scale*, Nature **461**, 629 (2009).

[128] M. W. Sigrist, *Laser: Theorie, Typen und Anwendungen* (Springer Berlin Heidelberg, 2018).

[129] A. W. Snyder and R. A. Sammut, *Fundamental (HE_{11}) modes of graded optical fibers*, Journal of the Optical Society of America **69**, 1663 (1979).

[130] J. T. Robinson, K. Preston, O. Painter, and M. Lipson, *First-principle derivation of gain in high-index-contrast waveguides*, Optics Express **16**, 16659 (2008).

[131] D. Saxena, *Design and Characterisation of III-V Semiconductor Nanowire Lasers*, PhD thesis (The Australian National University, 2017).

[132] W. T. Silfvast, *Laser Fundamentals* (Cambridge University Press, 2004).

[133] S. W. Eaton, A. Fu, A. B. Wong, C.-Z. Ning, and P. Yang, *Semiconductor nanowire lasers*, Nature Reviews Materials **1**, 16028 (2016).

[134] Z. Gu, Q. Song, and S. Xiao, *Nanowire Waveguides and Lasers: Advances and Opportunities in Photonic Circuits*, Frontiers in Chemistry **8**, 1 (2021).

[135] A. Maslov and C. Ning, *Modal gain in a semiconductor nanowire laser with anisotropic bandstructure*, IEEE Journal of Quantum Electronics **40**, 1389 (2004).

[136] B. F. Mayer, *Ultrafast Nanowire Lasers as On-Chip Devices Dissertation Ultrafast Nanowire Lasers as On-Chip Devices*, PhD thesis (Technische Universität München, 2017).

[137] S.-W. Chang and S. L. Chuang, *Fundamental Formulation for Plasmonic Nanolasers*, IEEE Journal of Quantum Electronics **45**, 1014 (2009).

[138] D. B. Li and C. Z. Ning, *Peculiar features of confinement factors in a metal-semiconductor waveguide*, Applied Physics Letters **96**, 181109 (2010).

[139] D. Saxena, F. Wang, Q. Gao, S. Mokkapati, H. H. Tan, and C. Jagadish, *Mode Profiling of Semiconductor Nanowire Lasers*, Nano Letters **15**, 5342 (2015).

[140] A. V. Maslov and C. Z. Ning, *Reflection of guided modes in a semiconductor nanowire laser*, Applied Physics Letters **83**, 1237 (2003).

[141] R. F. Oulton, V. J. Sorger, D. A. Genov, D. F. P. Pile, and X. Zhang, *A hybrid plasmonic waveguide for subwavelength confinement and long-range propagation*, Nature Photonics **2**, 496 (2008).

[142] R. F. Oulton, *Surface plasmon lasers: Sources of nanoscopic light*, Materials Today **15**, 26 (2012).

[143] S. A. Church, R. Al-Abri, P. Parkinson, and D. Saxena, *Optical characterisation of nanowire lasers*, Progress in Quantum Electronics, 100408 (2022).

[144] R.-M. Ma, R. F. Oulton, V. J. Sorger, and X. Zhang, *Plasmon lasers: coherent light source at molecular scales*, Laser & Photonics Reviews **7**, 1 (2013).

[145] H. Yokoyama and S. D. Brorson, *Rate equation analysis of microcavity lasers*, Journal of Applied Physics **66**, 4801 (1989).

[146] N. Mundigl, *Nanophotonics in Single Wurtzite GaAs Nanowires*, Master thesis (Universität Regensburg, 2022).

[147] L. W. Casperson, *Threshold characteristics of multimode laser oscillators*, Journal of Applied Physics **46**, 5194 (1975).

[148] M. P. van Exter, G. Nienhuis, and J. P. Woerdman, *Two simple expressions for the spontaneous emission factor β*, Physical Review A **54**, 3553 (1996).

[149] N. Gregersen, T. R. Nielsen, J. Mørk, J. Claudon, and J. M. Gérard, "Controlling Nanowire Emission Profile Using Conical Taper", in Integrated photonics and nanophotonics research and applications (2008), ITuB2.

[150] D. Dalacu, P. J. Poole, and R. L. Williams, *Nanowire-based sources of non-classical light*, Nanotechnology **30**, 232001 (2019).

[151] S. I. Azzam, A. V. Kildishev, R.-M. Ma, C.-Z. Ning, R. Oulton, V. M. Shalaev, M. I. Stockman, J.-L. Xu, and X. Zhang, *Ten years of spasers and plasmonic nanolasers*, Light: Science & Applications **9**, 90 (2020).

[152] C. Li, Z. Liu, J. Chen, Y. Gao, M. Li, and Q. Zhang, *Semiconductor nanowire plasmonic lasers*, Nanophotonics **8**, 2091 (2019).

[153] M. Bauch, K. Toma, M. Toma, Q. Zhang, and J. Dostalek, *Plasmon-Enhanced Fluorescence Biosensors: a Review*, Plasmonics **9**, 781 (2014).

[154] E.-P. Li and H.-S. Chu, *Plasmonic Nanoelectronics and Sensing* (Cambridge University Press, 2014).

[155] W. L. Barnes, A. Dereux, and T. W. Ebbesen, *Surface plasmon subwavelength optics*, Nature **424**, 824 (2003).

[156] S. Kumar and S. I. Bozhevolnyi, *Single Photon Emitters Coupled to Plasmonic Waveguides: A Review*, Advanced Quantum Technologies **4**, 2100057 (2021).

[157] P. B. Johnson and R. W. Christy, *Optical Constants of the Noble Metals*, Physical Review B **6**, 4370 (1972).

[158] Y.-J. Lu *et al.*, *Plasmonic Nanolaser Using Epitaxially Grown Silver Film*, Science **337**, 450 (2012).

[159] L. K. van Vugt, S. Rühle, and D. Vanmaekelbergh, *Phase-Correlated Nondirectional Laser Emission from the End Facets of a ZnO Nanowire*, Nano Letters **6**, 2707 (2006).

[160] B. Hua, J. Motohisa, Y. Kobayashi, S. Hara, and T. Fukui, *Single GaAs/GaAsP Coaxial Core-Shell Nanowire Lasers*, Nano Letters **9**, 112 (2009).

[161] B. Mayer, L. Janker, D. Rudolph, B. Loitsch, T. Kostenbader, G. Abstreiter, G. Koblmüller, and J. J. Finley, *Continuous wave lasing from individual GaAs-AlGaAs core-shell nanowires*, Applied Physics Letters **108**, 071107 (2016).

[162] N. B. Nguyen, M. P. Nielsen, L. Lafone, E. Clarke, P. Fry, and R. F. Oulton, *Hybrid gap plasmon GaAs nanolasers*, Applied Physics Letters **111**, 261107 (2017).

[163] L. Xu *et al.*, *Surface plasmon enhanced luminescence from organic-inorganic hybrid perovskites*, Applied Physics Letters **110**, 233113 (2017).

[164] X. Wang, S.-C. Huang, S. Hu, S. Yan, and B. Ren, *Fundamental understanding and applications of plasmon-enhanced Raman spectroscopy*, Nature Reviews Physics **2**, 253 (2020).

[165] X. Liu, Q. Zhang, J. N. Yip, Q. Xiong, and T. C. Sum, *Wavelength Tunable Single Nanowire Lasers Based on Surface Plasmon Polariton Enhanced Burstein–Moss Effect*, Nano Letters **13**, 5336 (2013).

[166] S. Kim and R. Yan, *Recent developments in photonic, plasmonic and hybrid nanowire waveguides*, Journal of Materials Chemistry C **6**, 11795 (2018).

[167] I. H. Malitson, F. V. Murphy, and W. S. Rodney, *Refractive Index of Synthetic Sapphire*, Journal of the Optical Society of America **48**, 72 (1958).

[168] L. Zhu, *Modal Properties of Hybrid Plasmonic Waveguides for Nanolaser Applications*, IEEE Photonics Technology Letters **22**, 535 (2010).

[169] M. H. Huang, S. Mao, H. Feick, H. Yan, Y. Wu, H. Kind, E. Weber, R. Russo, and P. Yang, *Room-Temperature Ultraviolet Nanowire Nanolasers*, Science **292**, 1897 (2001).

[170] J. C. Johnson, H.-J. Choi, K. P. Knutsen, R. D. Schaller, P. Yang, and R. J. Saykally, *Single gallium nitride nanowire lasers*, Nature Materials **1**, 106 (2002).

[171] X. Duan, Y. Huang, R. Agarwal, and C. M. Lieber, *Single-nanowire electrically driven lasers*, Nature **421**, 241 (2003).

[172] J. X. Ding, J. A. Zapien, W. W. Chen, Y. Lifshitz, S. T. Lee, and X. M. Meng, *Lasing in ZnS nanowires grown on anodic aluminum oxide templates*, Applied Physics Letters **85**, 2361 (2004).

[173] Y. Zhang, R. E. Russo, and S. S. Mao, *Quantum efficiency of ZnO nanowire nanolasers*, Applied Physics Letters **87**, 043106 (2005).

[174] C. F. Zhang, Z. W. Dong, G. J. You, S. X. Qian, and H. Deng, *Multiphoton route to ZnO nanowire lasers*, Optics Letters **31**, 3345 (2006).

[175] A. H. Chin, S. Vaddiraju, A. V. Maslov, C. Z. Ning, M. K. Sunkara, and M. Meyyappan, *Near-infrared semiconductor subwavelength-wire lasers*, Applied Physics Letters **88**, 163115 (2006).

[176] C. Zhang, F. Zhang, T. Xia, N. Kumar, J.-i. Hahm, J. Liu, Z. L. Wang, and J. Xu, *Low-threshold two-photon pumped ZnO nanowire lasers*, Optics Express **17**, 7893 (2009).

[177] H. Zhu, Y. Fu, F. Meng, X. Wu, Z. Gong, Q. Ding, M. V. Gustafsson, M. T. Trinh, S. Jin, and X.-Y. Zhu, *Lead halide perovskite nanowire lasers with low lasing thresholds and high quality factors*, Nature Materials **14**, 636 (2015).

[178] Y.-H. Chou *et al.*, *High-Operation-Temperature Plasmonic Nanolasers on Single-Crystalline Aluminum*, Nano Letters **16**, 3179 (2016).

[179] J. Ho, J. Tatebayashi, S. Sergent, C. F. Fong, Y. Ota, S. Iwamoto, and Y. Arakawa, *A Nanowire-Based Plasmonic Quantum Dot Laser*, Nano Letters **16**, 2845 (2016).

[180] Q. Zhang, G. Li, X. Liu, F. Qian, Y. Li, T. C. Sum, C. M. Lieber, and Q. Xiong, *A room temperature low-threshold ultraviolet plasmonic nanolaser*, Nature Communications **5**, 4953 (2014).

[181] H. Yu, T. P. H. Sidiropoulos, W. Liu, C. Ronning, P. K. Petrov, S.-H. Oh, S. A. Maier, P. Jin, and R. F. Oulton, *Influence of Silver Film Quality on the Threshold of Plasmonic Nanowire Lasers*, Advanced Optical Materials **5**, 1600856 (2017).

[182] Q. Zhang *et al.*, *Wavelength Tunable Plasmonic Lasers Based on Intrinsic Self-Absorption of Gain Material*, ACS Photonics **4**, 2789 (2017).

[183] E. Kapon, S. Simhony, R. Bhat, and D. M. Hwang, *Single quantum wire semiconductor lasers*, Applied Physics Letters **55**, 2715 (1989).

[184] E. Kapon, *Quantum wire lasers*, Proceedings of the IEEE **80**, 398 (1992).

[185] M. Asada, Y. Miyamoto, and Y. Suematsu, *Theoretical Gain of Quantum-Well Wire Lasers*, Japanese Journal of Applied Physics **24**, L95 (1985).

[186] S. Das Sarma and D. W. Wang, *Many-Body Renormalization of Semiconductor Quantum Wire Excitons: Absorption, Gain, Binding, and Unbinding*, Physical Review Letters **84**, 2010 (2000).

[187] Y. Masumoto, B. Fluegel, K. Meissner, S. Koch, R. Binder, A. Paul, and N. Peyghambarian, *Band-gap renormalization and optical gain formation in highly excited CdSe*, Journal of Crystal Growth **117**, 732 (1992).

List of publications

- **V. Zeller**, N. Mundigl, P. E. Faria Junior, J. Fabian, C. Schüller, and D. Bougeard, *Wurtzite Quantum Wires with Strong Spatial Confinement: Polarization Anisotropies in Single-Wire Spectroscopy*, Phys. Rev. Appl. **18**, 054014 (2022).

- S. Meier, P. E. F. Junior, F. Haas, E.-S. Heller, F. Dirnberger, **V. Zeller**, T. Korn, J. Fabian, D. Bougeard, and C. Schüller, *Intersubband Excitations in Ultrathin Core-Shell Nanowires in the One-Dimensional Quantum Limit Probed by Resonant Inelastic Light Scattering*, Phys. Rev. B **104**, 235307 (2021).

- M. Halbhuber, J. Mornhinweg, **V. Zeller**, C. Ciuti, D. Bougeard, R. Huber, and C. Lange, *Non-Adiabatic Stripping of a Cavity Field from Electrons in the Deep-Strong Coupling Regime*, Nat. Photonics **14**, 675 (2020).

- T. Grünbaum, S. Milster, H. Kraus, W. Ratzke, S. Kurrmann, **V. Zeller**, S. Bange, C. Boehme, and J. M. Lupton, *OLEDs as Models for Bird Magnetoception: Detecting Electron Spin Resonance in Geomagnetic Fields*, Faraday Discuss. **221**, 92 (2020).

Danksagung

Die Zeit während der Promotion ist sicherlich mit Höhen und Tiefen verbunden und besonders herausfordernd, wenn gerade eine Pandemie die Welt überrollt. Genau deshalb schätze ich die Unterstützung all jener Menschen sehr, die mich in den letzten Jahren begleitet haben und ohne die das Gelingen dieser Arbeit nicht möglich gewesen wäre.

An erster Stelle gilt besonderer Dank **Prof. Dr. Dominique Bougeard**. Zum einen für die Möglichkeit, in seiner Arbeitsgruppe zu promovieren und zum anderen für seine ausgezeichnete Betreuung. Danke für die vielen Stunden, die wir über meine Arbeit, über Physik oder ganz andere Dinge diskutiert haben, dein offenes Ohr in jeglichen Angelegenheiten und dein Engagement gegenüber jedem in der Gruppe, das zu einer außergewöhnlich guten Arbeitsatmosphäre führt!

Herzlich bedanken möchte ich mich auch bei **Prof. Dr. Christian Schüller** für das Begutachten dieser Arbeit und die hilfreichen Diskussionen im Rahmen des Projekts zu den Quantendrähten.

Ein sehr großes Dankeschön auch an **Dr. Florian Dirnberger**, nicht nur für die Einarbeitung in das Thema dieser Doktorarbeit und die ständige Hilfe bei jedweden fachlichen Fragen, sondern auch für die schöne und lustige Zeit, die wir außerhalb der "Physik-Welt" miteinander verbringen.

Vielen Dank auch an **Dr. Paulo E. Faria Junior** für die vielen intensiven Diskussionen über die Wurtzit Subband-Struktur unserer Quantendrähte, die Berechnung der Absorptionsspektren und die tolle Zusammenarbeit im Rahmen meiner Doktorarbeit.

Weiterer großer Dank gilt **Dr. Dieter Schuh**, der Spezialist und Problemlöser in allen Angelegenheiten ist. Besonders möchte ich mich bei ihm für die fachkundige Betreuung an der III-V MBE und seinem stetigen Bereitschaftsdienst während den Wachstumszeiten meiner Proben bedanken. In diesem Zusammenhang möchte ich mich auch besonders bei

Dr. Michael Prager bedanken, der mir an der MBE immer mit Rat und Tat zur Seite stand.

Danke auch an **Imke Gronwald**, die mit ihrer Kompetenz, Freude und Neugier immer hilfreiche Tipps parat hat. Speziell möchte ich mich für das Schleusen der Proben und das Teilen ihrer Expertise am REM und im Chemielabor bedanken.

Zudem möchte ich mich bei **Andreas Schützenmeier** bedanken, ohne dessen gewissenhafte Arbeit und technischen Support unsere Wissenschaft nicht umsetzbar wäre.

Bei **Dr. Matthias Kronseder** möchte ich mich für das Bedampfen unserer Wachstumssubstrate und für das Wachsen der Gold/AlOx Substrate in der Metall-MBE bedanken. Danke auch für deine spontane Verfügbarkeit und deine tolle Gesellschaft im MBE Labor!

Ein großes Dankeschön auch an **Ulla Franzke** für ihre herzliche und offene Art und das Regeln aller administrativen Angelegenheiten.

Besonderer Dank gilt auch meinen fleißigen Masterstudenten **Lukas Herrmann** und **Nadine Mundigl**, die mit ihrer gewissenhaften Arbeit wesentlich zu dieser Dissertation beigetragen haben. Die Zusammenarbeit mit euch hat sehr viel Spaß gemacht!

Bei **Andreas Schmidbauer** möchte ich mich vor allem dafür bedanken, dass er mein Leben seit dem Studium mit seiner Freundschaft bereichert. Danke für unsere schöne gemeinsame Zeit innerhalb und außerhalb der Universität! In diesem Zusammenhang möchte ich mich auch bei **Christoph Rohrmeier** bedanken. Ohne euch zwei wäre ich wohl nicht bis hierher gekommen.

Für die zusammen verbrachte Zeit ein großes Dankeschön auch an **Laura Diebel**, die mich mit ihrem Einhorn-Glitzer immer aufheitern kann.

Ein sehr großes Dankeschön auch an die ehemaligen Doktoranden. Neben den schon Genannten gilt dies vor allem **Dr. Maike Halbhuber**, **Dr. Michaela Trottmann**, **Dr. Thomas Mayer** und **Dr. Floyd Schauer** für die tolle und lustige gemeinsame Zeit in der Arbeitsgruppe und auch außerhalb der Universität, besonders während der Cocktail Happy Hour. Ohne euch wären die vergangenen Jahre nicht einmal halb so schön gewesen!

Außerdem möchte ich den weiteren Mitgliedern unserer Arbeitsgruppe **Rudolf Richter**, **Lukas Rupp**, **Jakob Walsh** und **Michaela Zoth** für die freundschaftliche und kollegiale Atmosphäre danken!

Danke auch an **Matthias Knorr** für sein immer offenes Ohr und unsere - teilweise doch längeren - Gespräche zwischen Tür und Angel.

Schlussendlich geht mein größter Dank an meine Familie, meine Freunde und vor allem an Hans. Danke für eure liebevolle Unterstützung während der Zeit meiner Promotion und den Rückhalt, den ich von euch erhalte. Danke, dass ihr mein Leben so wunderbar macht!